A Study of Heavy Precipitation Events in Taiwan during 10-13 August, 1994.
Part II: Mesoscale Model Simulations

W.-K. Tao[1], C.-S. Chen[2], Y. Jia[1,3], D. Baker[4], S. Lang[1,3], P. Wetzel[1] and W. K.-M. Lau[1]

[1]*Laboratory for Atmospheres*
NASA/Goddard Space Flight Center
Greenbelt, MD 20771
USA

[2]*National Central University*
Taiwan, Republic of China

[3]*Science Systems and Applications Inc.*
NASA/Goddard Space Flight Center
Greenbelt, MD 20771
USA

[4]*Physics Department*
Austin College
900 North Grand Avenue
Sherman, TX 75090
USA

Journal of the Meteorological Society of Japan

(February 21, 2001)

Corresponding author address: Dr. Wei-Kuo Tao, Mesoscale Atmospheric Processes Branch,
Code 912, NASA/GSFC, Greenbelt, MD 20771
email: tao@agnes.gsfc.nasa.gov

ABSTRACT

Several heavy precipitation episodes occurred over Taiwan from August 10 to 13, 1994. Precipitation patterns and characteristics are quite different between the precipitation events that occurred from August 10 and 11 and from August 12 and 13. In Part I (Chen *et al.* 2001), the environmental situation and precipitation characteristics are analyzed using the EC/TOGA data, ground-based radar data, surface rainfall patterns, surface wind data, and upper air soundings.

In this study (Part II), the Penn State/NCAR Mesoscale Model (MM5) is used to study the precipitation characteristics of these heavy precipitation events. Various physical processes (schemes) developed at NASA Goddard Space Flight Center (i.e., cloud microphysics scheme, radiative transfer model, and land-soil-vegetation surface model) have recently implemented into the MM5. These physical packages are described in the paper. Two way interactive nested grids are used with horizontal resolutions of 45, 15 and 5 km.

The model results indicated that cloud physics, land surface and radiation processes generally do not change the location (horizontal distribution) of heavy precipitation. The Goddard 3-class ice scheme produced more rainfall than the 2-class scheme. The Goddard multi-broad-band radiative transfer model reduced precipitation compared to a one-broad band (emissivity) radiation model. The Goddard land-soil-vegetation surface model also reduce the rainfall compared to a simple surface model in which the surface temperature is computed from a surface energy budget following the "force-restore" method. However, model runs including all Goddard physical processes enhanced precipitation significantly for both cases. The results from these runs are in better agreement with observations. Despite improved simulations using different physical schemes, there are still some deficiencies in the model simulations. Some potential problems are discussed.

Sensitivity tests (removing either terrain or radiative processes) are performed to identify the physical processes that determine the precipitation patterns and characteristics for heavy rainfall events. These sensitivity tests indicated that terrain can play a major role in determining the exact location for both precipitation events. The terrain can also play a major role in determining the intensity of precipitation for both events. However, it has a large impact on one event but a smaller one on the other. The radiative processes are also important for determining the precipitation patterns for one case but not the other. The radiative processes can also effect the total rainfall for both cases to different extents.

1. Introduction

Flash floods occur frequently in Taiwan during the Mei-Yu season (May and June) and in summer. During Mei-Yu season, precipitation systems associated with the Mei-Yu front can produce a large amount of rainfall (Kuo and Chen 1990; Lin *et al.* 1992; Li *et al.* 1997; Trier *et al.* 1990) or heavy rainfall events can take place near mountain slope areas as a result of the interaction between topography and prevailing wind (Chen and Lin 1996, 1997; Yeh and Chen 1998; Akaeda *et al.* 1995). In summer, typhoons over or near Taiwan can bring heavy rainfall. However, in the summer season, there is still the possibility that heavy rainfall will occur in Taiwan even though a typhoon is not over nor in the vicinity of Taiwan.

Heavy rainfall occurred over the western side of Taiwan's complex terrain from August 10 to 13, 1994 [see Fig. 2 in Part I, Chen *et al.* (2001)] after Typhoon Doug moved northward from the East China Sea into Taiwan and on towards the Yellow Sea. On August 10, most of the rainfall fell over sloped areas. The heaviest daily rainfall totals were in excess of 200 mm over southwestern as well as central Taiwan. However, not much rainfall occurred over northern Taiwan. The lack of rainfall over northern Taiwan also occurred on August 11, 12 and 13. The larger rainfall amounts shifted westward from the sloped areas on August 10 toward lower terrain on August 11. On August 12 and 13, most of the higher rainfall amounts were found over the coastal area in southwestern Taiwan. Notably, about 300 to 400 mm per day fell over the coastal area in southwest Taiwan on August 12 and 13. The distribution of rainfall amount was different on August 10 and 11 (termed as Case 1) compared to August 12 and 13 (termed as Case 2). In Part I, Chen *at al.* (2001) also categorized the precipitation pattern into two types, propagating and stationary. For the propagating type of precipitation, rainrates increased or remained the same as systems went from the plains to mountainous regions. With the quasi-stationary type of precipitation, however, rainrates decreased as precipitation propagated across the plains and into the mountains. Chen *at al.* (2001) also proposed several physical processes (i.e., topographic lifting, interactions between the offshore and prevailing wind) for these two types of precipitation patterns. Please refer to Part I for detailed discussions on these precipitation events.

In this study (Part II), the Penn State/NCAR Mesoscale Model (MM5) with new improved sophisticated physics (i.e., cloud microphysics, radiation, and land-soil-vegetation-surface processes) is used to simulate the characteristics of precipitation analyzed in Part I. Nested grids were used with horizontal resolutions of 45, 15, and 5 km. Sensitivity tests were also performed to identify the major factors influencing the location of heavy precipitation (i.e., over sloped or coastal areas), the precipitation amounts, as well as the type of precipitation pattern (propagating or stationary). In Section 2, the new and improved MM5 physics will be described. The model results and the comparison with observations will be discussed in Section 3. Sensitivity tests associated with the impact of terrain, microphysics, radiation and land surface processes will be presented in Section 4. Section 5 is the discussion and summary.

2. Method

2.1 MM5 and model physics

The regional-scale model used in this study is the fifth-generation of the Penn State/NCAR mesoscale model MM5 V2.5. Details of the model can be found in Anthes *et al.* (1987), Grell *et al.* (1995) and Dudia (1993). It uses finite differences and a time-splitting scheme to solve prognostic equations on an Arakawa type-B staggered grid. MM5 uses observed (or large-scale modeled) wind, temperature and humidity for its initial conditions and incorporates relatively realistic topography as well as sophisticated physical processes to represent the appropriate forcing. These physical processes include clouds, a planetary boundary layer (PBL), short- and long-wave radiation, and surface fluxes of heat, moisture and momentum. Because of the wide variety of physical parameterizations that can be used in the MM5, only a brief overview along with some relevant new improvements are listed as follows:

1. The model was initialized from NOAA/NCEP analyses (2.5^o by 2.5^o). Time-varying lateral boundary conditions were provided at 12-h intervals. The model was integrated, respectively, from 1200 UTC 9 August to 1800 UTC 11 August 1994 (for Case 1) and from 1200 UTC 11 August to 1800 UTC 13 August 1994 (for Case 2). The main reason for not running the model continuously from August 10 to August 13 is that MM5 as well as most other mesoscale models is still not capable of capturing the exact location, timing and accurate amount of precipitation after just 1-2 days of model integration.

2. Multiple nested domains were constructed with grid resolutions of 45, 15 and 5 km, respectively; the corresponding numbers of grid points are 59 x 60 x 27, 58 x 79 x 27 and 82 x 73 x 27 (Fig. 1). The model top is located at the 50 hPa level. Time steps of 120, 40 and 13.33 s were used in these nested grids, respectively. The largest domain covers the area from southern Japan to the northern Philippines (35 - 15 N), and from central China to the west Pacific (104 - 134 E). The finest domain covers the entire island of Taiwan and the immediate vicinity.

3. The Grell cumulus parameterization scheme (1993) was used for the coarse grid mesh (45 and 15 km). The Grell scheme is based on Arakawa and Schubert (1974), and it includes moist convective-scale downdrafts. The Grell scheme consists of three parts: static control (a cloud model with specified cloud-thermodynamic properties), dynamic control (triggering - determines the amount and location of the moist convection), and feedback (determines the vertical distribution of latent heat release and moistening). In the 5 km grid domain, the Grell parameterization scheme was turned off.

4. A two-class ice cloud microphysics scheme (Dudhia 1989) was used for the resolvable scale convection. This scheme allows for simple ice-phase processes. Cloud water becomes cloud ice and rain water becomes snow when the temperature is below the freezing point. This cloud scheme has been designed and used mainly for coarse grid resolutions in MM5.

A two-class liquid and three-class ice microphysics scheme developed and coded by the Goddard Mesoscale Modeling Group (Tao and Simpson 1993) has already been implemented into MM5 and ARPS. The microphysical scheme implemented into MM5 and ARPS was mainly based on Lin *et al.* (1983) with additional processes from Rutledge and Hobbs (1984). In addition, the Goddard microphysics scheme has several minor modifications. The first modification is the option to choose either graupel or hail as the third class of ice (McCumber *et al.* 1991). Graupel has a low density and a large intercept (i.e., high number concentration). In contrast, hail has a high density and a small intercept (i.e. low number concentration). These differences can affect not only the description of the hydrometeor population, but also the relative importance of the microphysical-dynamical-radiative processes. Second, a saturation technique was implemented by Tao *et al.* (1989). This saturation technique is basically designed to ensure that supersaturation (subsaturation) cannot exist at a grid point that is clear (cloudy). This saturation technique is one of the last microphysical processes to be computed. It is only done prior to evaluating the evaporation of rain and deposition or sublimation of snow/graupel/hail. A third difference is that all microphysical processes (transfer rates from one type of hydrometeor to another) are calculated based on one thermodynamic state . This ensures that all processes are treated equally. The opposite approach is to have one particular process calculated first modifying the temperature and water vapor content (i.e., through latent heat release) before the second process is computed. The fourth difference is that the sum of all the sink processes associated with one species will not exceed its mass. This ensures that the water budget will be balanced in the microphysical calculations.

The Goddard three-class ice scheme was also used for comparison with the two-class ice scheme.

5. The standard MM5 atmospheric radiation model includes longwave (infrared) and shortwave (visible) parameterizations that interact with the atmosphere (Dudhia 1989). This scheme uses a broad band two-stream (upward and downward fluxes) approach for the radiative flux calculations. Its longwave radiation scheme is an emissivity-type (which uses a precalculated emissivity function to represent the frequency integrated absorption spectrum of water vapor weighted by a suitable envelope function). MM5's shortwave radiation scheme takes into account the effect of the solar zenith angle, clouds having their own albedo and absorption coefficient, and clear air (scattering and water vapor absorption).

The radiative transfer package developed by Chou (1984, 1986) and Chou and Kouvaris (1991) was recently implemented into MM5 by the Goddard Mesoscale Modeling Group. This radiation scheme is a broad-band model and is considered state-of-the-art in the General Circulation Modeling community (the UCLA GCM, Goddard GCM, CSU GCM and FSU global model have all adopted this radiative scheme). The shortwave radiation models of Chou (1990, 1992) are used to compute solar heating in the atmosphere/clouds and at the surface. The solar spectrum is divided into two regions: the ultraviolet (UV) and visible region (wavelength < 0.69 um) and the near infrared (IR) region (wavelength > 0.69 um). In the UV and visible spectral region, ozone absorption and Rayleigh and cloud scattering are included. In the near IR region, absorption due to water vapor, cloud, CO_2 and O_2, and scattering due to clouds are included. The UV and visible region is further grouped into four bands, and an effective ozone absorption coefficient and an effective Rayleigh scattering coefficient are given for each band. The near IR region is divided into seven water vapor absorption bands. The k-distribution method is applied to each of the seven bands for computing the absorption of solar radiation by water vapor and clouds. The four-stream discrete-ordinate scattering algorithm of Liou *et al.* (1988) is used to compute multiple scattering within a cloud layer. The simple scattering albedos for each of the seven near IR bands are taken from King *et al.* (1990).

The longwave radiation model of Chou and Suarez (1994) is used to compute cloud and atmospheric infrared cooling. The infrared spectrum is divided into eight bands. The water vapor transmission function is computed using the k-distribution method, and the CO_2 and O_3 transmission functions are computed using look-up tables. The absorption due to cloud hydrometeors is also included. Clouds are assumed to be gray and non-scattering. The multiplication approximation is used to take into account the effect of overlapping of different gas and cloud absorptions. Use of a fully explicit microphysics scheme (liquid and ice) and a fine horizontal resolution (5 km or less) can give realistic cloud optical properties and cloudiness which are crucial for determining the radiation budgets with less tuning.

The Goddard Radiation scheme was also compared with the standard MM5 radiation scheme (Dudhia 1989).

6. The planetary boundary layer parameterization used in MM5 was a Blackadar high-resolution model (Blackadar 1979; Zhang and Anthes 1982). The vertical mixing of horizontal wind, potential temperature, mixing ratio of water vapor, cloud water and cloud ice are parameterized. Also, the surface heat and moisture fluxes (from both ocean and land) are computed from similarity theory.

7. The PLACE model (Parameterization for Land-Atmosphere Cloud Exchange, Fig. 2) has recently been incorporated as an option within MM5 through a coupling with four popular boundary layer options: the Blackadar high resolution PBL, the MRF model, a simple O'Brien K-profile boundary layer, and the Seaman-Stauffer TKE boundary layer. PLACE is a detailed interactive process model of the heterogeneous land surface (soil and vegetation) and adjacent near-surface atmosphere. PLACE basically consists of three elements. These are: **(1)** a soil module that includes at least seven water reservoirs (i.e. plant internal storage, dew/intercepted precipitation, surface material (no roots), a topsoil root layer, a subsoil root layer, and two deeper layers that regulate seasonal and interannual variability of the soil hydrology); **(2)** a surface slab of vegetation, litter and other loose material which shades the soil and acts as the source for sensible heat flux, and which intercepts precipitation and dew; and **(3)** the surface layer of the atmosphere (up to the lowest computational level of the model to which it is coupled) within which the fluxes of sensible heat and water vapor are calculated. More details on PLACE can be found in Wetzel and Boone (1995). PLACE has been a very active participant in two major international intercomparison projects, sponsored by World Climate Research Project (WCRP)/GEWEX: The Project for the Intercomparison of Land surface Parameterization Schemes [PILPS, see Henderson-Sellers *et al.* (1993, 1995)] and the Global Soil Wetness Project [GSWP, see Boone and Wetzel (1999)]. This work has demonstrated that PLACE is as accurate as other widely used land-surface schemes in GCMs, such as BATS. However PLACE has been specifically designed to be applied to mesoscale models with grid resolutions of 100 km or smaller. PLACE was linked to the GCE model to study the impact of soil moisture patches and atmospheric boundary conditions on cloud structure, rainfall, and soil moisture distribution (Lynn *et al.* 1998). Lynn *et al.* (2001) have tested the MM5-PLACE performance for sea-breeze generated deep convection over the Florida peninsula during the Convection and Precipitation Electrification Experiment (CaPE). They indicated that the land processes, initial soil moisture and planetary boundary layer can have a major impact on the sea breeze, lake breeze and moist convection.

The PLACE model was compared to a simple surface model (the SLAB model in MM5) in which the surface temperature is computed from a surface energy budget following the "force-restore" method developed by Blackadar (Zhang and Anthes 1982).

8. The temporal differencing used in MM5 consists of leapfrog steps with an Asselin filter. A centered finite difference method is used for advection. It is well known that these difference methods can generate negative mass for hydrometeors near and at cloud boundaries. The adjustment used in MM5 is to reassign all negative hydrometeors to be zero. This can cause an imbalance in the water budget. Note that the error grows with the number of time iterations not the length of model integration.

To remedy this shortcoming (especially for long term model integrations and for fine model resolution simulations), a mass conservation - adjustment scheme was implemented into MM5. The procedure for this mass conservation scheme for all hydrometeors is as follows: 1) compute the total positive mass (P) and negative mass (N) over the entire domain, 2) set all negative mass to be zero, and 3) recompute the positive mass by multiplying by a factor of (P-N)/P. This type of adjustment has been used in many cloud scale models (i.e., Soong and Ogura 1973; Goddard Cumulus Ensemble Model, and many others).

2.2 *Experiment design*

The experiment design is summarized in Table 1. A total of twelve experiments are performed. There are seven runs simulating Case 1 and five runs for Case 2. In Run 1, the standard MM5 options for the physical processes (two-class ice scheme, simple radiation scheme, SLAB surface scheme) are chosen. The Goddard three-class ice scheme is used in Run 2 for comparison with the two-class ice scheme in Run 1. The difference between Run 1 and Run 3 is that the Goddard radiation scheme is used in Run 3 instead of the simple Dudhia radiation scheme. The PLACE land scheme is used in Run 4. In Run 5, all of the new modifications, the Goddard microphysics, PLACE and radiation scheme, are used. Run 6 is the same as Run 5 except that total (solar and longwave) radiation is turned off. The aim of this sensitivity test is to examine the effect of the land-sea breeze and PBL processes on precipitation over Taiwan. Run

7 is the same as Run 5 except the complex terrain is removed. The role of topographic lifting on the precipitation processes will be quantified in this sensitivity test.

Runs 8, 9, 10, 11 and 12 follow the model set-ups for Runs 1, 2, 5, 6 and 7, respectively, except for Case 2 (August 12 and 13).

3. General Results and Comparisons with Observations

Observations indicated that heavy precipitation developed over sloped terrain (250-500 m altitude) and most precipitation occurred in the daytime for Case 1 (August 10-11). In contrast, heavy precipitation developed over the relatively flat coast and lower elevation area (100 m altitude), and most of the rainfall occurred during the afternoon and into the night for Case 2 (August 12-13). The first objective of this modeling study is to examine and compare the model simulated heavy precipitation events with observations. In particular, the temporal variation of rainfall will be examined and compared to the observed over various locations/stations (i.e., flat and sloped areas).

3.1 Case 1: August 10-11 1994 (Run 1)

Figure 3 shows six hourly accumulated rainfall simulated in Run 1 (Case 1) over the 5 km resolution domain. Major precipitation starts near the coast of central Taiwan early on the morning of August 10. It propagates inland and also elongates and intensifies in the north and south directions with several centers of heavy rainfall at noon on August 10. Most of the heavy precipitation on that day occurs east of 121 E. Not much rain occurs over northern Taiwan on August 10. The heavy precipitation dissipates after 6 PM in central Taiwan. The model also produced significant rainfall over southern Taiwan on August 10. Those characteristics were generally consistent with observations. In addition, the model produced significant rainfall over the ocean late on August 10 which is also in agreement with observed overcast conditions (seen in IR). On August 11, the model significantly underestimates the rainfall over the coastal areas even though its simulated rainfall is located mainly over the west coast as observed. Most of the heavy precipitation is over the Strait on the morning of August 11. Also, some precipitation developed over northern Taiwan early on the morning on August 11 and is not seen in the ground measurements.

For the stations along the southern coast of Taiwan on August 11, the magnitude of rainfall for Tainan and Kangshan was less than observed. The rainfall began too early at Kaoshiung.

Figure 4 shows the MM5 simulated time series of rainfall for two stations (Alishan and Taichung) located in central Taiwan. The variation of the rainfall with time for the station near sloped terrain (Alishan) and for the station at lower elevation (Taichung) is quite different. Heavy precipitation fell out quickly and stopped rapidly in Taichung. By contrast, the precipitation lasted longer in Alishan. The MM5 simulation captured the observed precipitation characteristics well (discussed in Part I). But, the model simulated total rainfall is about 200 mm which overestimates the observations by about 30 mm for station Alishan. For station Taichung, the modeled precipitation started late as well as lasted shorter than observed. Figure 4 also shows the water vapor convergence/divergence over the two stations, Alishan and Taichung. At Alishan, precipitation starts before the strong water vapor convergence and implies that precipitation is mainly caused by the propagation of a convective system from the lower elevation. The water vapor convergence is quite strong between 9AM and noon on August 10. The terrain can play an important role in producing the strong convergence (lifting) of water vapor. Moisture convergence is present prior to and during the rainfall over station Taichung. These features are different from the station over the sloped region.

Figure 5 shows an east-west cross-section of the three dimensional wind field. The vertical velocities are much stronger (over 12 m s^{-1}) for the convective events that occurred over the steep terrain on August 10 compared to those mainly occurring over the flat coastal region on August 11 (few m s^{-1}). These features are consistent with the model simulated rainfall intensity over the flat and sloped areas. Also, note the broad weak downward motion located above the upward motion in the middle troposphere on August 11 in Fig. 5(c) and 5(d). One interesting feature shown in Fig. 5(a) is that the stronger vertical velocities are always at higher altitudes. There is downward motion at 121 E (over the tip of the central terrain) and strong vertical velocity that develops at 121.4 E. Observations [shown in Fig. 2(a) in Part I] indicate that there is precipitation in the same location. The westerlies are much stronger on August 10 than on August 11. The strong westerlies could lead to fast inland movement of precipitation that first develops over the Strait.

Figure 6 shows the time series of the Froude number calculated over the Penghu station [off the coast of Taiwan, see Fig. 1 in Part I]. The Froude number on August 10 ranges from 0.8 to 0.5. The observed Froude number (shown in Part I) was about 0.6 to 0.7. Low-level air parcels could be lifted over the terrain under this type of flow regime. The precipitation could be enhanced over the sloped areas on the upstream side of the Central Mountain Ridge [Smolarkiewicz and Rotunno (1989), discussed in Part I]. The Froude number is smaller and range froms 0.15 to .35 on August 11. The observed Froude number was about 0.3 on August 11. The lower Froude number on August 11 could explain the shift in heavy precipitation from the sloped areas to lower terrain.

3.2 *Case 2: August 12-13 1994 (Run 8)*

For August 12, the rainfall distribution indicates that the convective systems are mainly located near the coast and over flat and lower elevation areas (Fig. 7). Heavy precipitation mainly occurs in the afternoon and into the early morning on August 13. These two features are very different from the August 10 event. No rainfall occurred over northern Taiwan in this case. The modeled precipitation characteristics are consistent with observations. However, the magnitude of the rainfall amounts for August 12 are much less than were observed (Table 3). Some of the heavy precipitation is over the Strait. Satellite IR imagery did show significant overcast over the Strait on August 12. On August 13, all heavy precipitation occurred over the west coast of southern Taiwan. Again, some of the heaviest precipitation is over the Strait. The model also underestimated significantly the rainfall on August 13.

Figure 8 shows an east-west cross-section of the three dimensional wind field. The vertical velocities associated with the convective systems are quite weak on both days. Also, they are mainly located over the flat area at low altitude along the west coast of Taiwan. Also, note that downward motion occurs above the upward motion as on August 11. One difference in the environmental wind pattern between August 12 and 13 is a relatively strong low level westerly wind on August 13. The strong westerly wind may have led to stronger convective systems (producing heavy precipitation) that moved inland on August 13 compared to those that developed on August 12.

There are several possible reasons for MM5's inability to simulate heavy precipitation on August 11, 12 and 13. The first reason may be related to the initial and lateral boundary conditions. Instead of using NOAA/NCEP data, the MM5 was initialized with EC/TOGA data. Another experiment was performed with four-dimensional dynamic nudging (Stauffer and Seaman 1990) on the 45 km grid. These two runs did not improve the model performance however. Another possible reason is that the model physics may not be accurate enough to produce heavy precipitation. Sensitivity tests on the model physics are performed and the results are discussed in the next section.

4. Sensitivity Tests

The physical processes that are responsible for the two precipitation events will be identified by performing sensitivity tests. The impact of terrain, microphysical processes, radiative processes and land surface processes will be examined as listed in Table 1 on the development and intensity of the observed precipitation events.

4.1 Microphysics (Runs 2 and 9)

Figure 9 shows the daily accumulated rainfall distribution for Case 1 and Case 2 using the Goddard 3-class ice (3ICE) scheme. The impact of the microphysical schemes on the horizontal distribution of rainfall is not significant for both cases. Most of the rainfall fell over sloped areas on August 10 and most of the higher rainfall amounts were found over the coastal area in southwestern Taiwan on August 12 and 13 which is well simulated for both cases (Runs 1 and 2 for Case 1 and Runs 8 and 9 for Case 2). The heavy precipitation that developed over the coast on August 13 simulated in Run 9 is in better agreement with observation than Run 8. In terms of precipitation, the 3ICE run (Run 2) simulated slightly more surface rainfall (6% increase over 2 days) and rain area than Run 1 using the simple two-class ice (2ICE) scheme (Table 2). However, the Goddard 3ICE scheme (Run 8) has much more of an impact on rainfall in Case 2 than in Case 1 (Table 3). The different large-scale environment between Cases 1 and 2 (discussed in Part I) could be the cause for the differing impact of microphysical schemes on rainfall production. This result simply implies that the impact of microphysical schemes on rainfall may be case dependent. Note that the simulated rainfall amount is in better agreement with observation for Case 2 when the Goddard 3ICE scheme is used.

Figure 10 shows the cloud (cloud water and cloud ice) and precipitable water (rain and snow) using the 2ICE scheme at 12 LST on August 10. Figure 11 shows the cloud, rain, snow and graupel using the Goddard 3ICE scheme. The third class of ice, graupel, with a faster fall speed, can fall into the melting layer and enhance the surface precipitation. Note that the 3ICE scheme produces a distinct multi-cellular cloud structure while the 2ICE scheme does not. Long-lasting tropical and midlatitude squall lines usually have multi-cellular cloud structure (see a review by Houze 1997). No observations on cloud structure are available for these particular heavy precipitation events.

Kuo *et al.* (1996) used the MM5 to assess the performance of various subgrid-scale cumulus parameterization and resolvable-scale microphysics schemes in the simulation of explosive marine cyclogenesis at grid resolutions of 20 and 60 km. Their results showed that the resolvable-scale microphysics schemes [i.e., Dudhia's simple 2ICE scheme and the Goddard 3ICE scheme] did not have a significant impact on cyclone deepening for tests carried out on the 20 km grid. However, the Goddard 3ICE scheme, that includes graupel microphysics, produces 10%-15% more precipitation than Dudhia's 2ICE scheme. Liu *et al.* (1999), recently, used the MM5 with multiple-nested grids from 54 to 6 km to simulate Hurricane Andrew (1992). Their results suggested that the Goddard 3ICE scheme produced a more realistic eye structure, surface pressure, and spiral rain bands compared to the experiment with the 2ICE scheme. They suggested that graupel occurred in the eye wall which has a faster fall speed than snow. The cloud updrafts therefore have less loading and become stronger in the middle and upper troposphere. Consequently, downdrafts in the eye become stronger, and the associated warming is better simulated. In another MM5 modeling study, Yang *et al.* (2000) showed that the Goddard 3ICE microphysics scheme provided the better precipitation performance for a Mei-Yu frontal system that developed in the spring of 1998 over Taiwan. His results also indicated that the inclusion of graupel produced 10-15% more precipitation throughout the 36 h simulation compared to that without graupel. The current modeling study also indicates that the Goddard 3ICE scheme produces more rainfall than the 2ICE scheme in agreement with previous MM5 modeling results. However, the amount of precipitation increase is much larger in the current Case 2.

A recent GCSS model intercomparison project clearly indicated that cloud resolving models (with high horizontal resolution) using three-class ice schemes produced less of a cold bias compared to those cloud models using a two-class ice scheme for a TOGA COARE deep precipitation episode (Johnson *et al.* 2001). Sensitivity tests showed that the two-class ice scheme produced much more cloud ice but by allowing the small ice to fall a smaller cold bias can be obtained.

4.2 Radiation (Run 3)

The impact of the radiation schemes on the horizontal distribution of rainfall is not as significant as the microphysical schemes for both cases (not shown). For example, the shift in larger rainfall amounts from the sloped areas on August 10 toward lower terrain on August 11 is well simulated in the run (Run 3) using the Goddard radiation scheme as it is in the one using

Dudhia's radiation scheme (Run 1). The Goddard radiation scheme, however, simulated less (26%) surface rainfall especially over the ocean (Table 2). One of the major differences between Dudhia's and the Goddard radiation scheme is the magnitude of longwave cooling in the lower and upper troposphere (see Fig. 12). Dudhia's longwave radiative cooling is over -6 C compared to -4 C in the Goddard radiation scheme near the surface for the cloud-free region [Fig. 12(a)]. Also, very small cooling (less than -0.5 C) above 14 km is produced in the Dudhia scheme. The stronger lower troposheric cooling can increase the relative humidity. In addition, stronger cooling near the surface can contribute to stronger radiative destabilization. Both factors consequently can provide a more favorable thermodynamic condition for cloud to form and, consequently, lead to more rainfall. Over the cloudy region, Dudhia's longwave scheme also produced strong cooling in the lower troposphere. The Goddard scheme produces stronger day time radiative heating compared to Dudhia's [Fig. 12(c)]. This feature will also not favor precipitation processes.

Krishnamurti *et al.* (1991) examined the impact of emissivity and the band radiative model on the track of Typhoon Hope (1979). They found that the band radiative model had a better track forecast compared to the emissivity model. They suggested that the band radiative model produced stronger cooling above 800 mb and less cooling below contributing to stronger radiative destabilization than the emissivity radiative model. The inflowing air supplies this instability for the maintenance of a long-lasting tropical storm. The emissivity model fails to predict a sufficient abundance of low clouds resulting in weaker cooling and hence decay of the storm. The current results do not agree with Krishnamurti *et al.* (1991) because stronger cooling is produced in the lower troposphere when the Dudhia emissivity model is used. One of the physical mechanisms (radiative destabilization) used to explain the effect on precipitation processes, however, is the same between the present study and Krishnamurti *et al.* (1991). The impact of longwave cooling on relative humidity and precipitation processes has been presented in Tao *et al.* (1996) and Sui *et al.* (1997).

4.3 Land Processes (Run 4)

The atmospheric component of MM5-PLACE provides surface winds, surface air temperature, surface pressure, atmospheric moisture, shortwave and longwave radiation, and precipitation to the land surface. The land-surface component returns momentum, sensible heat, and latent heat fluxes to the atmosphere. The coupling is two-way interactive. For example, precipitation can alter the distribution of soil moisture, which in turn changes the partitioning of energy between sensible heat and latent heat. These heat fluxes then may feed back on the subsequent development of clouds and precipitation. The simple Slab surface model does not include this feedback. The inclusion of PLACE (that consists of the moisture feedback and vegetation-wetness) should allow for better simulation of the diurnal cycle of ground surface temperature and wetness.

The impact of the land surface schemes on the horizontal distribution of rainfall is not significant for Case 1 (Fig. 13). Most of the rainfall occurring over sloped areas on August 10 is well simulated. The simulated precipitation on August 11 is also much less than observed. These two features are also simulated in Run 1 using the Slab surface model (Blackadar). The PLACE run results are better over central-northern Taiwan (centered at 24.2N) on August 10 [see Fig. 2(a) in Part I]. A well separated heavy precipitation area over central and northern Taiwan is not simulated in Run 1 which did not use the PLACE model. Precipitation over the Strait and near 23.55 N is well simulated compared to radar observations (shown in Fig. 12 in Part I). This feature is also not well simulated in Runs 1, 2 and 3.

Figure 14 shows the time series of sensible heat fluxes, latent heat fluxes, land surface temperature and rainfall simulated by the PLACE model and by the Slab surface model. Diurnal variation is clearly evident in the surface temperature and surface fluxes. Weaker diurnal variation is found in the run using the PLACE because the PLACE allows for precipitation feedback and vegetation-wetness. In addition, the PLACE model produces more latent heat fluxes than the Slab model on the second day. This is caused by the moistening of the soil by the previous day's precipitation. The sensible heat fluxes simulated by the Slab surface model are stronger than those for the PLACE model for both days (due to higher land surface temperatures in the Slab model).

The use of two different land schemes does not significantly impact the temporal variation of rainfall [Fig. 14(d)]. Both runs show one major heavy rain peak in the early morning of August 10. The Slab model simulated a higher precipitation peak because of stronger sensible heat fluxes. The PLACE model produced more latent heat fluxes and rainfall after this major rainfall peak. Figure 15 shows the observed hourly rainfall during the period between August 10 and 13, 1994. This rainfall information is from 243 stations. Observations indicated the maximum rainfall occurred on the evening of August 10 and 11. Little precipitation occurred between the morning of August 11 and 5 PM LST on August 11. The simulated rainfall starts too early and underestimates the rainfall in the evening of August 10 and 11. The PLACE model with its sophisticated land surface does not improve the timing of precipitation .

Simulated land surface temperatures are higher in the run using the Slab model. The sea surface temperature is about 300 K. Consequently, the run using the PLACE model allows for a stronger land-sea temperature gradient and hence a stronger land-sea breeze circulation is expected in the run using the PLACE model. Precipitation should then preferentially occur near the coastal area and over the Taiwan Strait. Daily precipitation amounts on August 10 and 11 are 3.6% and 35%, respectively, less than when using the Slab surface model for the third domain (land and ocean - see Table 2). The stronger land-sea temperature gradient simulated by the PLACE model run on August 11 does not enhance precipitation. This implies that other factors may play a more important role in precipitation processes for this particular case than the land-sea breeze and surface fluxes .

4.4 PLACE/Goddard three-class ice microphyiscal scheme/Goddard Radiation (Runs 5 and 10)

Figure 16 shows six hourly accumulated rainfall simulated in Case 1 using the Goddard 3-class ice scheme, Goddard radiative transfer model and PLACE (Run 5). Again, the horizontal distribution of major precipitation events on August 10 is well simulated as with the other runs. However, the are three major differences between this run compared to others. The first major difference is that daily precipitation totals on both August 10 and 11 are higher for this run (Table 2). The second major difference is that more precipitation is simulated over central and southern Taiwan on August 11. The third major difference is that precipitation develops over the north coastal areas on August 11 [Fig. 16 (e) and (f)]. The first two differences suggest that the results from this run are in better agreement with observation, but the last difference goes against the observations.

Observations show a rainfall maximum in the afternoon and no precipitation at night on August 10 (Fig. 15). This simulation shows a rain maximum in the morning on August 10 with relatively little rainfall afterward until another rainfall peak on the evening of August 11 [Fig. 14(d)]. The temporal evolution of precipitation for this run is better compared to the other runs. For example, the peak rainfall lasts longer on the morning of August 10. In addition, there is a second rainfall peak on the evening of August 11 that is not simulated in the other runs. This run also simulates the diurnal variation of surface temperature and surface fluxes. The magnitudes of surface temperature and surface fluxes are in closer agreement with Run 4 using the PLACE than they are with Run 1 using the Slab model. The latent heat fluxes are larger on August 10 right after the heavy rainfall event. There is no clear relationship between the rainfall amount and the latent fluxes. Dynamic processes (i.e., moisture convergence and topographic lifting) may play a major role in determining the rainfall amount.

It is interesting to note that the precipitation amount increases significantly in this run using the Goddard ice scheme, Goddard radiation and the Goddard land surface model (PLACE). The PLACE and Goddard radiation scheme should each reduce the rainfall amount compared to the Slab model and Dudhia's simple radiation scheme, respectively. Only inclusion of the Goddard 3ICE scheme should produce more (slightly) precipitation compared with the 2ICE scheme. This suggests that there are non-linear interactive processes between precipitation, radiation and the surface. Different microphysical schemes can either enhance or reduce the cloudiness. Cloudiness can modulate atmospheric radiational cooling and heating profiles that can also effect the surface radiation budget. And, rainfall can modify the surface fluxes.

Figure 17 shows six hourly accumulated rainfall simulated in Case 2 using the Goddard 3-class ice scheme, the Goddard radiative transfer model and PLACE (Run 10). No precipitation is simulated over northern Taiwan as observed. This feature is well simulated by the other runs as well. On August 12, heavy precipitation mainly occurred over the coast, the plain and the slopes of central and southern Taiwan [Figs. 17(a), (b) and (c)]. Some light precipitation developed over the mountainous area on the afternoon of August 12. Topographic lifting could have played a role with this precipitation event, but the evidence is not as strong as with the August 10 case. On August 13, precipitation mainly develops over the Taiwan Strait (close to the coast) and moves inland into southern Taiwan. This feature is better simulated in this Run 10 than in Run 8. These results indicate that including the PLACE, Goddard radiation and the Goddard 3ICE scheme improved the simulation for Case 2. More total daily precipitation is simulated compared to the other runs (Table 3), especially over the southern coast of Taiwan on August 13 which is well simulated in this run. Figure 18 shows the hourly surface fluxes, surface temperature and rainrates averaged over land for Runs 8 and 10. Diurnal variation of surface fluxes and temperature is simulated. Rain occurs on both days over central and southern Taiwan [Figs. 17 and 18(d)]. This is good agreement with observations (Fig. 15). The weaker diurnal variation in surface temperature on August 13 is caused by overcast conditions.

Simulated average hourly rainfall rates for areas over the coast, plains, slopes and mountains as analyzed in Part I [see Figs. 1 and 11 in Part I] from Runs 5 and 10 are shown in Fig. 19. On August 10, precipitation was simulated in the morning in Areas A, B, C, D, E and F [see Part I for details] as observed for Run 5. The maximum rainfall was about 1-2 hours later in Areas E and F not in C and D as observed. These results suggest that the observed eastward-movement of precipitation systems from the coast to the mountains was properly simulated (based on hourly rainfall). This precipitation pattern is termed "propagating type" as discussed in Part I. Precipitation lasted longer in Area E than Area A. This indicates that topographic lifting plays an important role for the precipitation over sloped and mountainous areas. However, the modeled heavy precipitation occurs too early and lasts shorter than observed. Little or no precipitation was observed between the evening (18 LST) of August 10 and the morning of August 11 (11 LST) in Areas A, B, C, D, E and F. Modeled results show no heavy precipitation until the late afternoon of August 11 in Areas A, B and C. For Area C, the heavy precipitation also occurs earlier than observed. On August 12 and 13, light precipitation fell over the sloped areas in central Taiwan as observed [Fig. 19(c)]. Precipitation occurs more along the coast, plains and slopes than over the mountainous areas in southern Taiwan [Figs. 19(e), (e) and (f)]. This feature is in good agreement with observation. Most of the simulated precipitation patterns seem to be of the "quasi-stationary" type for August 12 and 13. Between Areas D and F, there is a 1 hour difference in peak precipitation on the morning of August 12. There is no evidence of the propagating type in the late morning and early afternoon on August 12 as observed. Topographic lifting seems to play a very minor role in the sloped areas for Case 2.

For comparison, the hourly rainfall rates for areas over the coast, plains, slopes and mountains from Run 1 and Run 8 are shown in Fig. 20. The propagating type of precipitation system is simulated for August 10. Precipitation lasted longer in Areas E and F than in Areas A and B. This again indicates that topographic lifting plays an important role for the precipitation over sloped areas (i.e., Fig. 4)[1]. Precipitation is not well simulated for Case 2 as discussed earlier.

Chen *et al.* (2001) indicated that offshore flow was observed along the western coastal areas from central to southern Taiwan in the early morning and late evening [5 and 20 LST on August 10, 11, 12 and 13 - see Fig. 9 in Part I]. Convergence produced by the interaction between offshore and oncoming prevailing (southwesterly wind) winds near the coast plays an important role in the formation and maintenance of precipitation over the coastal area. The transition from offshore to onshore flow occurred at 8 LST on August 10, 11 LST on August 11 and 13, and 14 LST on August 12. Near sloped areas, upslope flow appeared in the late morning or early afternoon. Onshore flow appeared on August 10 producing a confluent area from morning to afternoon. The upward motion associated with the upslope wind superimposed

---

[1] Similar features (characteristics of precipitation and convergence/ divergence of water vapor at Taichung and Alishan stations) are also obtained in Run 5.

on the topographic lifting effect helped intensify precipitation in the sloped and mountainous areas. The variation of surface wind was observed from August 10 to 13. From evening to early morning, offshore flow appeared.

Figure 21 shows the simulated surface wind using the Goddard 3-class ice scheme, the Goddard radiative transfer model and PLACE for Cases 1 and 2 (Runs 5 and 10, respectively). Offshore flow was simulated along the western coastal area of central Taiwan on the early morning of August 10, 12 and 13 as observed [Fig. 21(a), (e) and (f)]. The convergence due to the interaction between offshore flow and prevailing wind plays an important role in precipitation development and enhancement for these days. However, strong convergence areas are mostly located over the Taiwan Strait and in northern Taiwan. Heavy precipitation developed and move inland [Fig. 16(d)]. In addition, the offshore flow was not well simulated along the southern coast of Taiwan. The offshore wind is also present along the western coast in the evening [Fig. 21(c) and (d)]. The transition from offshore to onshore flow occurred on the morning of August 10 [Fig. 21(b)] as observed. A confluent area is simulated near the mountain areas of central Taiwan as is heavy precipitation [Fig. 16(b) and (c)]. A dominant diffluent area is formed from the slopes to the low lands over western Taiwan due to the strong offshore flow and upslope wind on the evening of August 10 [Fig. 21(c)]. In addition, the prevailing westerly wind changed to a southwest wind in the simulation. This can lead to less moisture being transported to the west and southwest coast of Taiwan. Heavy precipitation is not formed during this period and the model results are not in good agreement with observations [Figs. 14(d) and 15].

The offshore flow is stronger and more persistent in the early morning of August 10 for Run 5 compared to Run 1. This could be a major reason that more precipitation is simulated along the western coast in Run 5 than in Run 1. The interaction between the prevailing southwest wind with the offshore flow leads to heavier precipitation over the low-lying western coastal area during the evening of August 11 in Run 5. The prevailing southwest wind is weaker in the Run 1 simulation. Only light precipitation was simulated by Run 1 in the afternoon, and no precipitation occurred in the evening (Fig. 3). The rainfall simulated in Run 1 does not agree very well with the observations.

On August 12, offshore flow was simulated by Run 9 from 00 LST to 08 LST just as observed [i.e., Fig. 21(e)]. Offshore flow was also simulated at 16 LST on August 12 along the southern coastal region. The interaction between the prevailing wind and topographic lifting, however, is not as strong as the August 10 case. Onshore flow was well simulated on the morning of August 13 in central and southern Taiwan. A confluent area simulated in Run 10

[Fig. 21(f)] was persistent. Consequently, the model did better in simulating the precipitation over the southwest coast (Fig. 17) on August 13, especially the early morning. In Run 8, southerly instead of southwesterly wind prevailed over the Taiwan Strait to the west of central Taiwan on August 12. No convergence area was observed near the central western coast. This southerly wind is not favorable for transporting moisture into central Taiwan that can fuel the heavy precipitation. Therefore, precipitation over the western coastal area was underestimated by Run 8.

4.5 Diurnal variation and land-sea breeze interactions (Runs 6 and 11)

In Part I, Chen *et al.* (2001) suggested that a confluent area, formed by the onshore flow and down slope wind, over the plains in the late morning may have played a major role in the propagating type of precipitation on August 10. They also suggested that the confluence due to the interaction of the predominant wind and offshore flow could have been important for developing the quasi-stationary type precipitation on August 12 and 13. A sensitivity test is performed to examine these effects by turning off the radiation for both Case 1 and 2 eliminating the diurnal variation in land surface temperature. The land-sea breeze circulation that causes the offshore and onshore flow is removed in these runs.

No offshore flow is simulated in Case 1 when the radiation is excluded (Run 6). The wind is mostly westerly and south-westerly on the west coast of Taiwan. Once the wind encounters the sloped and mountainous areas, confluence is formed and cloud develops. Figure 22 shows the 6-hourly accumulated rainfall distribution for Run 6. The rainfall distribution is different from the run with radiative processes [Run 5, see Fig. 16]. For example, the heavy precipitation simulated in Run 5 mainly starts near the coast (00-06 LST) and moves to the sloped area (06-12 LST). But, the precipitation simulated in Run 6 [Fig. 22(b)] weakens when it moves to the sloped area. The heavy precipitation simulated in Run 6 also occurs and elongates mainly along the 900-1200 m terrain elevation region. This type of precipitation is the "quasi-stationary" type not the "propagating" types discussed in Part I as well as simulated by Run 5. Note that the heavy precipitation in northern Taiwan for August 10 is over the Strait and not over land as was simulated in Run 5. In addition, heavy precipitation over the Taiwan Strait in the late afternoon and evening of August 11 is less in this run compared to Run 5. These results suggest that the strong land-sea surface temperature gradient in the late afternoon and evening produced in the PLACE run caused the development of heavy precipitation over the Strait.

Again offshore flow is not simulated for Case 2 (Run 11) in the run without radiative processes. Figure 23 shows the 6-hourly accumulated rainfall distribution for Run 11. The heavy precipitation that develops over central and southern Taiwan on August 12 and 13 seems to be the "quasi-stationary" type. The precipitation that developed over central Taiwan before noon on August 12 and on the morning of August 13 was also located mainly along 900-1200 m of terrain elevation as in Run 6. Precipitation over the Taiwan Strait on the morning of 13 August and late afternoon of August 12 [as simulated in Run 10, see Fig. 17] is not simulated in this run. The majority of heavy precipitation is located over southern Taiwan (coast and plain area) in excellent agreement with observations. In Run 10, the majority of heavy precipitation over southern Taiwan is located over the Strait (but very close to land).

As expected, the diurnal variation of land surface temperature and surface fluxes is not simulated in these two runs without radiation (Figs. 24 and 25). The land surface temperature stays between 298 and 299 K and is warmer than the run with radiative processes. The difference in land surface temperature is between 2 to 4 K for Case 1 and 0.5 to 7 K for Case 2. Higher sensible and latent heat fluxes are simulated in Run 6 compared to Run 5. The heavy precipitation in the morning of August 10 lasts shorter, and the precipitation on August 11 is weaker compared to the run with radiation included. For Case 2, higher sensible heat fluxes are simulated in the run without radiation. However, higher latent heat fluxes are only simulated at night (between 18 LST and 06 LST) in the run without radiation. The rainfall is smaller (larger) on 12 August (13 August) compared to the run with radiation (Run 10).

The daily rainfall is reduced by about 24% for August 10 and 52% for August 11 (Table 2) compared to the run with radiation included (Run 5). Over the two-day period, the total precipitation is reduced by about 36% compared to run with radiation. The land-sea breeze circulation may not have had much impact on the location of major precipitation in central and southern Taiwan for this case, but it can still have impact the total rainfall over the Taiwan region for this Case. The total precipitation over two days is reduced (17%) for Case 2 if radiation is not allowed (Table 3). Precipitation is enhanced (32%), however, on August 12 in the run without the radiative processes.

The Goddard Radiation scheme was implemented into the Goddard Cumulus Ensemble (GCE) Model (Tao and Simpson 1993). Tao *et al.* (1996)[2] performed sensitivity tests with and

---

[2] Please refer to Tao *et al.* (1996) for details of using the cloud resolving models to study the cloud-radiation interaction.

without radiation for both tropical and midlatitude mesoscale convective systems. The GCE model results indicated that the dominant process for enhancing surface precipitation in both the tropical and midlatitude cases was radiative cooling. The results also indicated that the overall effect of radiative cooling is to increase the relative humidity. Because of the high moisture content in the tropics, the increase in relative humidity by radiative cooling had more of an impact on precipitation in the tropical case than in the midlatitude case. Radiative cooling led to a 36% increase in rainfall for the tropical case. The midlatitude squall line with a higher CAPE and lower humidity environment was only slightly affected (7%) by any of the longwave mechanisms. Solar heating was run from 9 AM to 1 PM LST in both environments and was found to decrease the precipitation by 7% in each case, compared to the runs with longwave radiation only. This result suggests that solar heating may play a significant role in the daytime minimum/nighttime maximum precipitation cycle found over most oceans, as noted in the observational study of Kraus (1963). Sui *et al.* (1998) also used the GCE model and performed a 15 day integration to simulate TOGA COARE convective systems. Their simulated diurnal variation of surface rainfall is in reasonable agreement with that determined from radar observations. They also found that modulation of convection by the diurnal change in available water as a function of temperature was responsible for a maximum in rainfall after midnight. This simply implies that the increase (decrease) in surface precipitation associated with IR cooling (solar heating) was mainly due to an increase (decrease) in relative humidity. The large-scale environment is moister in Case 1 than Case 2. That may be the reason for the larger impact on rainfall in Case 1 than Case 2.

These sensitivity tests also suggest that diurnal variation of land surface temperature may be needed for the "propagating" type of precipitation (for Case 1). Also, the interaction of the oncoming prevailing wind and offshore flow is not important for developing the "quasi-stationary" type of precipitation on August 12 and 13. The location of the surface precipitation from these two runs (without radiative processes) seems to be in better agreement with observation than the runs with radiative processes. The model, however, is not completely able to simulate the surface wind correctly. In addition, the sea surface temperature does not allow for varying daily in MM5. The diurnal variation in surface temperature is very small (less than 0.2 K). Therefore, this conclusion needs to be taken cautiously.

4.6 Terrain Effects (Runs 7 and 12)

Orographic precipitation is controlled by a number of dynamical and microphysical processes. Houze (1993) summarized that orographic precipitation can be generated by seven types of mechanisms: (1) the seeder-feeder mechanism of Bergeron (1968), (2) condensation through forced upslope flow, (3) upslope triggering of convection, (4) upstream cloud formation resulting from orographic flow blocking or vertically propagating gravity waves, (5) thermal triggering from an elevated heat source, (6) lee side enhancement of precipitation by mountain-induced gravity waves, and (7) lee-side convergence owing to flow around a three-dimensional obstacle. However, the large-scales (synoptic and meso-Alfa-scale) can set the stage for and determine the likelihood of deep moist convection on any given day, while the smaller-scale governs the details of timing and location. The large-scale processes provide stability, moisture, and occasionally the triggering mechanism (i.e., frontal activity or large-scale vertical velocity). Mountain scale processes may provide localized pulses of vertical motion that can initialize moist convective cells. In Part I, Chen *et al.* (2001) suggested that topographic lifting due to the predominant wind and upslope flow could be quite important for the "propagating" type of precipitation on August 10. A sensitivity test removing the terrain is performed for both Cases 1 and 2.

The no terrain case for Case 1 can generate the precipitation on the eastern side of the island for August 10 with precipitation mainly occurring on the central and northern side of Taiwan on August 11 (Fig. 26). A strong westerly wind dominates the lower and middle troposphere during August 10 while a meridional (southerly/northerly) wind prevails on August 11. Thus, precipitation can move to the east coast of Taiwan on August 10 and northern Taiwan on August 11 once the terrain is removed. For Case 2, the precipitation over southern Taiwan on August 13 is not effected by the terrain (Fig. 27) except that the rainfall moves into Taiwan from the Strait in the case without terrain. On August 12, the terrain effect was as important as it was for the August 10/11 case because the rainfall pattern was parallel to the orientation of the mountain and there was major precipitation over central Taiwan in the simulation with terrain (Fig. 17). Based on the rainfall distribution, the sensitivity tests suggest that the terrain can be important for the "propagating" type of precipitation on August 10, but not for the "quasi-stationary" tpye on August 13.

In the no terrain runs, the land surface temperature is higher because the temperature is colder at high elevation (Figs. 24 and 25). The land surface temperature is warmer than the ocean temperature during day time in the cases without terrain. Stronger diurnal variations of surface temperature and latent heat fluxes are simulated in the no terrain cases. The terrain has little impact on the sensible heat fluxes. The heavy precipitation on the morning of August 10 lasts shorter compared to the run with terrain included [Fig. 24(d)]. This result implies that terrain enhanced the precipitation by providing topographic lifting for the August 10 case. More precipitation is simulated on the evening of August 10 and 11 for the no terrain case. This may be due to stronger surface latent heat fluxes. On August 12, precipitation is weaker over land and does not develop until the afternoon in the run without terrain. The precipitation is heavier over southern Taiwan when terrain is removed. The south-westerly wind over southern Taiwan on August 13 may transport moisture inland when the terrain is removed. For August 12, the large-scale flow mainly consists of a weak westerly wind.

The terrain intensified the total precipitation by about 10% for August 10 and about 20% for August 11 (Table 2). The Taiwan terrain only modified the characteristics of the precipitation in terms of location and timing. The terrain reduced the total precipitation by about 7% for August 12 and increased it by about 1% for August 13 (Table 3). Thus, the larger scale (or meso-Alfa-scale) probably played the most important role in providing moisture for Case 2.

Precipitation is more organized in the run with terrain compared to the run without. This implies that the major role of terrain on precipitation processes is determining the location of heavy rainfall. The large-scale influence (i.e., moisture advection) still dominates the rainfall processes. The topographic lifting played a secondary role on August 10.

5. Discussions and Summary

In this study (Part II), the Penn State/NCAR Mesoscale Model (MM5) with various physical processes (schemes) developed at NASA Goddard Space Flight Center (i.e., cloud microphysics scheme, radiative transfer model, and land-soil-vegetation surface model) is used to study the precipitation characteristics of the heavy precipitation events that occurred in Taiwan during August 10-13, 1994. A total of twelve sensitivity tests are performed to examine the physical processes that are responsible for the heavy precipitation events. Two-way interactive nested grids are used with horizontal resolutions of 45, 15 and 5 km. Model results (5 km resolution domain) are compared to observations (Chen *et al.* 2001, Part I).

Table 4 summarizes the major characteristics of these twelve simulations. The model results showed that the location of precipitation was well simulated. The timing and duration of heavy precipitation were not well simulated for both cases. The model using the standard MM5 options (2ICE scheme, simple radiation and SLAB surface model) simulated less rainfall compared to observations. The model results indicated that the cloud physics, land surface and radiation processes do not generally change the location (horizontal distribution) of heavy precipitation.

The Goddard 3-class ice scheme produced more rainfall than the 2-class scheme in both cases. The third class of ice, graupel, with a faster fall speed, can fall into the melting layer and enhance the surface precipitation. However, the 3ICE scheme had much more of an impact on rainfall in Case 2 (August 12-13) than in Case 1 (August 10-11). These results are in agreement with previous MM5 studies (Kuo *et al.* 1996; Liu *et al.* 1999; Yang *et al.* 2000).

The Goddard multiple broad-band radiative transfer model reduced the amount of precipitation compared to a single broad band (emissivity) radiation model. The emissivity radiation model's longwave radiative cooling is over -6 C compared to -4 C in the Goddard radiation scheme near the surface for the cloud-free region. The stronger lower tropospheric cooling can further increase the relative humidity. In addition, stronger cooling near the surface can contribute to stronger radiative destabilization. Both factors consequently can provide a more favorable thermodynamic condition for cloud to form and, consequently, lead to more rainfall.

The Goddard land-soil-vegetation surface model also reduced the rainfall compared to a simple surface model in which the surface temperature is computed from a surface energy budget following the "force-restore" method (SLAB surface model). Diurnal variation is clearly evident in the surface temperature and surface fluxes in both surface models. Weaker diurnal variation is found in the run using the PLACE because the PLACE allows for precipitation feedback and vegetation-wetness. In addition, the PLACE model produces more latent heat fluxes than the Slab model on the second day of model integration. This is caused by the moistening of the soil by the previous day's precipitation. The results also indicated that the run using the PLACE model allows for a stronger land-sea temperature gradient. The stronger land-sea temperature gradient simulated by the PLACE model run also does not enhance precipitation. Stronger latent heat fluxes were simulated in PLACE, but they did not enhance rainfall. Dynamic processes (i.e., moisture convergence and topographic lifting) may have played a major role in determining the rainfall amount.

The results (particularly for the second day of integration) from the model runs including all Goddard physical processes are in better agreement with observations than the runs using standard MM5 options. The Goddard physics runs produced significant precipitation for both cases in better agreement with observations. Hourly rainfall rates for areas over the coast, plains, slopes and mountains are also better simulated in these runs. The run with all Goddard physics, however, produced significant rainfall over the northern Taiwan Strait. This feature was not observed. Note that the PLACE and Goddard radiation scheme each reduce the rainfall amount compared to the Slab model and simple radiation scheme, respectively. Only inclusion of the Goddard 3ICE scheme should produce (slightly) more rainfall compared with the 2ICE scheme. The results suggest that there are non-linear interactive processes between precipitation, radiation and the surface. For example, different microphysical schemes can either enhance or reduce the cloudiness. Cloudiness can modulate atmospheric radiational cooling and heating profiles that can also effect the surface radiation budget. And, rainfall can modify the surface fluxes.

No offshore flow was simulated when the radiation processes were turned off. Heavy precipitation mainly located along areas of 900-1200 m of elevation. The sensitivity tests suggest that diurnal variation of land surface temperature may be needed for the "propagating" type of precipitation (Case 1). The interaction of the oncoming prevailing wind and offshore flow is not important for developing the "quasi-stationary" type of precipitation on August 12 and 13. The model, however, is not completely able to simulate the surface wind correctly. The conclusions from these runs needs to be taken cautiously, however.

The Taiwan terrain can modify the characteristics of the precipitation in terms of location and timing. For example, precipitation is more organized in the run with terrain compared to the run without. Terrain increased the rainfall amount for Case 1 which had strong westerly winds in the lower and middle troposphere. The rainfall, however, was only slightly modified for August 10. This result implies that topographic lifting played a secondary role on August 10. In contrast, terrain effects reduced the total precipitation by about 7% for August 12. The larger scale (or meso-Alfa-scale) probably played the most important role in providing moisture for Case 2, and it dominated the rainfall processes.

No matter how sophisticated the model physics, the synoptic initialization dominates the first 24 hours of simulation. The sensitivity of the model physics becomes more apparent between 24 and 48 hours of simulation time. The surface wind over mountain areas is generally not well simulated. Fine resolution terrain data is needed for future work. Possible reasons for some of the poor simulations are:

(1) The model was initialized with a very coarse resolution (2 by 2 degree) for both atmospheric thermodynamic, dynamic and soil vegetation land data sets. In addition, the SST was kept constant neglecting the impact of radiation, precipitation and winds.

(2) The model's horizontal resolution was 5 km. Consequently, the resolution may not have been accurate enough to simulate detailed convective cells that produce heavy precipitation.

(3) The model was initialized with poor terrain resolution. Figure 28 shows the real and model terrain. The deficiency in terrain resolution may lead to the poor simulation of surface winds.

(4) The model's physical processes may need more improvement. Observations are needed to assess the performance of different physical processes.

Future modeling works will be aimed to resolve these issues.

6. Acknowledgment

The first, third, fourth, fifth and sixth authors are supported by the NASA Headquarters Atmospheric Dynamics and Thermodynamics Program, the NASA Natural Hazard Program and the interdisciplinary program of Earth Science Enterprise (ESE). We thank Dr. R. Kakar (HQ) for his support. We wish to thank Drs. B. Lynn and D. Stauffer for helping to implement the PLACE model into MM5. Acknowledgment is also made to NASA/Goddard Space Flight Center for computer time used in the research.

The second author is supported by the National Science Council, Taiwan, Republic of China under grant NSC 89-2111-M-008-009. The Institute of Atmospheric Physics and the Computer Center of National Central University provided computer resources for the second author.

7. References

Akaeda, K., J. Reisner and D. Parsons, 1995: The role of mesoscale and topographically induced circulations initiating a flash flood observed during the TAMEX project. *Mon. Wea. Rev.*, **123**, 1720-1739.

Anthes, R. A., E.-Y. Hsie and Y.-H. Kuo, 1987: Description of the Penn State/NCAR Mesoscale Model Version 4 (MM4). NCAR Technical Note, NCAR/TN-282+STR, 66pp.

Arakawa, A. and W. H. Schubert, 1974: Interaction of cumulus cloud ensemble with the large-scale environment. Part I. J. Atoms. Sci., 31, 674-701.

Bergeron, T., 1968: On the low-level redistribution of atmospheric water by orography. P*roceedings, International Cloud Physics Conference*, Toronto.

Blackadar, A. K., 1979: High resolution models of the planetary boundary layer. Advances in Environmental Science and Engineering, 1, No. 1. Pfafflin and Ziegler, Eds., Gordon and Briech Sci. Publ., New York, 50-85.

Boone, A. and P. J. Wetzel, 1999: A simple scheme for modeling sub-grid soil texture variability for use in an atmospheric climate model. *J. Met. Soc. Japan*, **77**, 317-333

Chen, C.-S., W.-K. Tao, Y. Jia, and S. Lang, 2001: A study of heavy precipitation events in Taiwan during 10-13 August, 1994: Part I: Observations, J. Meteor. Soc. Japan (submitted).

Chen, C.-S., and C.-Y. Lin, 1996: The characteristics of some mountain-generated precipitation systems under weak synoptic forcing during Mei-Yu season. Proc. Natl. Sci. Counc. ROC(A), 20, 11-22.

Chen, C.-S., and C.-Y. Lin, 1997: A preliminary study of the formation of precipitation systems under undisturned conditions during TAMEX. Meteorol.Atmos. Phys., 64, 83-105.

Chou, M.-D., 1984: Broadband water vapor transmission functions for atmospheric IR flux computation. J. Atmos. Sci., 41, 1775-1778.

Chou, M.-D., 1986: Atmospheric solar heating rate in the water vapor bands. J. Climate Appl. Meteor., 25, 1532-1542.

Chou, M.-D., 1990: Parameterization for the absorption of solar radiation by O2 and CO2 with application to climate studies. J. Climate, 3, 209-217. Chou, M.-D., 1992: A solar radiation model for use in climate studies. *J. Atmos. Sci.*, **49**, 762-772.

Chou, M.-D. and L. Kouvaris, 1991: Calculations of transmission functions in the IR CO2 and O3 Bands. *J. Geophys. Res.*, **96**, 9003-9012.

Chou, M.-D., 1992: A solar radiation model for use in climate studies. *J. Atmos. Sci.*, **49**, 762-772.

Chou, M.-D., and M. J. Suarez, 1994: An efficient thermal infrared radiation parameterization for use in general circulation models. NASA Tech. Memo. 104606, 3 , 85 pp.

Dudhia, J., 1989: Numuerical study of convection observed during winter monsoon experiment using a mesoscale two-dimensional model. *J. Atmos. Sci.*, **46**, 3077-3107.

Dudhia, J., 1993: A nonhydrostatic version of the Penn State-NCAR mesoscale model: Validation tests and simulation of an Atlantic cyclone and cold front. *Mon. Wea. Rev.*, **121**, 1493-1513.

Grell, G. A., 1993: Prognostic evaluation of assumptions used by cumulus parameterizations. *Mon. Wea. Rev.*, **121**, 764-787.

Grell, G. A., J. Dudhia and D. R. Stauffer, 1994: A description of the Fifth-Generation Penn State/NCAR Mesoscale Model (MM5). NCAR Technical Note, NCAR/TN-398+IA, pp107.

Henderson-Sellers, Z.-L. Yang and R. E. Dickinson, 1993: The project for intercomparison of land surface parameterization schemes. *Bull. Amer. Meteor. Soc.*, **74**, 1335-1349.

Henderson-Sellers, A. J. Polcher, P. K. Love, K. McGuffie, T. H. Chen, 1995: The project for intercomparison of land surface parameterization schemes (PILPS): Phases 2 and 3, *Bull Amer. Meteor. Soc.*, **76**, 489-503.

Houze, R.A., Jr., 1993: Cloud Dynamics. *Academic Press*, 573 pp.

Houze, R.A., Jr., 1997: Stratiform precipitation in regions of convection: a meteorological paradox? *Bull. Amer. Met. Soc.*, **78**, 2179-2196.

Johnson, D., W.-K. Tao, J. Simpson, and C.-H. Sui, 2001: A study of the response of deep tropical clouds to mesoscale processes, Part I: Modeling strategy and simulation of toga coare convective systems *J. Atmos. Sci.*. (submitted)

King, M. D., Radke, L. F., & Hobbs, P. V., 1990: Determination of the spectral absorption of solar radiation by marine strato-cumulus clouds from airborne measurements within clouds. *J. Atmos. Sci.*, **47**, 894-907.

Krishnamurti, T. N., K. S. Yap and D. K. Oosterhof, 1991: Sensitivity of tropical storm forecast to radiative destabilization. *Mon. Wea. Rev.*, **119**, 2176-2205.

Kraus, E. B., 1963: The diurnal precipitation change over the sea. *J. Atmos. Sci.*, **20**, 546-551.

Kuo, Y.-H., and G. T.-J. Chen, 1990: The Taiwan area mesoscale experiments: An overview. *Bull. Amer. Meteor. Soc.*, **71**, 488-503.

Kuo, Y.-H., R. J. Reed and Y.-B. Liu, 1996: The ERICA IOP5 storm. Part III: Mesoscale cyclogenesis and precipitation parameterization. *Mon. Wea. Rev.*, **124**, 1409-1434.

Li, J., and Y.-L. Chen, 1999: A case study of nocturnal rainshowers over the windward coastal region of the island of Hawaii. *Mon. Wea. Rev.*, **127**, 2674-2692

Li, J., Y.-L. Chen, and W.-C. Lee, 1997: Analysis of a heavy rainfall event during TAMEX. *Mon. Wea. Rev.*, **125**, 1060-1082.

Lin, Y.-L., R. D. Farley and H. D. Orville, 1983: Bulk parameterization of the snow field in a cloud model. *J. Clim. Appl. Meteor.*, **22**, 1065-1092.

Liou, K.-N., Fu, Q., and Ackerman, T. P., 1988: A simple formulation of the delta-four-stream approximation for radiative transfer parameterizations. *J. Atmos. Sci.*, **45**, 1940-1947.

Liu, Y., D.-L. Zhang, and M. K. Yau, 1999: A multiscale numerical study of Hurricane Andrew (1992). Part II: Kinematics and inner-core structures. *Mon. Wea. Rev.*, **127**, 2597-2616.

Lynn, B. H., W.-K. Tao and P. Wetzel, 1998: A study of landscape generated deep moist convection. *Mon. Wea. Rev.*, **126**, 928-942.

Lynn, B. H., D. Stauffer, P. Wetzel, W.-K. Tao, P. Alpert, N. Perlin, R. D. Baker, R. Munoz, A. Boone, and Y. Jia, 2001: A simulation of a Florida sea-breeze using a mesoscale model

(MM5) with a new turbulent kinetic energy (TKE) atmospheric boundary layer model and sophisticated land surface model (PLACE), *Mon. Wea. Rev.*, (in press).

McCumber, M., W.-K. Tao, J. Simpson, R. Penc, and S.-T. Soong, 1991: Comparison of ice-phase microphysical parameterization schemes using numerical simulations of tropical convection. *J. Appl. Meteor.*, **30**, 985-1004.

Rutledge, S. A., and P. V. Hobbs, 1984: The mesoscale and microscale structure and organization of clouds and precipitation in mid latitude clouds. Part XII: A diagnostic modeling study of precipitation development in narrow cold frontal rainbands. *J. Atmos. Sci.*, **41**, 2949-2972.

Smolarkiewicz, P. K., and R. Rotunno, 1989: Low Froude number flow past three-dimensional obstacles. Part II: Upwind flow reversal zone. *J. Atmos. Sci.*, **47**, 1498-1511.

Soong, S.-T., and Y. Ogura, 1973: A comparison between axisymmetric and slab symmetric cumulus models. *J. Atmos. Sci.*, **30**, 879-893.

Stauffer, D. R. and N. L. Seaman, 1990: Use of four-dimensional assimilation in a limited-area mesoscale model. Part I: Experiments with synoptic-scale data. *Mon. Wea. Rev.*, **118**, 1250-1277.

Sui, C.-H., X. Li, and K.-M. Lau, 1997: Radiative-convective processes in simulated diurnal variations of tropical oceanic convection. *J. Atmos. Sci.*, **55**, 2345-2357.

Tao, W.-K., and J. Simpson, 1989: Modeling study of a tropical squall-type convective line. *J. Atmos. Sci.*, **46**, 177-202.

Tao, W.-K., and J. Simpson, 1993: The Goddard Cumulus Ensemble Model. Part I: Model description. *Terrestrial, Atmospheric and Oceanic Sciences (TAO)*, **4**, 19-54.

Tao, W.-K., J. Simpson, S. Lang, C.-H. Sui, B. Ferrier, and M.-D. Chou, 1996: Mechanisms of cloud-radiation interaction in the tropics and midlatitudes. *J. Atmos. Sci* . **53**, 2624-2651.

Trier, S. B., D. B. Parsons and T. J. Matejka, 1990: Observations of a subtropical cold front in a region of complex terrain. *Mon. Wea. Rev.*, **118**, 2449-2470.

Wetzel, P. J., and A. Boone,1995: A parameterization for land-atmosphere-cloud exchange (PLACE): Documentation and testing of a detailed process model of the partly cloudy boundary layer over heterogeneous land. *J. of Climate*, **8**, 1810-1837.

Yang, M.-J., F.-C. Chien and M.-D. Cheng, 2000: Precipitation parameterization in a simulated Mei-Yu front. *Terrestrial, Atmospheric and Oceanic Sciences (TAO)*, **11**, 393-422.

Yeh, H.-C., and Y.-L. Chen, 1998: Characteristics of the rainfall distribution over Taiwan during TAMEX. *J. Appl. Meteor.*, **37**, 1457-1469.

Zhang, D.-L., and R. A. Anthes, 1982: A high-resolution model of the planetary boundary layer-sensitivity tests and comparisons with SESAME-79 data. *J. Appl. Meteor.*, **21**, 1594-1609.

FIGURE CAPTIONS

Figure 1 Nested configuration used by the model. Horizontal resolutions for domains 1, 2 and 3, are 45, 15 and 5 km, respectively.

Figure 2 Schematic representation of the PLACE Model. The calculation of each specific physical parameters is listed (equation) in Wetzel and Boone (1995). (See text for more details.)

Figure 3 Six hourly accumulated rainfall simulated by the MM5 for Case 1 from **(a)** 00-06 AM August 10 to **(h)** 18:00 to 24:00 PM August 11, 1994. The simulated rainfall is obtained from the 5 km resolution domain. LST stands for local standard time.

Figure 4 Time evolution of rainfall and convergence/divergence of water vapor at two stations (Alishan and Taichung). **(a)** and **(b)** are modeled rainfall over Alishan and Taichung, respectively. **(c)** and **(d)** are the same as (a) and (b) except for convergence/divergence of water vapor. The units for the convergence/divergence of water vapor are kg/kg/s and the contour interval is 2×10^{-6} kg/kg/s.

Figure 5 Cross-sections of wind speed (m s^{-1}) and vertical velocity (m s^{-1}). **(a)** is at 06 AM August 10, **(b)** is at 12 AM August 10, **(c)** is at 06 AM August 11 and **(d)** is at 12 AM August 11. West/east cross-sections at 23.2 N is shown in (a) and (c). West/east cross-sections at 23.5 N is shown in (b) and (d). (See Fig. 3.)

Figure 6 Time series of the Froude number calculated over the Penghu station (119.3E and 23.4N) for Case 1.

Figure 7 Same as Fig. 3 except for Case 2 (Run 8).

Figure 8 Cross-sections (west/east at 23.55 N) of wind speed (m s^{-1}) and vertical velocity (m s^{-1}). **(a)** is at 06 AM August 12, **(b)** is at 06 AM August 13 and **(c)** is at 18 PM August 13.

Figure 9 Daily accumulated rainfall simulated by MM5 for Case 1 and Case 2. **(a)** is for August 10 and **(b)** is for August 11 using the Goddard 3-class ice scheme. **(c)** and **(d)** are the same as (a) and (b), respectively, except for using the 2-class ice scheme. **(e)**, **(f)**, **(g)** and **(h)** are the same as (a), (b), (c) and (d), respectively, except for Case 2.

Figure 10 Cross-sections (west/east at 23.55 N) of **(a)** cloud (cloud water and cloud ice) and **(b)** precipitable water (rain and snow) using a 2- class ice scheme at 12 LST on August 10. The cloud ice and snow are located above the melting level (about 6 km). The units are g/kg. The contour intervals are 0.01, 0.1, 0.5 and 1 g/kg for (a), and 0.1, 1, 4 and 8 g/kg for (b).

Figure 11 Cross-sections (west/east at 23.55 N) of **(a)** cloud, **(b)** rain, **(c)** snow and **(d)** graupel using the Goddard 3-class ice scheme at 12 LST on August 10. The units are g/kg. The contour intervals vary and are indicated.

Figure 12 Atmospheric radiative cooling and heating over land (Taiwan Island) using Dudhia's radiation scheme and the Goddard radiation scheme. **(a)** is for 2200 local standard time (LST) 9 August, **(b)** 0000 LST 10 August, **(c)** 1200 LST 10 August and **(d)** 0000 LST 12 August. The open circles are Run 1 (Dudhia's radiation scheme) and dark circles Run 3 (Goddard Radiation scheme).

Figure 13 As Fig. 9 except that the PLACE is used. **(a)** is for August 10 and **(b)** is for August 11.

Figure 14 Time evolution of rainfall, surface temperature and surface fluxes from Run 1 (using the Slab model, 2-class ice scheme and simple radiation scheme), Run 4 (using the PLACE, 2-class ice scheme and simple radiation scheme) and Run 5 (using PLACE, 3-class ice microphysics and Goddard radiation). **(a)** is for sensible fluxes, **(b)** latent heat fluxes, **(c)** surface temperature and (d) rainfall. Open circles are Run 1, dark circles Run 4 and crosses Run 5. These values are area averaged over the land (Taiwan) only.

Figure 15 Observed hourly rainfall during the period between August 10 and 13, 1994. The rainfall information is averaged over 243 stations.

Figure 16 As Fig. 3 except that the Goddard 3-class ice scheme, the Goddard radiation scheme and the PLACE are used (Run 5, Case 1).

Figure 17 As Fig. 7 except that the Goddard 3-class ice scheme, the Goddard radiation scheme and the PLACE are used (Run 10, Case 2).

Figure 18 As Fig. 14 except for Case 2. Open circles are for Run 8 (Slab model, 2ICE and Dudhia's radiation scheme), and crosses are for Run 10 (using PLACE, 3-class ice scheme and Goddard radiation).

Figure 19 Hourly rainfall rates for areas over the coast, plains, slopes and mountains. **(a)** and **(d)** are for Areas A and B representing the coastal areas in central and south-central, and southern Taiwan, respectively. **(b)** and **(e)** are for Areas C and D representing the plain areas of central and south-central, and southern Taiwan, respectively. **(c)** and **(f)** are for Areas E and F representing the sloped and mountainous areas in central and south-central, and southern Taiwan, respectively. Areas A, B, C, D, E and F are shown in Fig. 1 in Part I. These rainfall rates are from Run 5 and Run 10.

Figure 20 As Fig. 19 except for Run 1 and Run 8.

Figure 21 Surface wind at **(a)** 05 LST August 10, **(b)** 11 LST August 10, **(c)** 19 LST August 10, **(d)** 18 LST August 11, **(e)** 05 LST August 12, and **(f)** 5 LST August 13. Results are from the runs using the PLACE, Goddard Radiation and Goddard 3ICE microphysical scheme (Runs 5 and 10).

Figure 22 As Fig. 16 except that the Goddard radiation scheme is turned off (Run 6, Case 1).

Figure 23 As Fig. 17 except that the Goddard radiation scheme is turned off (Run 11, Case 2).

Figure 24 As Fig. 14 except that the results are from runs without radiation and terrain. Crosses are for Run 5 (PLACE, 3ICE and Goddard radiation scheme), open circles Run 6 (without radiation) and dark circles Run 7 (no Terrain).

Figure 25 As Fig. 24 except for Case 2. Crosses are for Run 10 (PLACE, 3ICE and Goddard radiation scheme), open circles Run 11 (without radiation) and dark circles Run 12 (no Terrain).

Figure 26 As Fig. 16 except that terrain is excluded (Run 7, Case 1).

Figure 27 As Fig. 26 except for Case 2 (Run 12).

Figure 28 **(a)** Taiwan topography used in MM5. Contours are every 100 m. **(b)** Real Taiwan topography. Contours are every 50 m (from 500 m to 2500 m).

TABLES

Table 1 Summary of numerical experiments.

Table 2 Daily accumulated rainfall in mm for Case 1 (August 10 and 11) and Case 2 (August 12 and 13). Observational rainfall is summed from 237 ground stations

Table 3 Same as Table 2 except for Case 2 (August 12 and 13).

Table 4 Major Characteristics of Precipitation Structures and Results Simulated in Different Runs Using Different Physical Processes for Case 1 (August 10-11) and Case 2 (August 12-13).

Table 1

Run	Land Processes	Microphysics	Radiation	Terrain	Case
1	Blackadar	2-Ice	Dudhia	Yes	1
2	Blackadar	3-Ice	Dudhia	Yes	1
3	Blackadar	2-Ice	Goddard	Yes	1
4	PLACE	2-Ice	Dudhia	Yes	1
5	PLACE	3-Ice	Goddard	Yes	1
6	PLACE	3-Ice	No	Yes	1
7	PLACE	3-Ice	Goddard	No	1
8	Blackadar	2-Ice	Dudhia	Yes	2
9	Blackadar	3-Ice	Dudhia	Yes	2
10	PLACE	3-Ice	Goddard	Yes	2
11	PLACE	3-Ice	No	Yes	2
12	PLACE	3-Ice	Goddard	No	2

Table 2

Run	August 10/11
1	41.44/18.24
2	47.19/16.00
3	30.58/13.32
4	39.93/11.80
5	62.36/48.18
6	47.53/23.01
7	55.89/38.69
Observation*	60.00/54.00

Table 3

Run	August 12/13
8	7.69/13.92
9	28.31/38.55
10	33.79/46.00
11	44.49/22.09
12	36.11/45.63
Observation*	51.00/24.00

Table 4

	Case 1		Case 2	
	August 10	August 11	August 12	August 13
2ICE, Simple Radiation and one-layer surface model	Propagating type. Location (coastal/sloped - central Taiwan) as observed. Heavy precipitation develops early and lasts shorter than observed.	Location as observed. Precipitation develops later than observed. Rainfall underestimated.	Location (flat/low elevation area) as observed. Rainfall underestimated significantly.	Location (coastal area - S. Taiwan) as observed. Rainfall underestimated significantly.
Goddard 3ICE	More rainfall compared to 2ICE scheme. No significant impact on horizontal distribution. Multi-cellular structure.		No significant impact on horizontal distribution. Better agreement with observed rainfall compared to 2ICE scheme.	
Goddard Radiation	Less rainfall compared to simple 1-broad band radiation scheme. No significant impact on horizontal distribution.			
PLACE	Less rainfall compared to 1-layer surface model. No significant impact on horizontal distribution. Latent heat fluxes are affected by rainfall.			
3ICE, PLACE and Goddard Radiation	Off-shore flow in early morning. Propagating type. Location as observed. Heavy precipitation lasts 1-2 h longer than other runs. Most rainfall of all runs.	Heavy precipitation over central and southern Taiwan as observed. Most rainfall of all runs. Better rainfall amount.	Off-shore flow in early morning. Quasi-stationary type. Location as observed. Better rainfall amount.	Off-shore flow in early morning. Quasi-stationary type. Heavy precipitation over Strait but near S. Taiwan. Most rainfall of all runs. Better rainfall amount.
No Radiation	No off-shore flow. Heavy precipitation located along 900-1200 m elevation area. Precipitation is weak over slope area. Less rainfall compared to run with radiation.	No off-shore flow. Location as observed. Much less rainfall compared to run with radiation.	No off-shore flow. Quasi-stationary type. Precipitation located along 900-1200 m elevation area and over S. Taiwan as observed. More rainfall compared to run with radiation.	No off-shore flow. Quasi-stationary type. Heavy precipitation located over S. Taiwan as observed. Much less rainfall compared to run with radiation.

No Terrain	No-offshore flow. Eastward fast moving convective systems. Location and organization not as observed. 10% less rainfall compared to run with terrain.	No-offshore flow. Eastward fast moving convective systems. Location and organization not as observed. 20% less rainfall compared to run with terrain.	No-offshore flow. Location and organization not as observed. 7% less rainfall compared to run with terrain.	No-offshore flow. Quasi-stationary type. Heavy precipitation located over S. Taiwan as observed. Not much impact on total rainfall

Major Characteristics of Precipitation Structures and Results Simulated in Different Runs Using Different Physical Processes for Case 1 (August 10-11) and Case 2 (August 12-13)

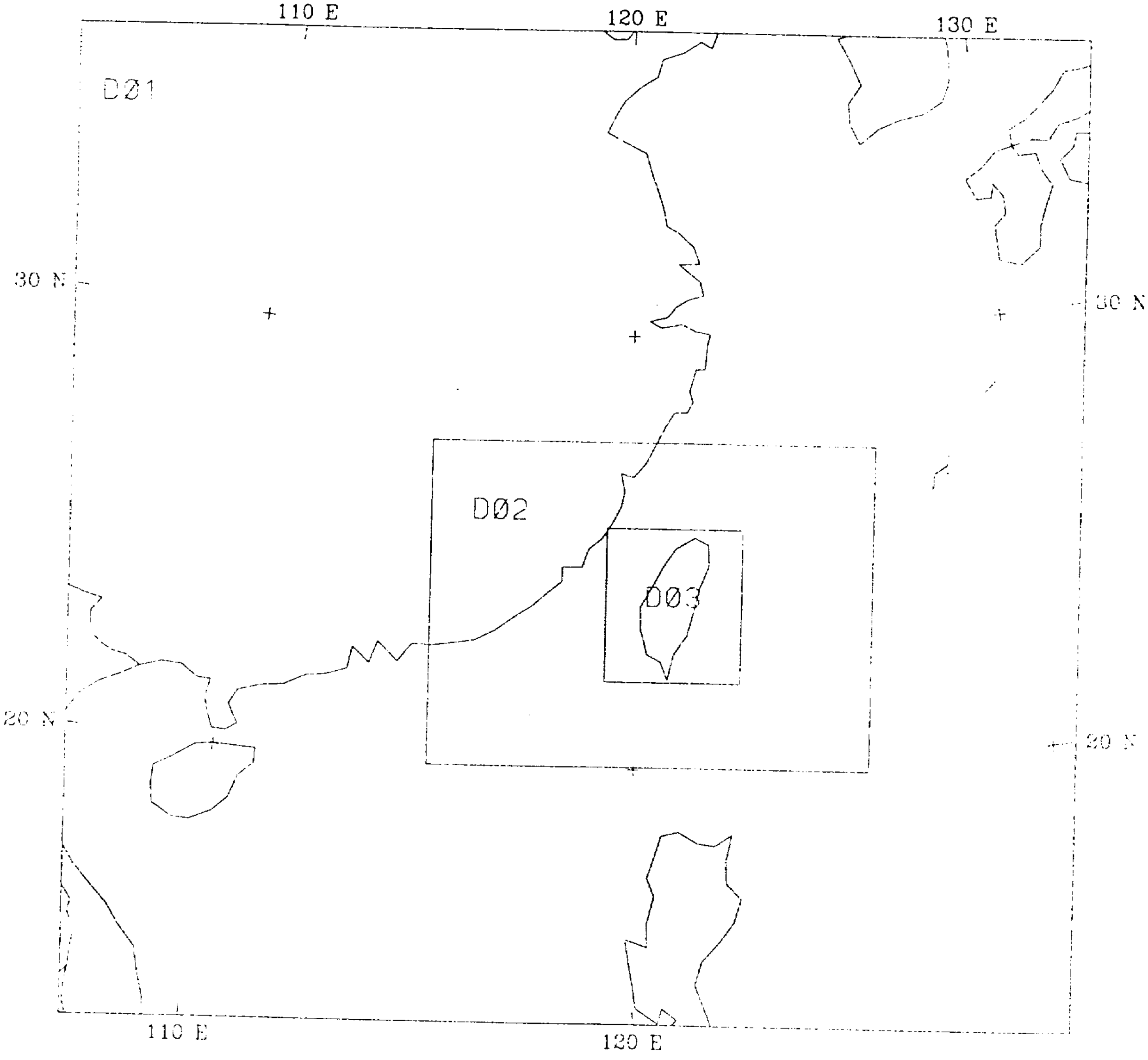

Fig. 1

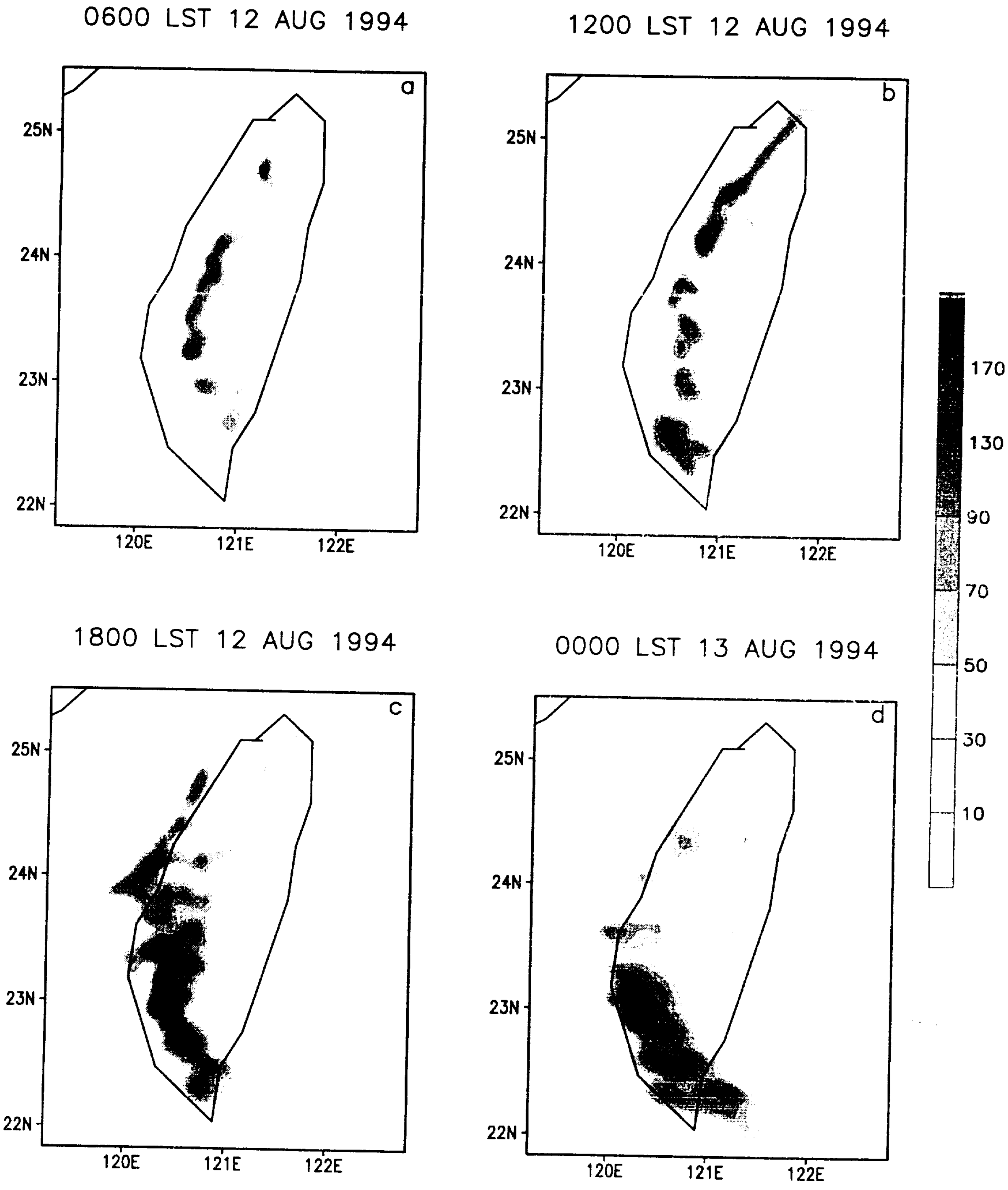

0600 LST 12 AUG 1994

1200 LST 12 AUG 1994

1800 LST 12 AUG 1994

0000 LST 13 AUG 1994

Fig. 23

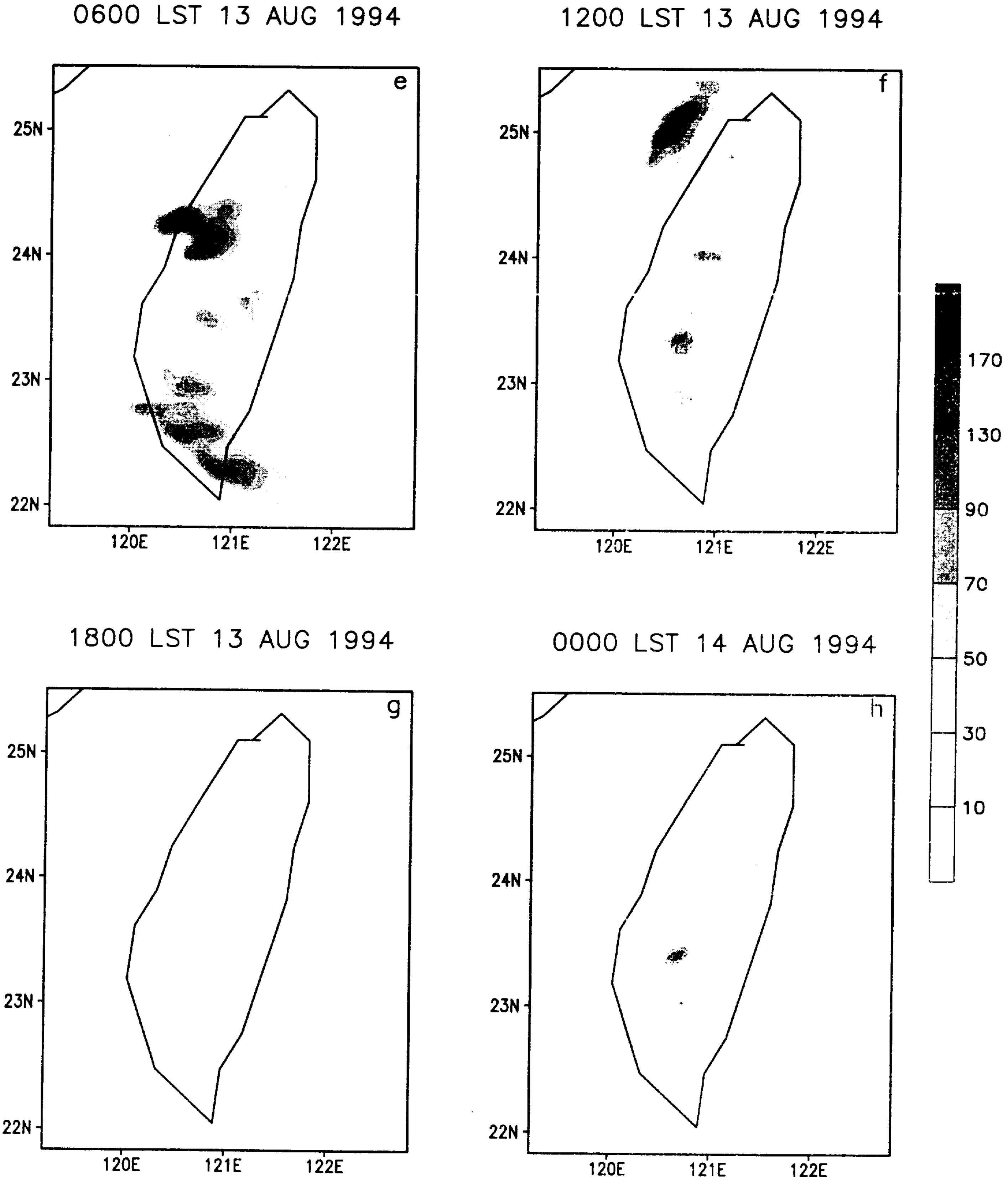
0600 LST 13 AUG 1994
e
1200 LST 13 AUG 1994
f
1800 LST 13 AUG 1994
g
0000 LST 14 AUG 1994
h
25N
24N
23N
22N
120E
121E
122E
170
130
90
70
50
30
10

Fig. 23 (Cont.)

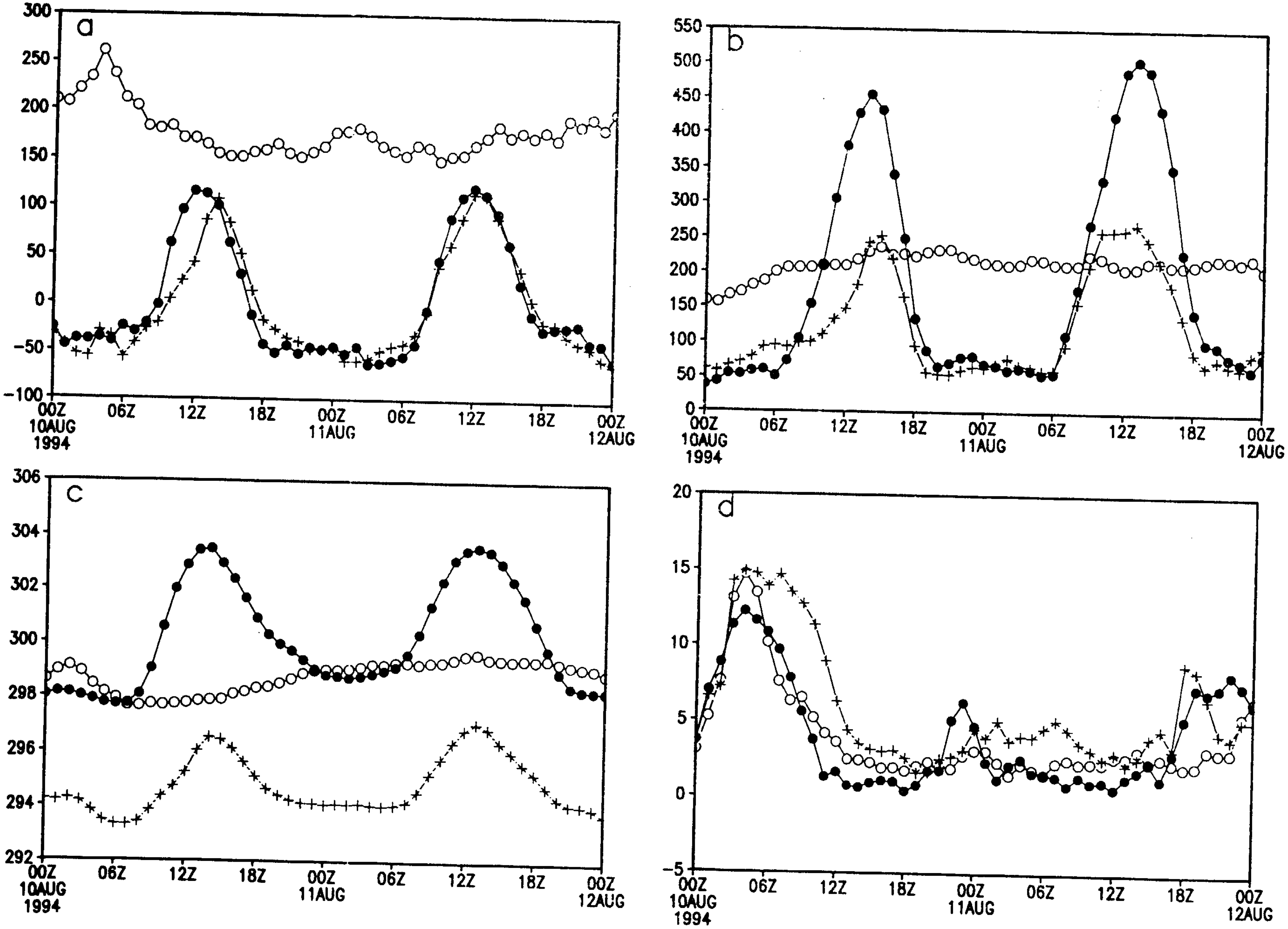
a
300
250
200
150
100
50
0
-50
-100
b
550
500
450
400
350
300
250
200
150
100
50
0
c
306
304
302
300
298
296
294
292
d
20
15
10
5
0
-5
00Z
10AUG
1994
06Z
12Z
18Z
00Z
11AUG
06Z
12Z
18Z
00Z
12AUG

Fig. 24

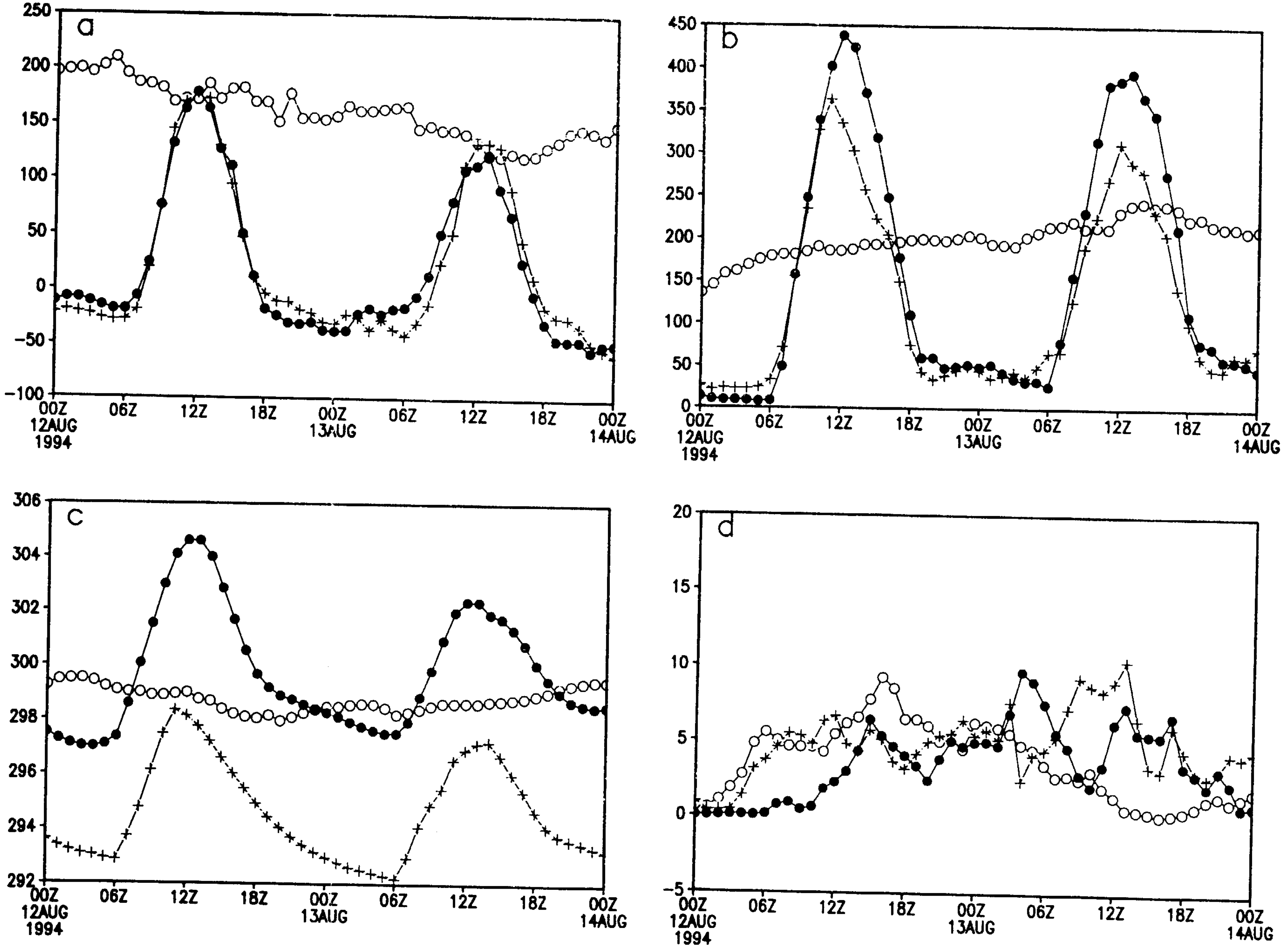
a
250
200
150
100
50
0
−50
−100
b
450
400
350
300
250
200
150
100
50
0
c
306
304
302
300
298
296
294
292
d
20
15
10
5
0
−5
00Z
12AUG
1994
06Z
12Z
18Z
00Z
13AUG
06Z
12Z
18Z
00Z
14AUG

Fig. 25

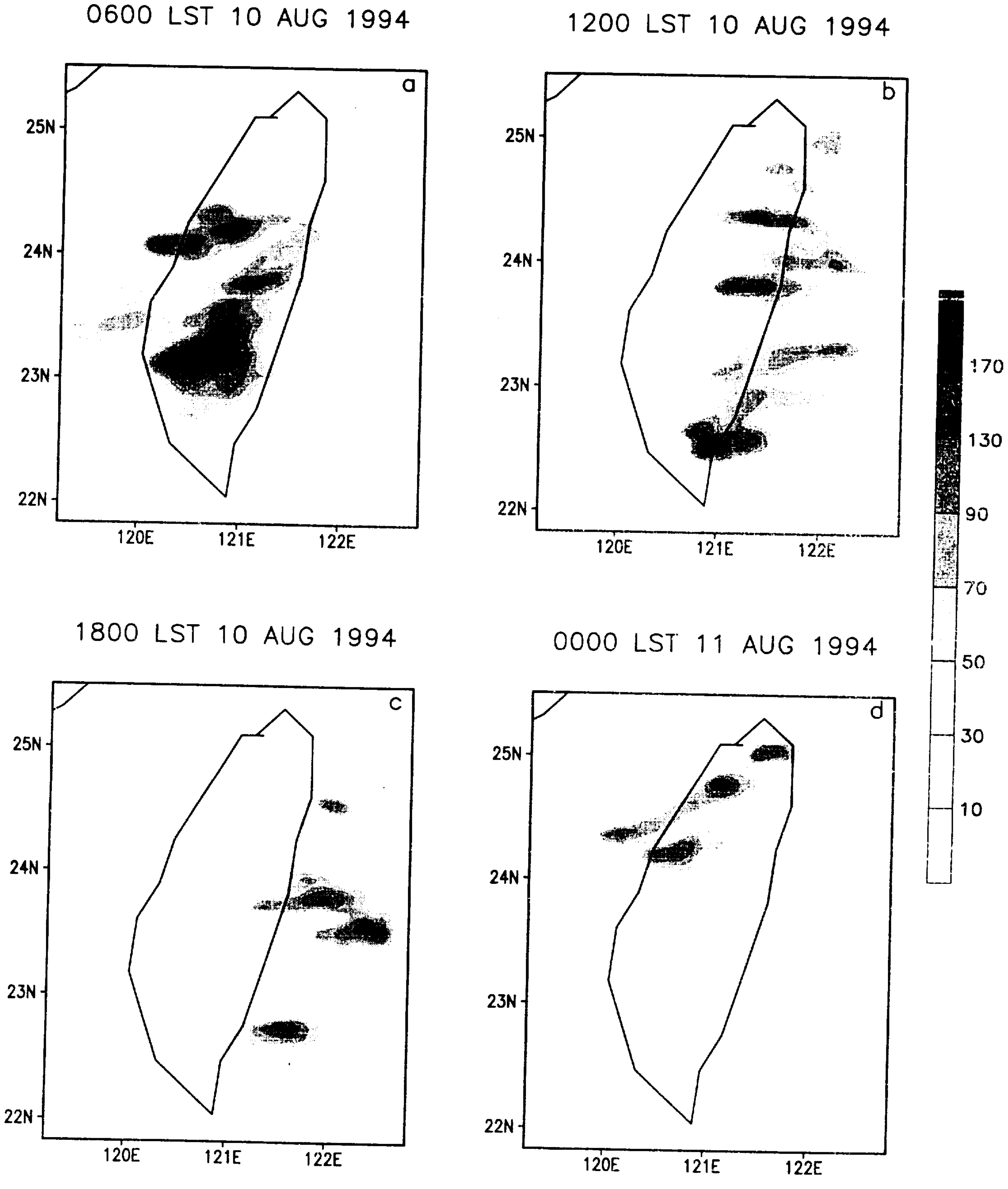

0600 LST 10 AUG 1994

1200 LST 10 AUG 1994

1800 LST 10 AUG 1994

0000 LST 11 AUG 1994

Fig. 26

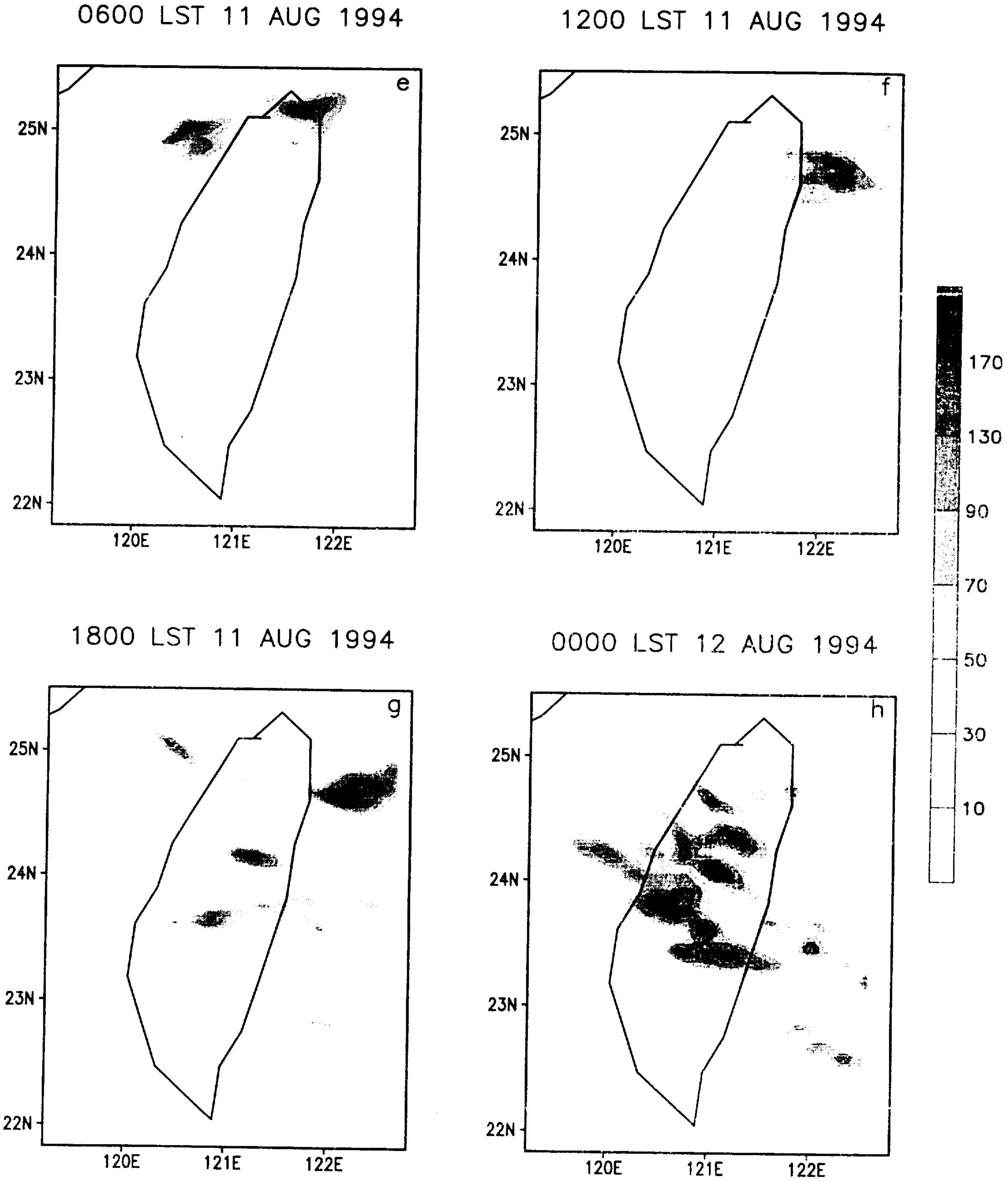
0600 LST 11 AUG 1994
1200 LST 11 AUG 1994
1800 LST 11 AUG 1994
0000 LST 12 AUG 1994
e
f
g
h
25N
24N
23N
22N
120E
121E
122E
170
130
90
70
50
30
10

Fig. 26 (Cont.)

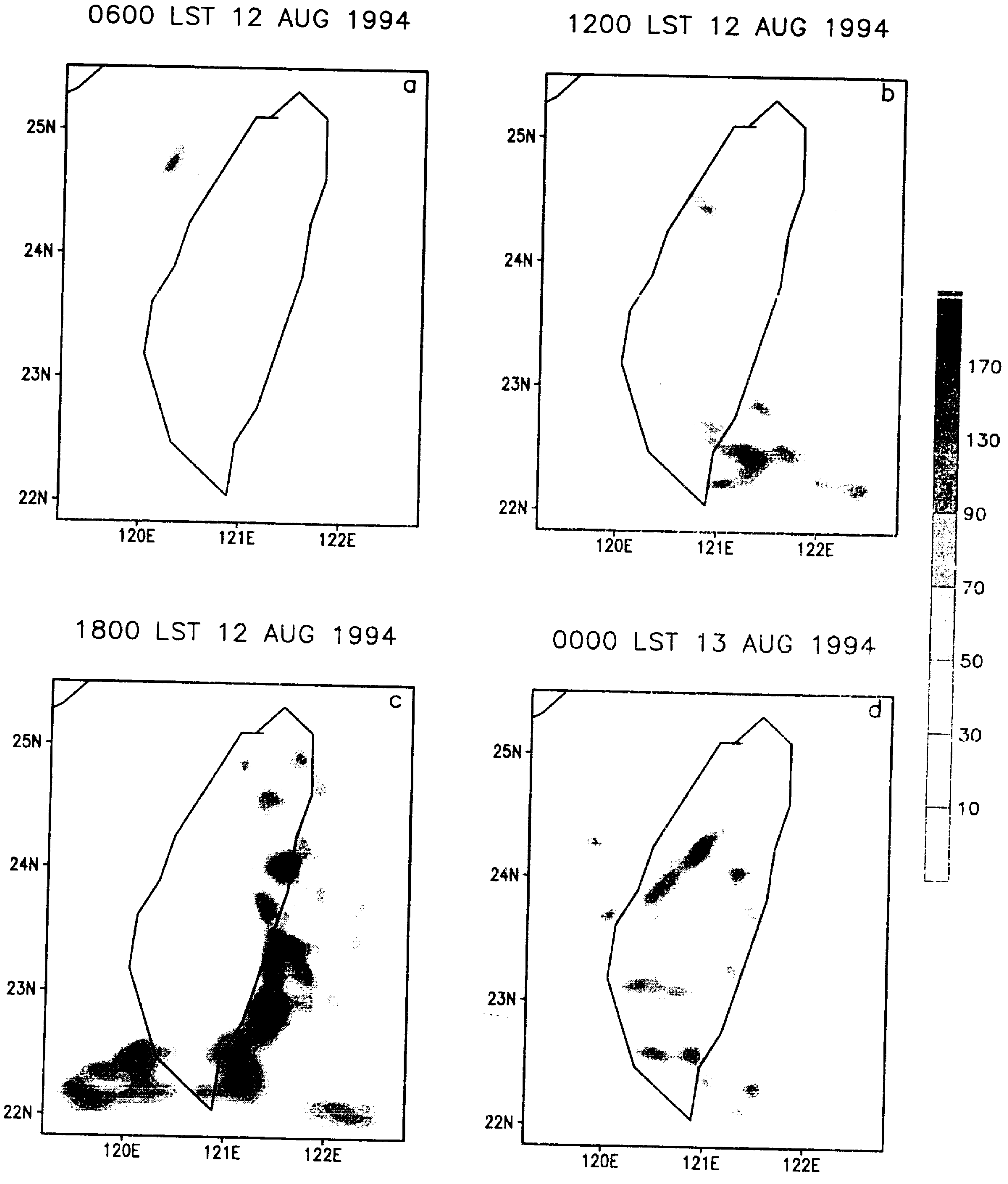

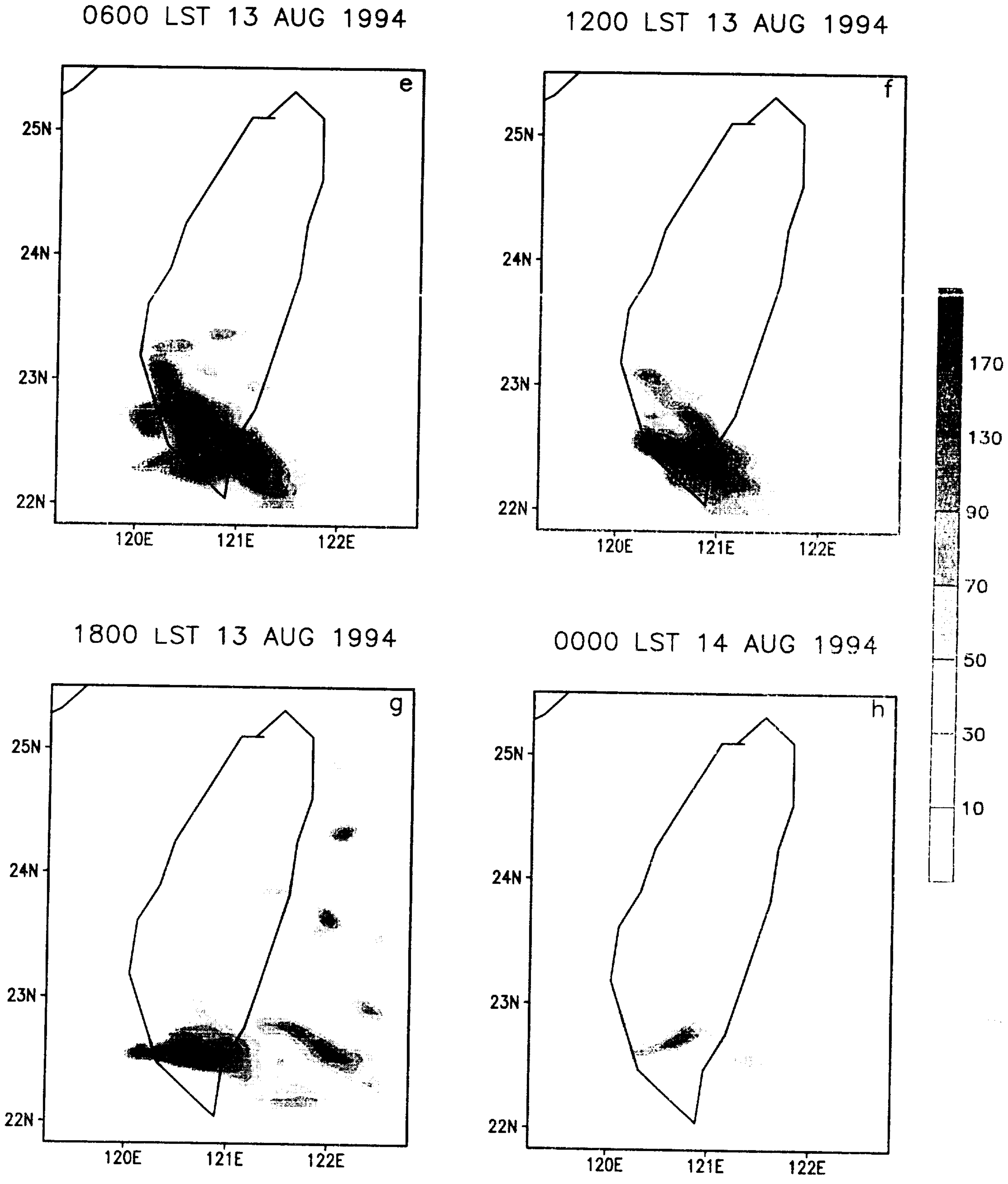
0600 LST 13 AUG 1994
e
1200 LST 13 AUG 1994
f
1800 LST 13 AUG 1994
g
0000 LST 14 AUG 1994
h
25N
24N
23N
22N
120E
121E
122E
170
130
90
70
50
30
10

Fig. 27 (Cont.)

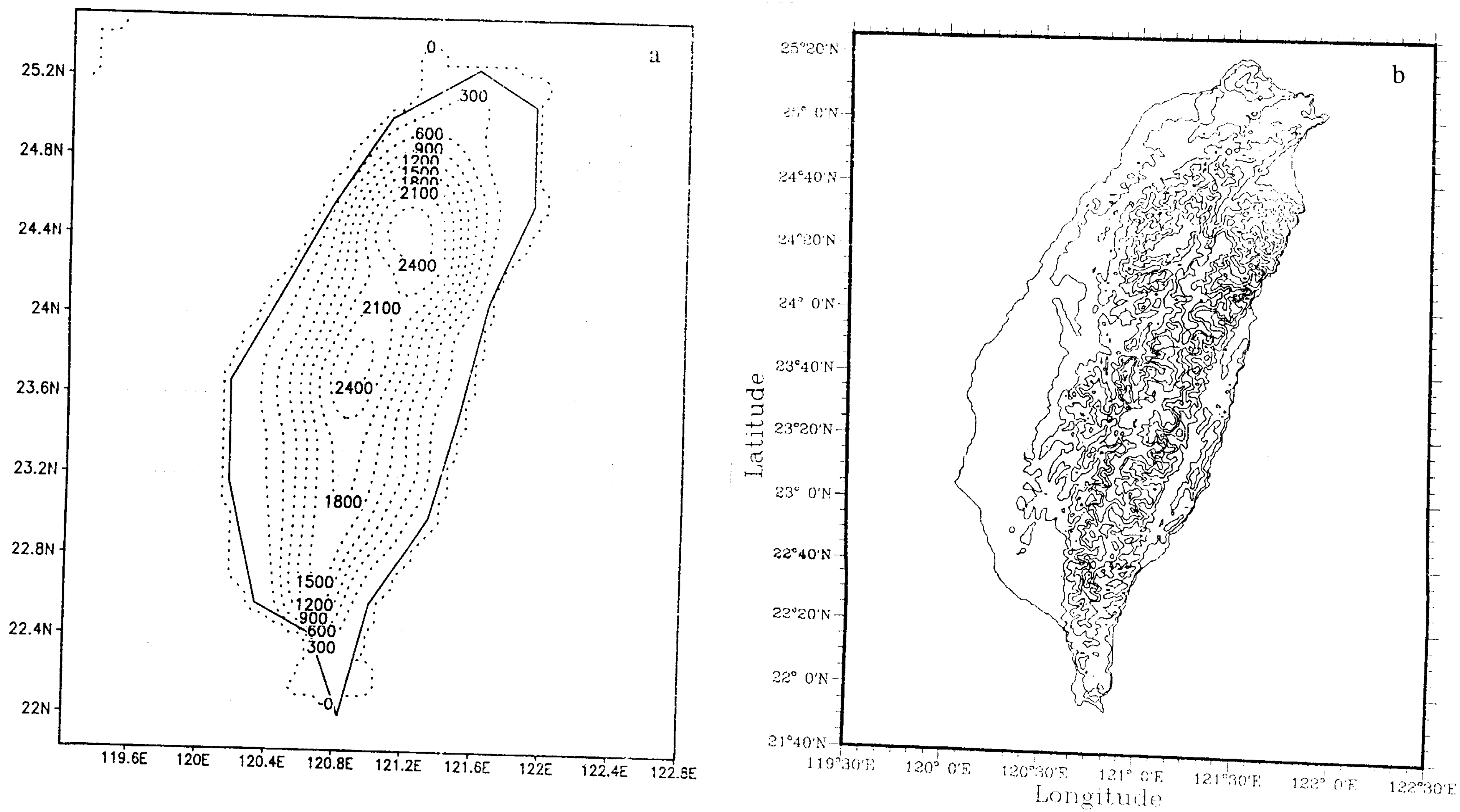
a
25.2N
24.8N
24.4N
24N
23.6N
23.2N
22.8N
22.4N
22N
119.6E
120E
120.4E
120.8E
121.2E
121.6E
122E
122.4E
122.8E
0
300
600
900
1200
1500
1800
2100
2400
2100
2400
1800
1500
1200
900
600
300
0
b
Latitude
25°20'N
25° 0'N
24°40'N
24°20'N
24° 0'N
23°40'N
23°20'N
23° 0'N
22°40'N
22°20'N
22° 0'N
21°40'N
119°30'E
120° 0'E
120°30'E
121° 0'E
121°30'E
122° 0'E
122°30'E
Longitude

Fig. 28

Parameterization for Land-Atmosphere-Cloud Exchange (PLACE): Model Schematic

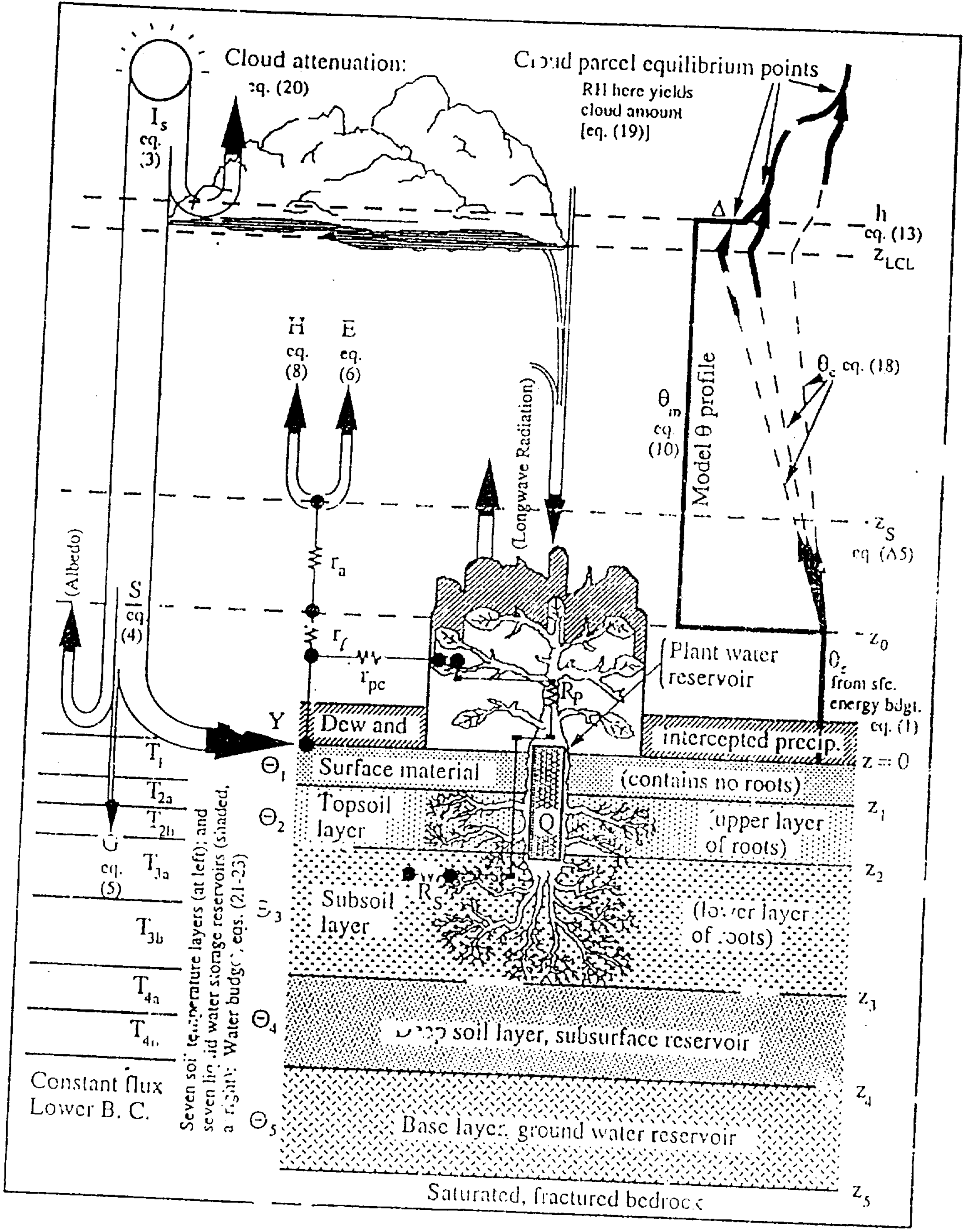

Fig. 2

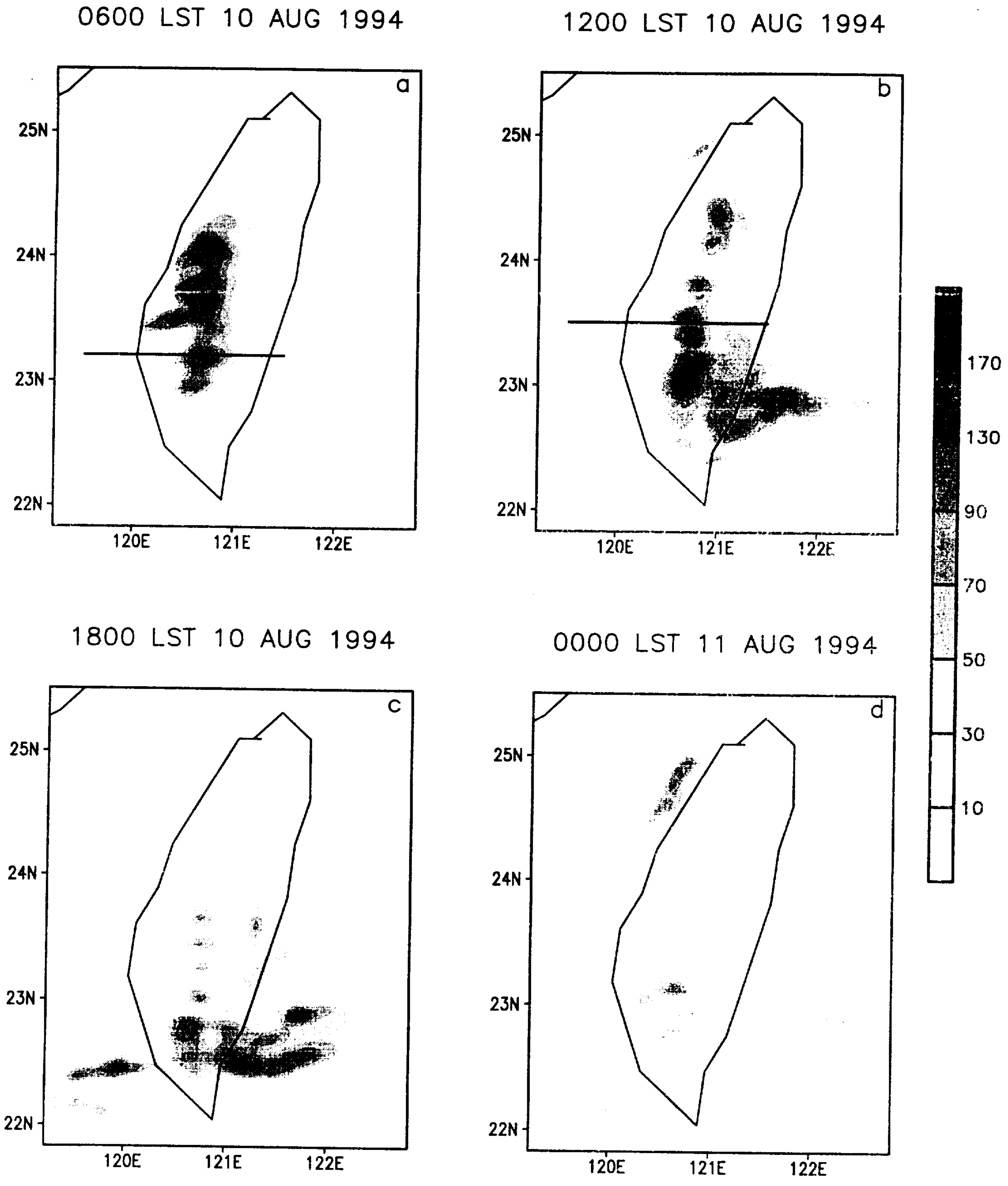
0600 LST 10 AUG 1994
1200 LST 10 AUG 1994
1800 LST 10 AUG 1994
0000 LST 11 AUG 1994
a
b
c
d
25N
24N
23N
22N
120E
121E
122E
170
130
90
70
50
30
10

Fig. 3

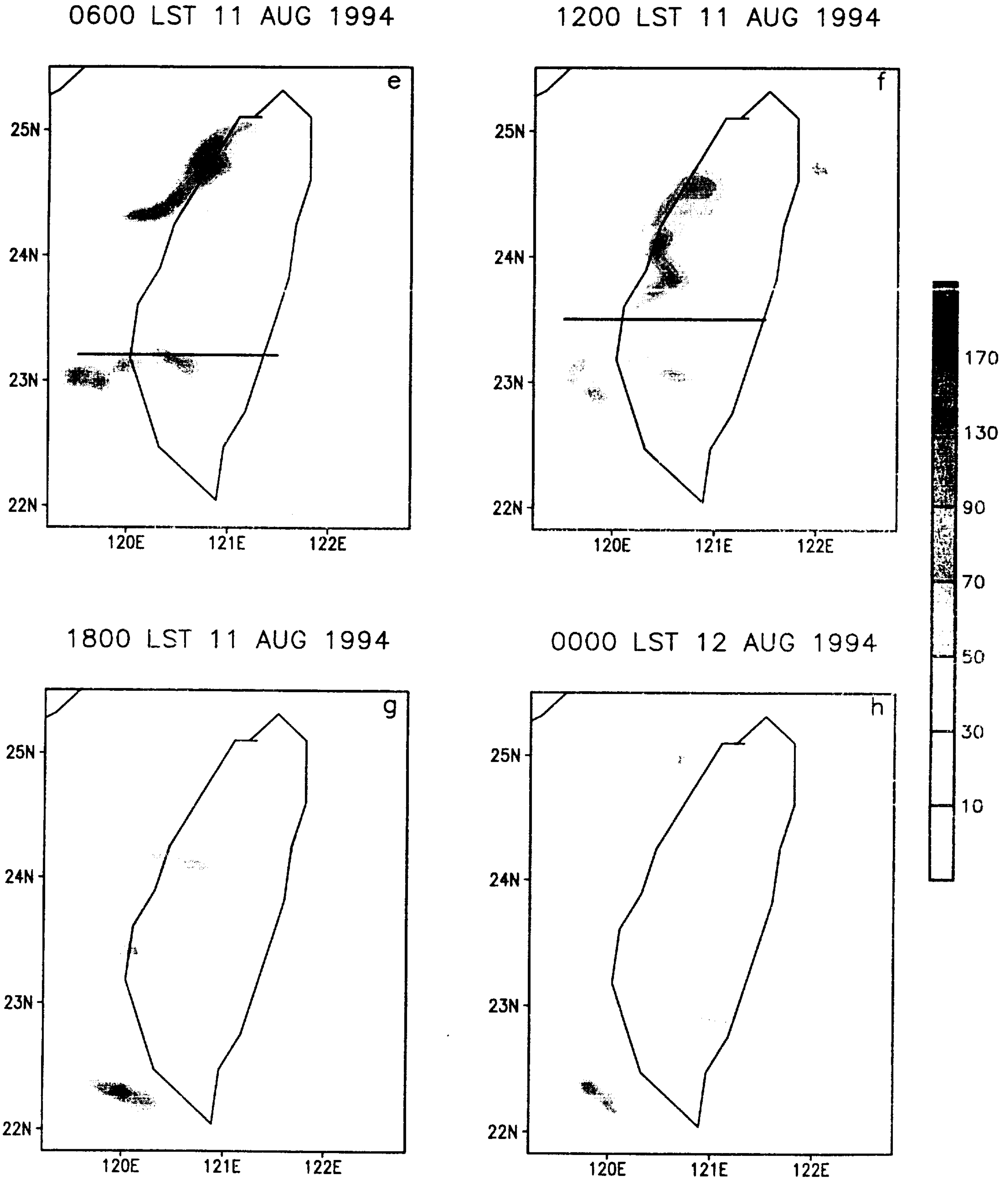
0600 LST 11 AUG 1994
e
1200 LST 11 AUG 1994
f
1800 LST 11 AUG 1994
g
0000 LST 12 AUG 1994
h
25N
24N
23N
22N
120E
121E
122E
170
130
90
70
50
30
10

Fig. 3 (Cont.)

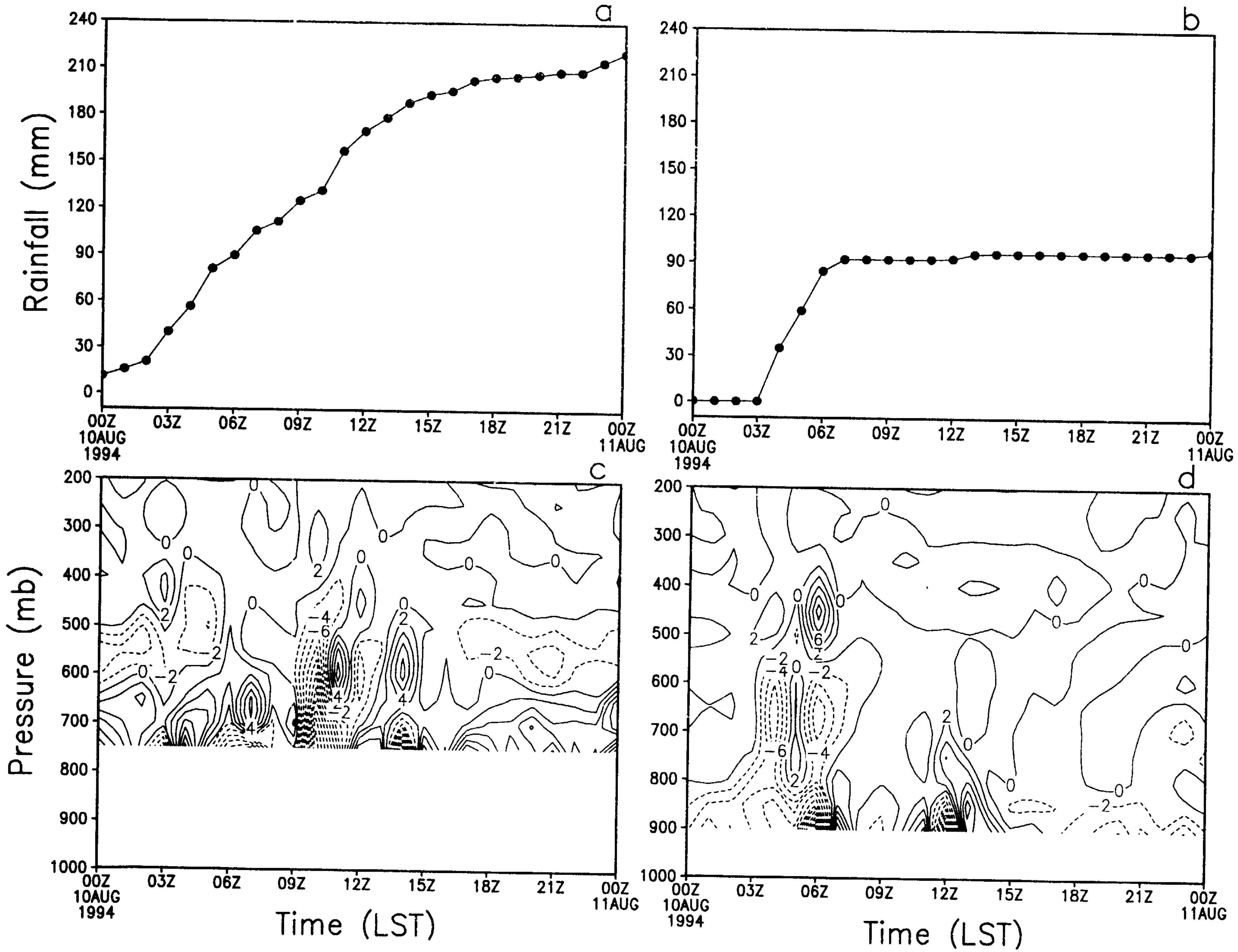
a
b
c
d
Rainfall (mm)
0
30
60
90
120
150
180
210
240
Pressure (mb)
200
300
400
500
600
700
800
900
1000
00Z 10AUG 1994
03Z
06Z
09Z
12Z
15Z
18Z
21Z
00Z 11AUG
Time (LST)
0
2
4
6
-2
-4
-6

Fig. 4

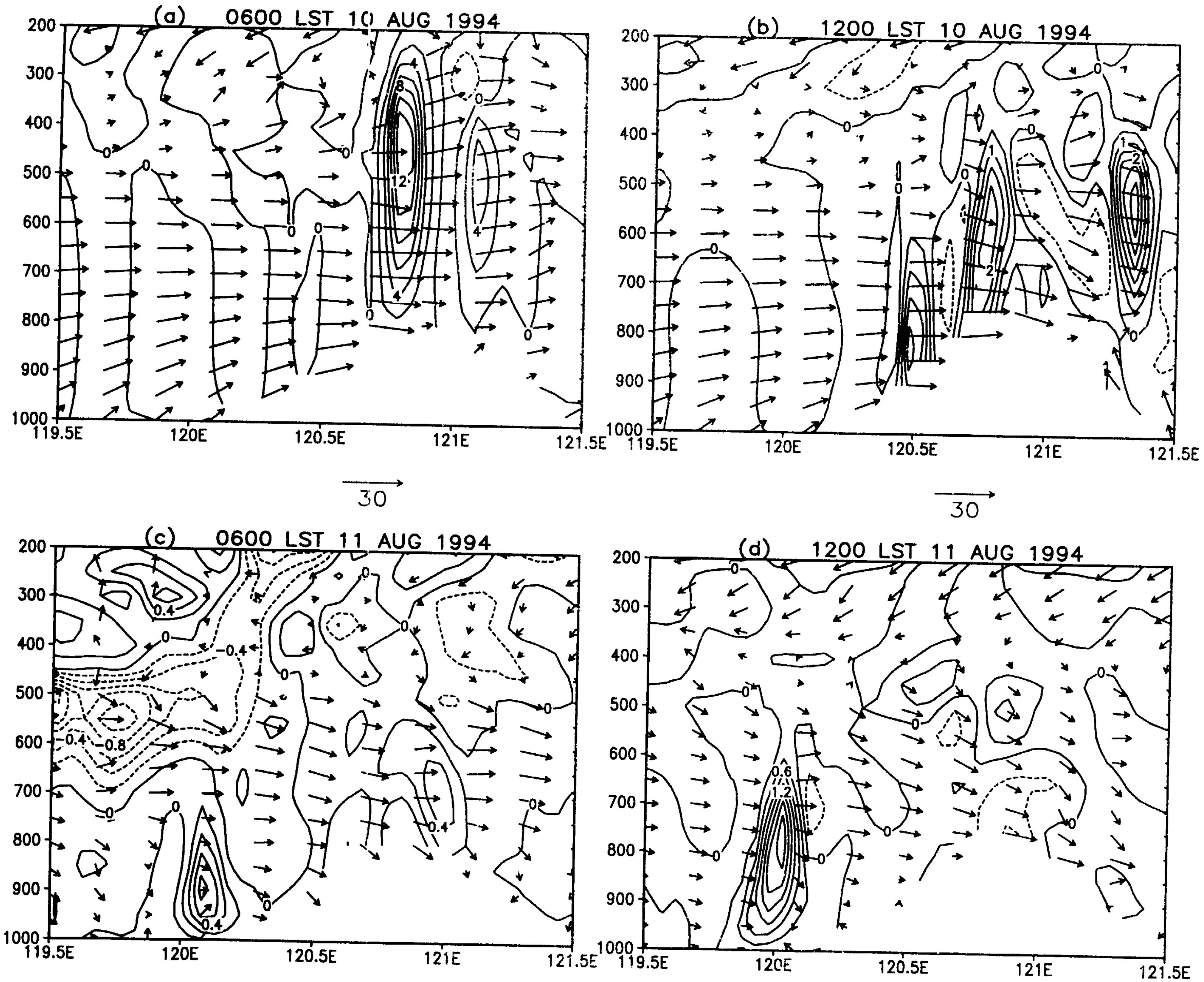
(a) 0600 LST 10 AUG 1994
(b) 1200 LST 10 AUG 1994
(c) 0600 LST 11 AUG 1994
(d) 1200 LST 11 AUG 1994
200
300
400
500
600
700
800
900
1000
119.5E
120E
120.5E
121E
121.5E
30
0
4
8
12
1
2
0.4
-0.4
-0.8
0.6
1.2

Fig. 5

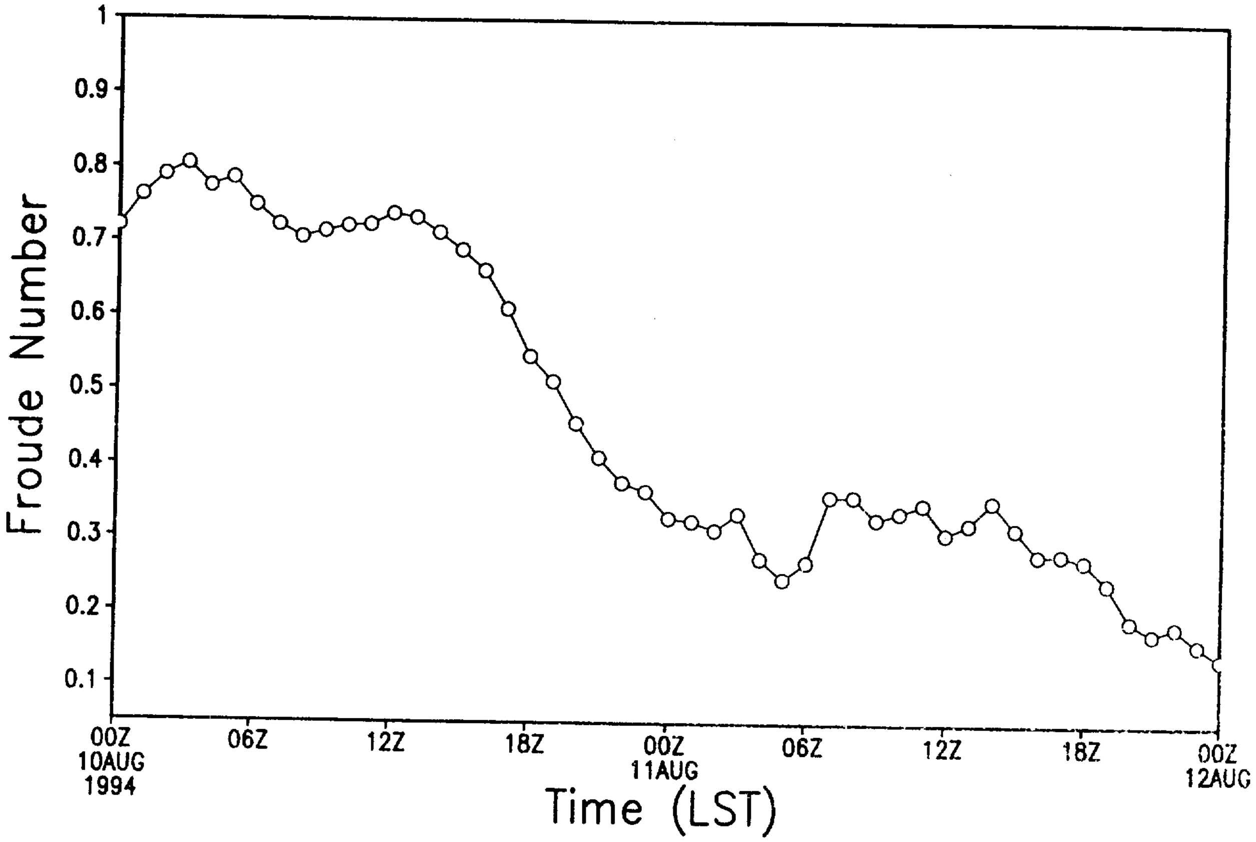

1
0.9
0.8
0.7
0.6
0.5
0.4
0.3
0.2
0.1
Froude Number
00Z
10AUG
1994
06Z
12Z
18Z
00Z
11AUG
06Z
12Z
18Z
00Z
12AUG
Time (LST)

Fig. 6

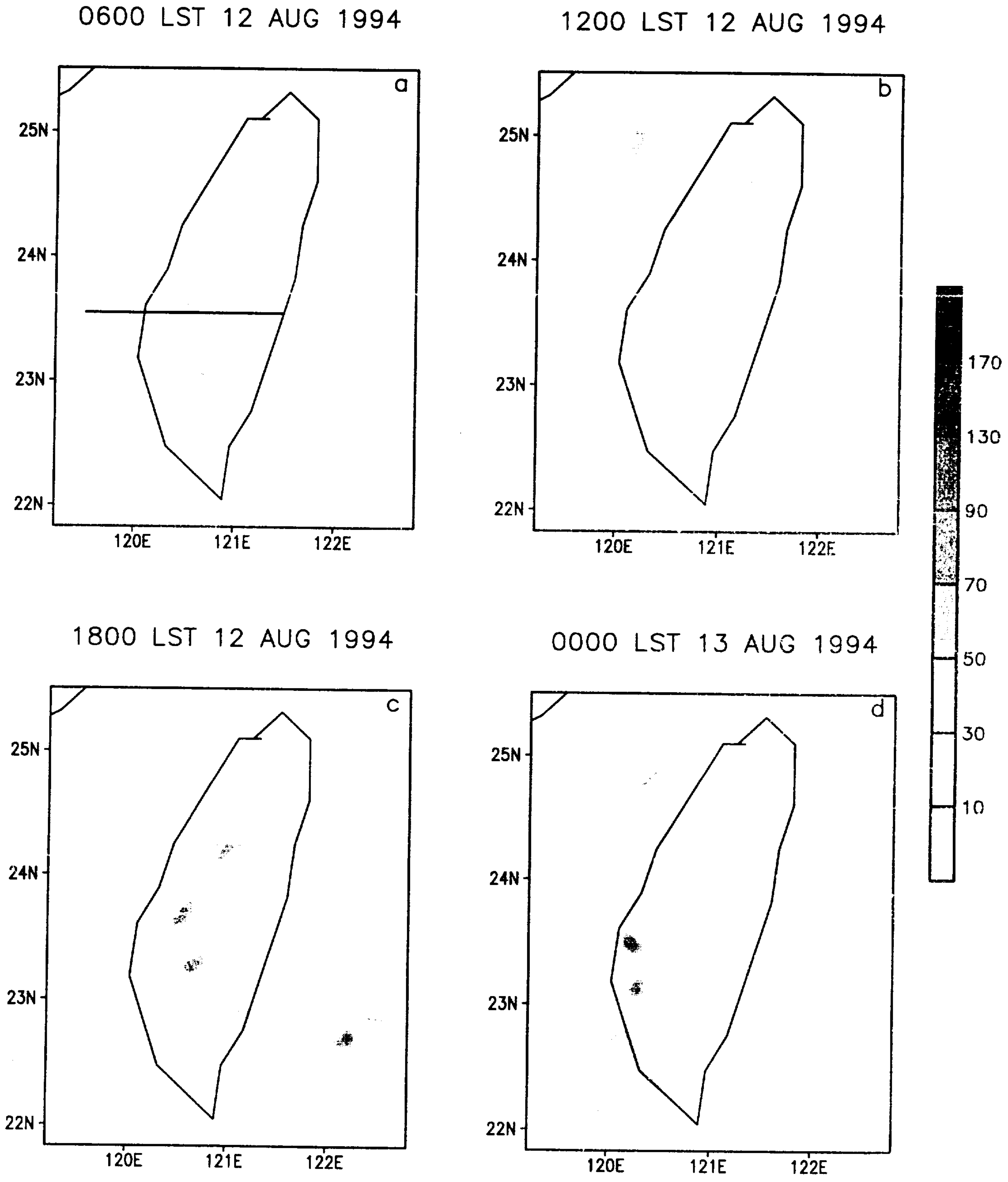

0600 LST 12 AUG 1994

1200 LST 12 AUG 1994

1800 LST 12 AUG 1994

0000 LST 13 AUG 1994

Fig. 7

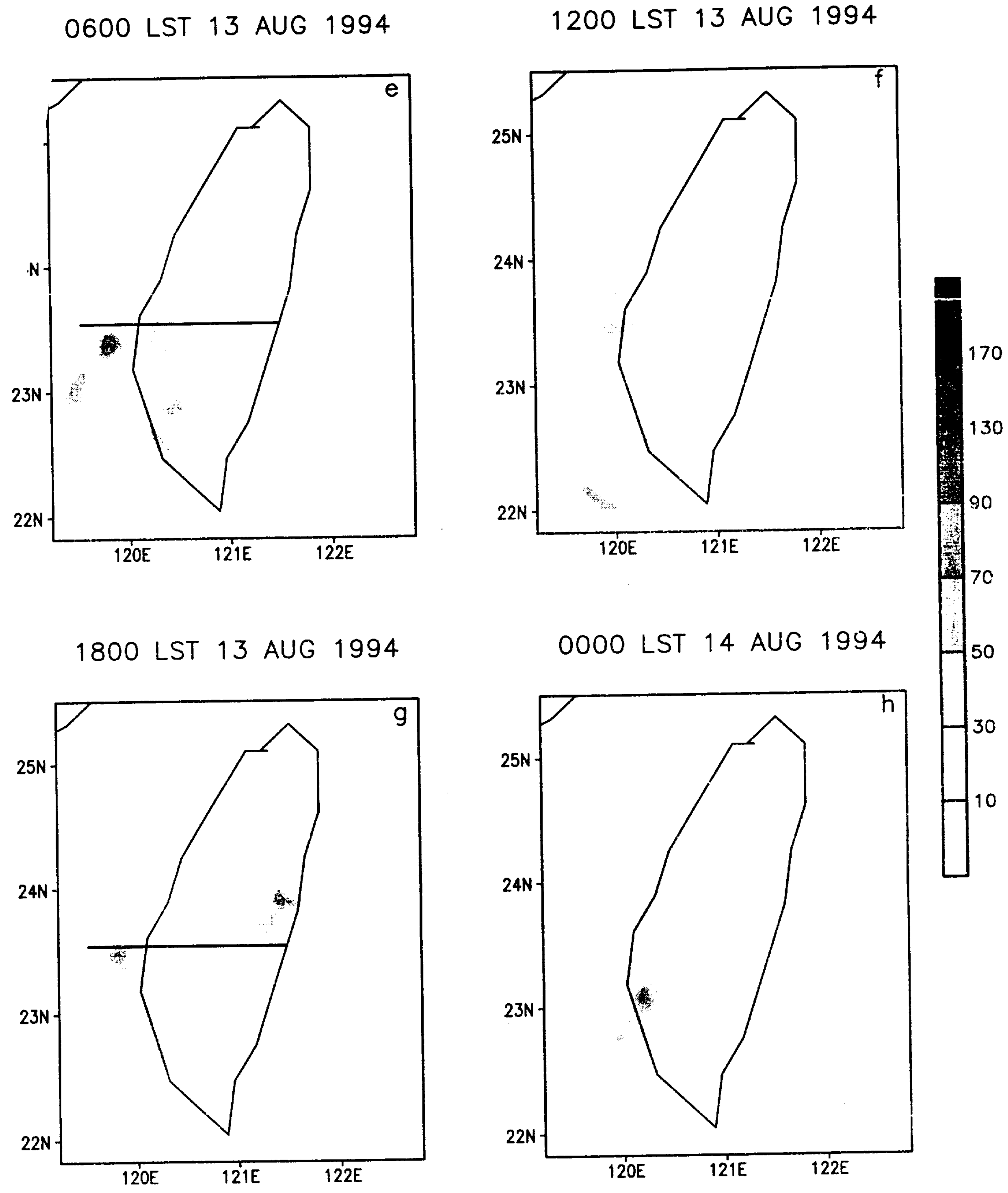
0600 LST 13 AUG 1994
e
N
23N
22N
120E
121E
122E
1200 LST 13 AUG 1994
f
25N
24N
23N
22N
120E
121E
122E
1800 LST 13 AUG 1994
g
25N
24N
23N
22N
120E
121E
122E
0000 LST 14 AUG 1994
h
25N
24N
23N
22N
120E
121E
122E
170
130
90
70
50
30
10

Fig. 7 (Con

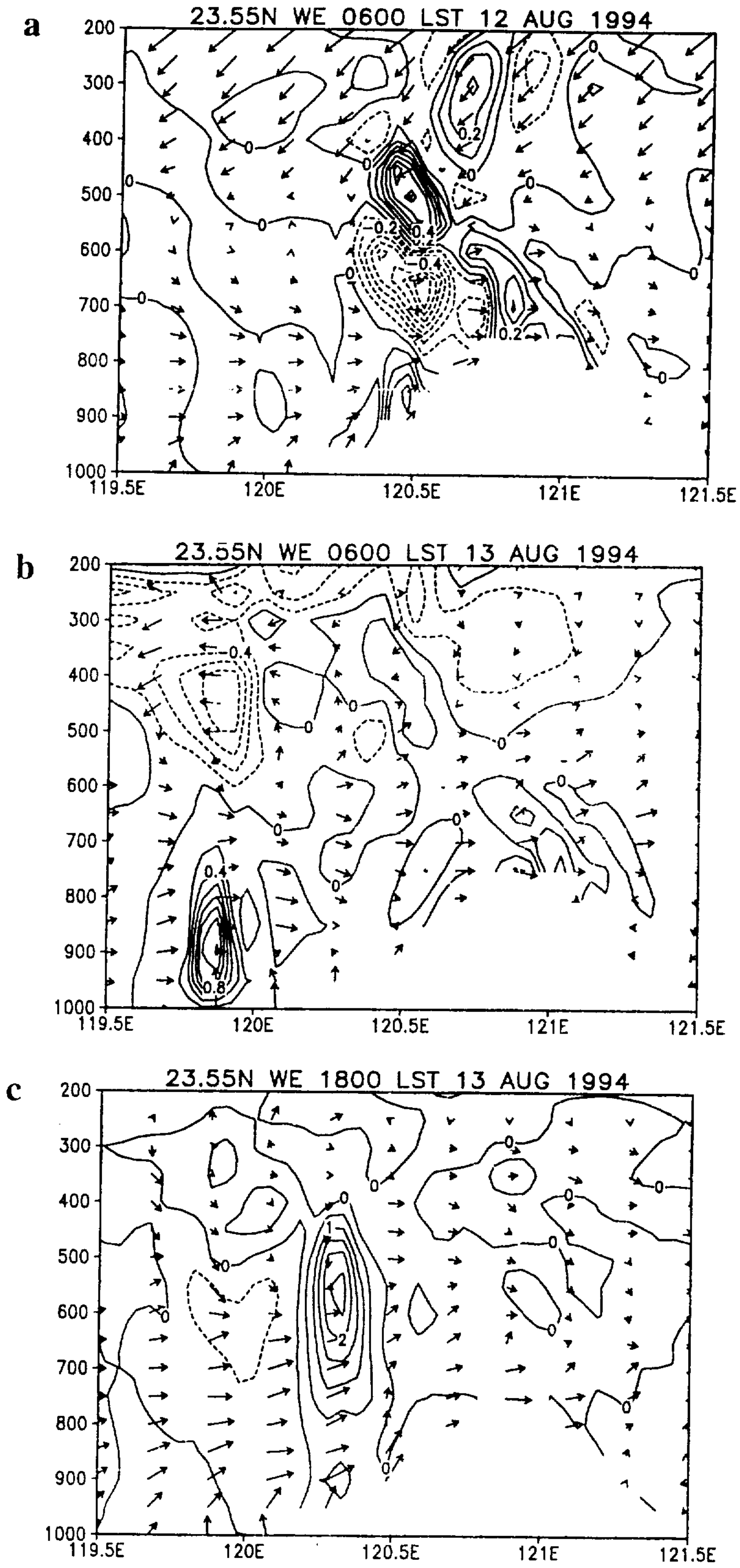
a
23.55N WE 0600 LST 12 AUG 1994
b
23.55N WE 0600 LST 13 AUG 1994
c
23.55N WE 1800 LST 13 AUG 1994
200
300
400
500
600
700
800
900
1000
119.5E
120E
120.5E
121E
121.5E
0
0.2
-0.2
0.4
-0.4
0.8
1
2

Fig. 8

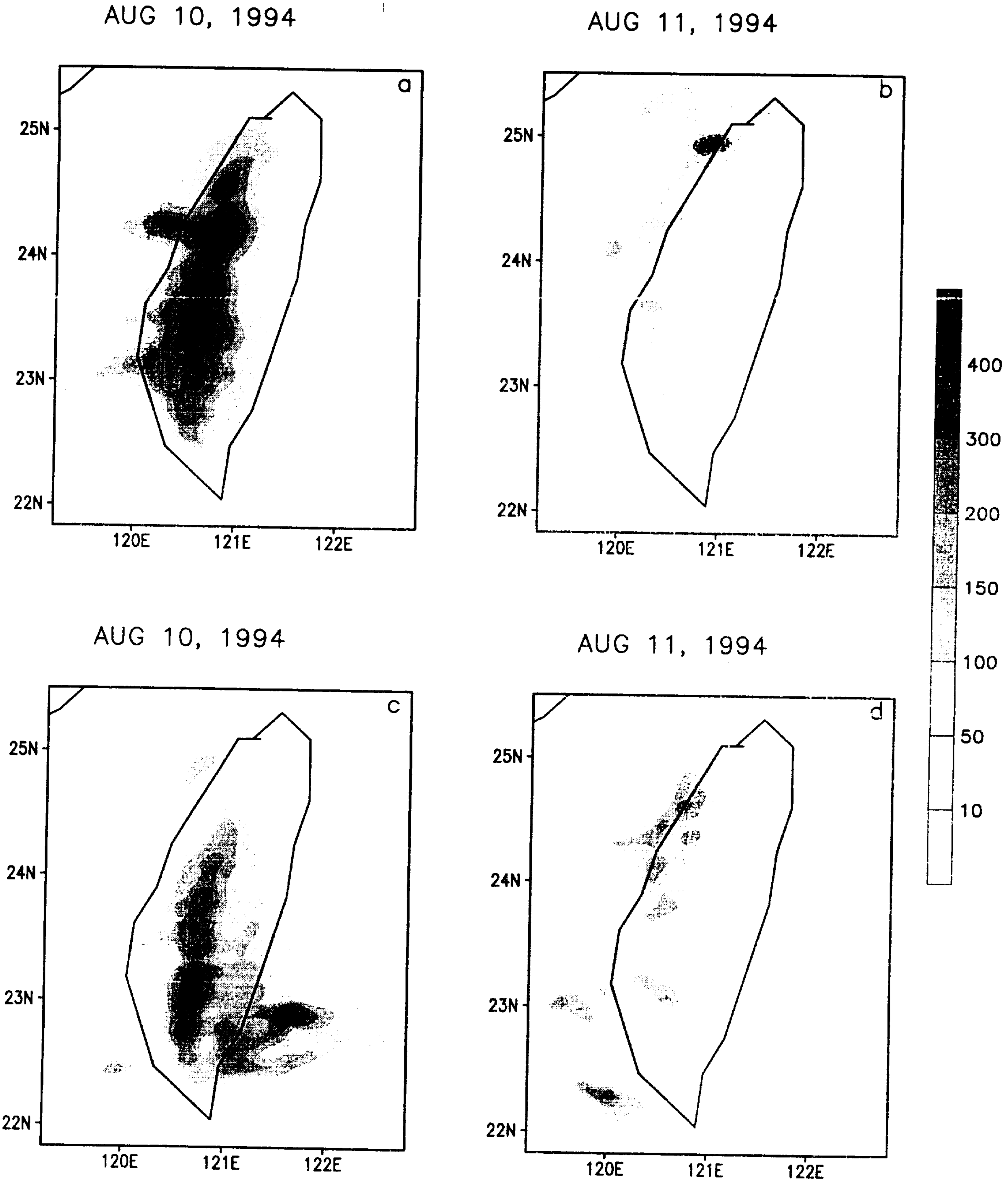

AUG 10, 1994

AUG 11, 1994

AUG 10, 1994

AUG 11, 1994

Fig. 9

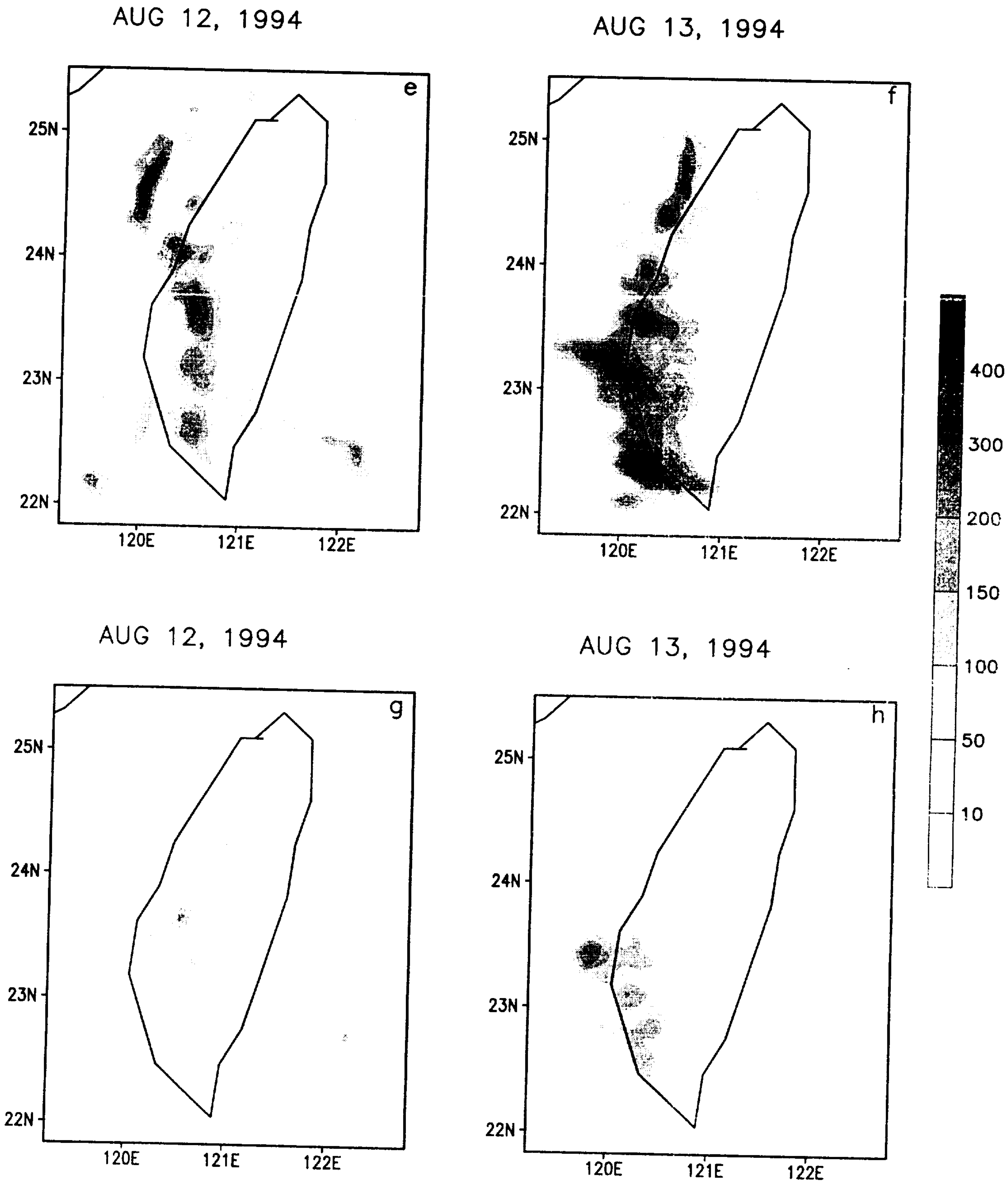
AUG 12, 1994
e
AUG 13, 1994
f
AUG 12, 1994
g
AUG 13, 1994
h
25N
24N
23N
22N
120E
121E
122E
400
300
200
150
100
50
10

Fig. 9 (Cont.)

Fig. 11

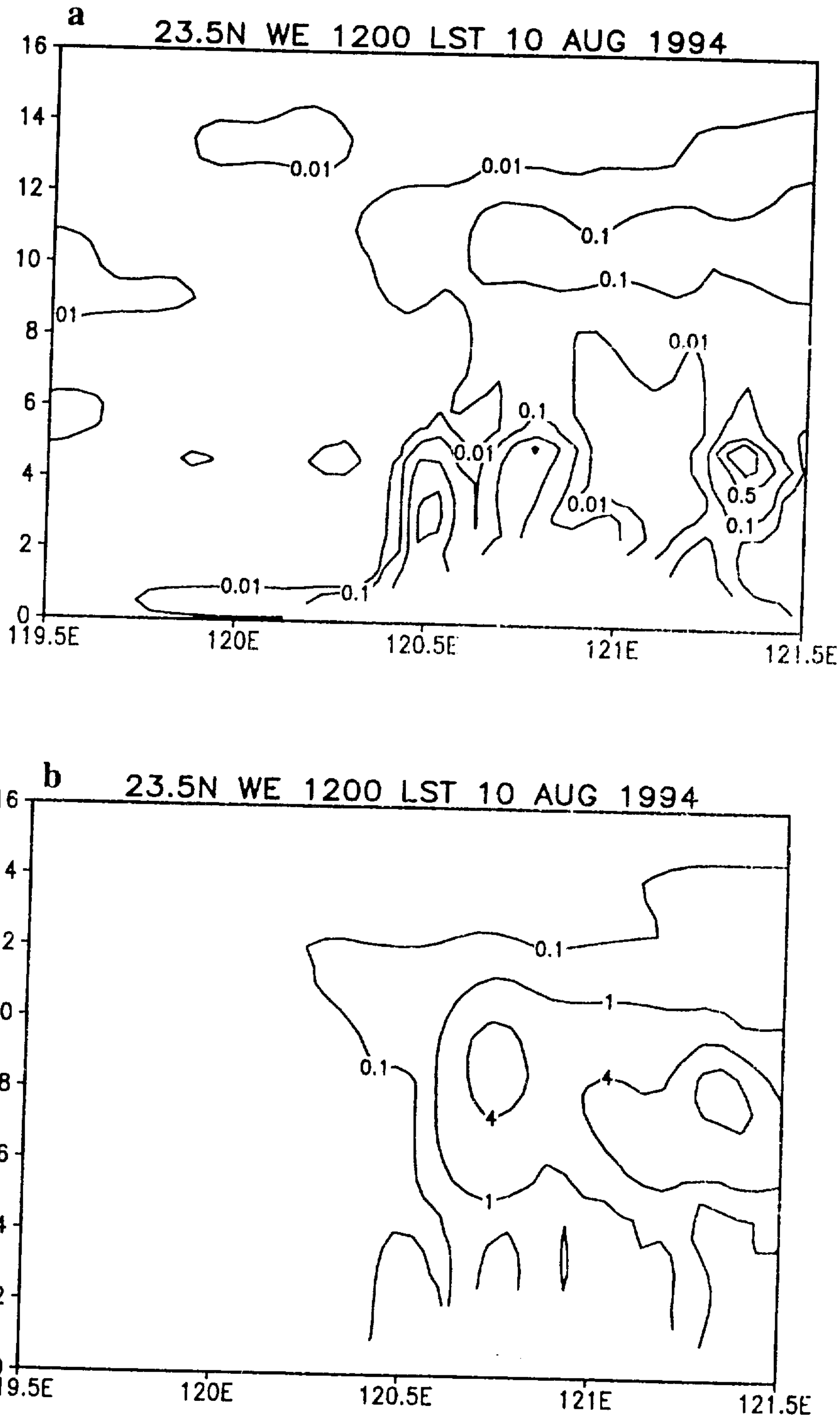
a
23.5N WE 1200 LST 10 AUG 1994
16
14
12
10
8
6
4
2
0
119.5E
120E
120.5E
121E
121.5E
0.01
0.01
01
0.1
0.1
0.01
0.1
0.01
0.01
0.5
0.1
0.01
0.1
b
23.5N WE 1200 LST 10 AUG 1994
16
14
12
10
8
6
4
2
0
119.5E
120E
120.5E
121E
121.5E
0.1
1
0.1
4
4
1

Fig.

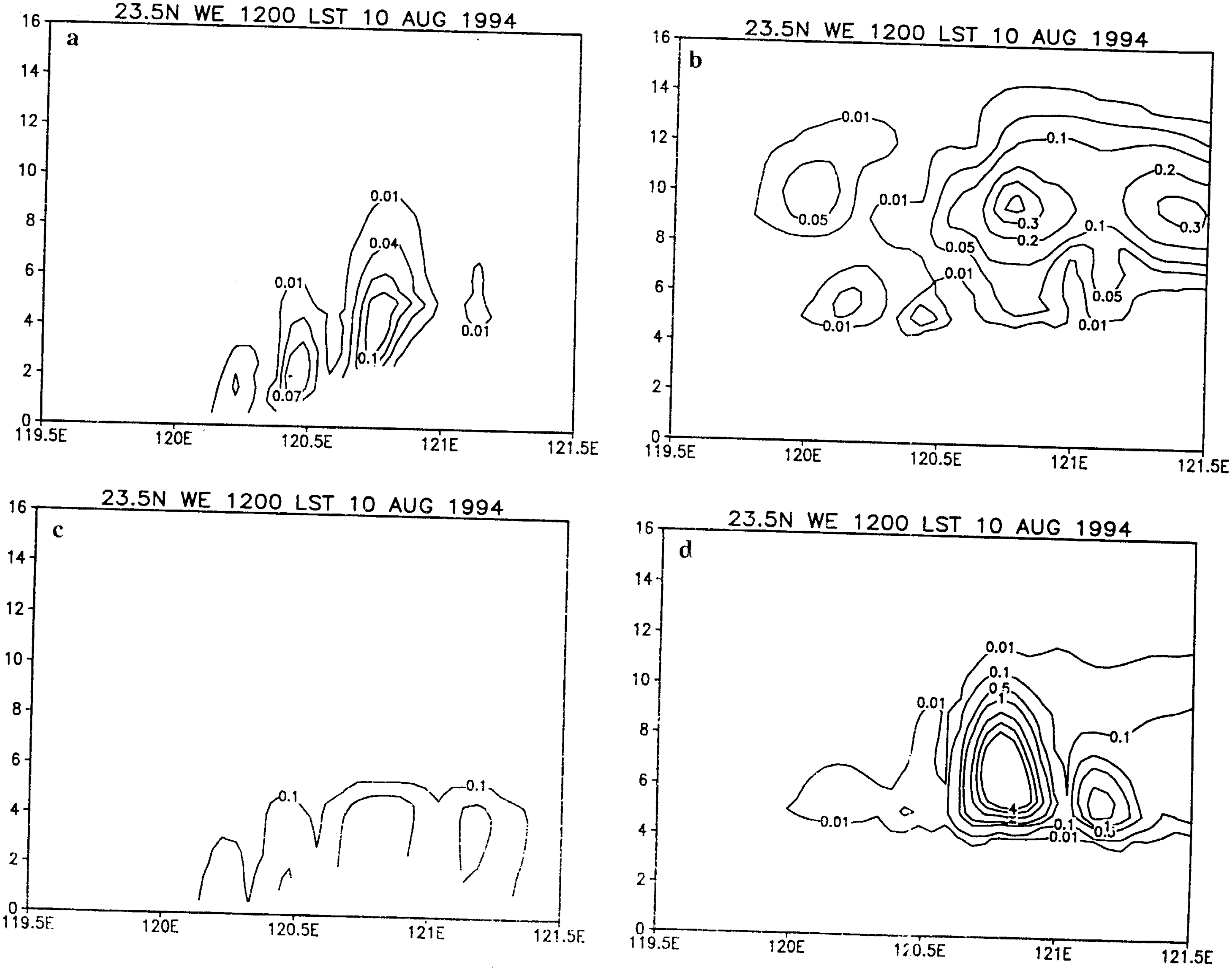
23.5N WE 1200 LST 10 AUG 1994
a
b
c
d
0
2
4
6
8
10
12
14
16
119.5E
120E
120.5E
121E
121.5E
0.01
0.04
0.07
0.1
0.05
0.2
0.3
0.5
1
4

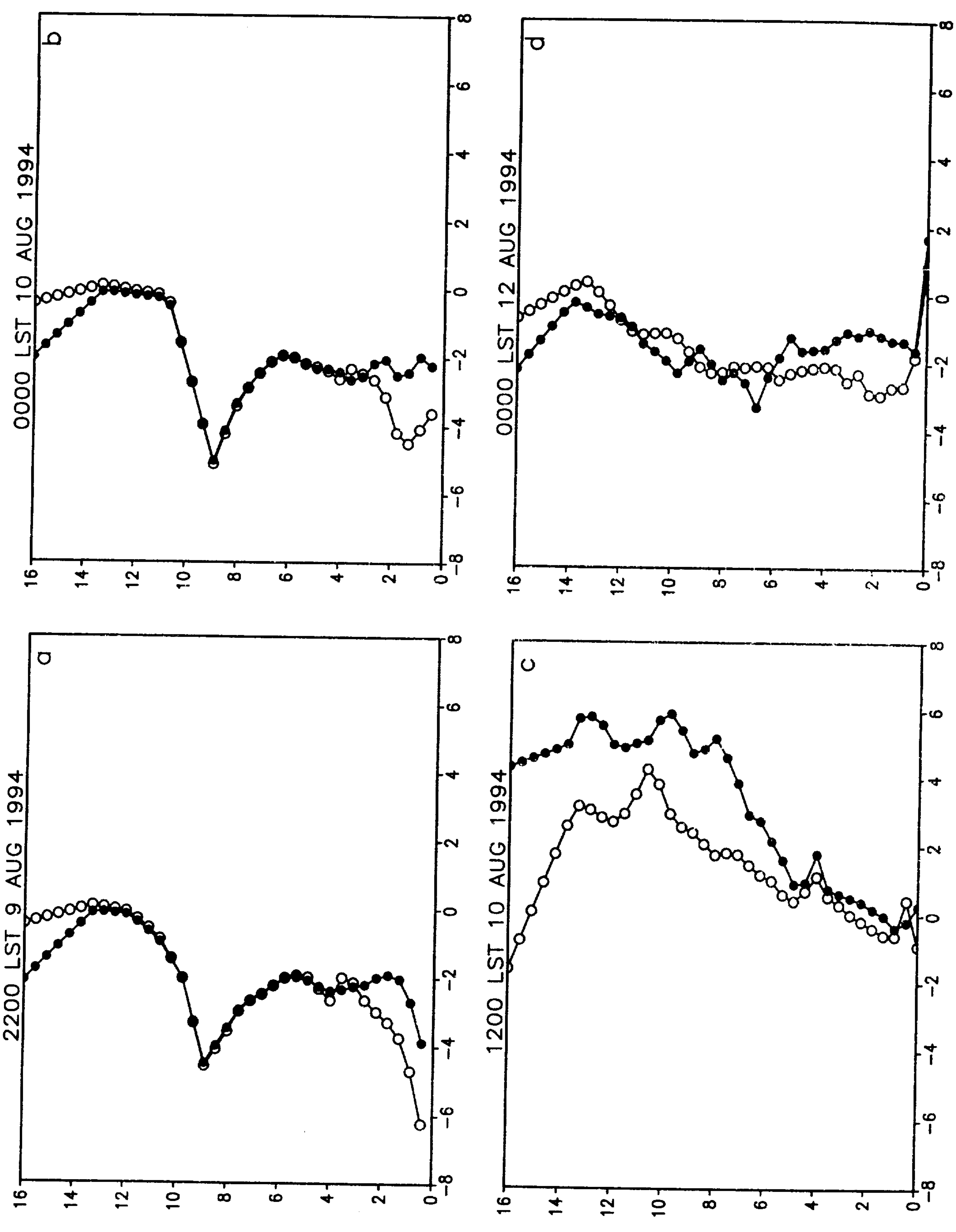
2200 LST 9 AUG 1994
a
0000 LST 10 AUG 1994
b
1200 LST 10 AUG 1994
c
0000 LST 12 AUG 1994
d
16
14
12
10
8
6
4
2
0
−8
−6
−4
−2
0
2
4
6
8

Fig. 12

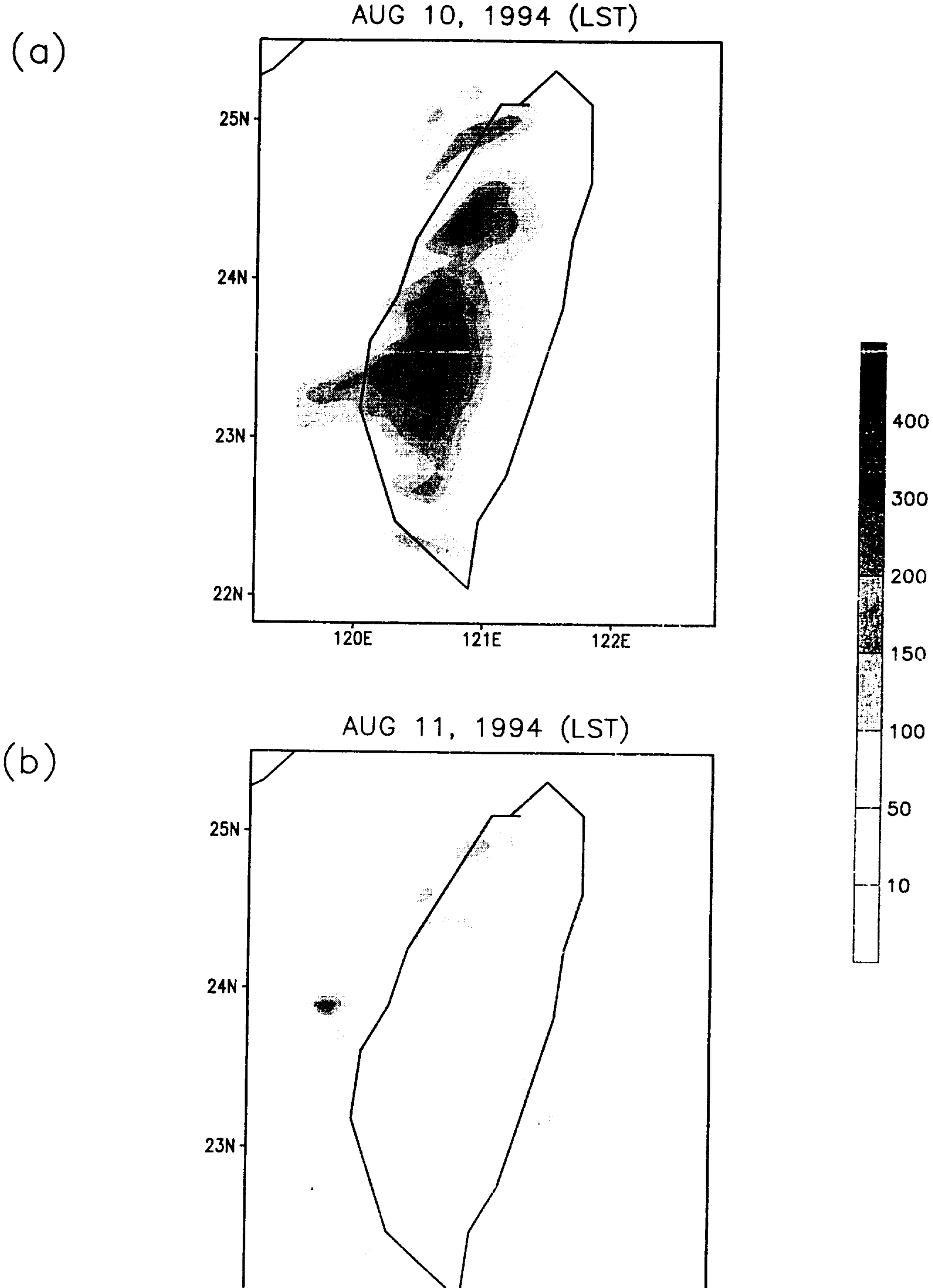
(a)
AUG 10, 1994 (LST)
25N
24N
23N
22N
120E
121E
122E
(b)
AUG 11, 1994 (LST)
25N
24N
23N
22N
120E
121E
122E
400
300
200
150
100
50
10

Fig. 13

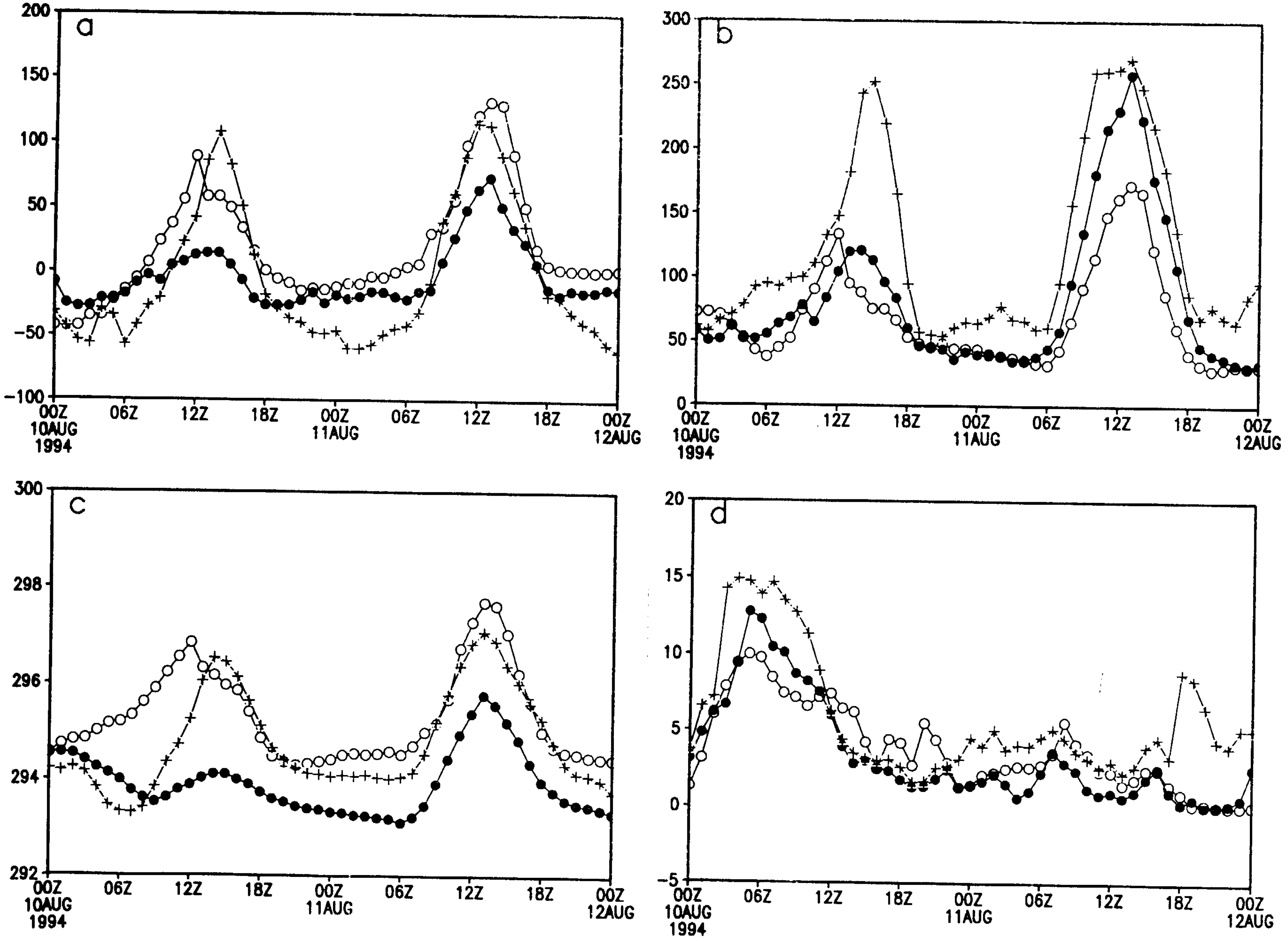
a
200
150
100
50
0
−50
−100
b
300
250
200
150
100
50
0
c
300
298
296
294
292
d
20
15
10
5
0
−5
00Z 10AUG 1994
06Z
12Z
18Z
00Z 11AUG
06Z
12Z
18Z
00Z 12AUG

Fig. 14

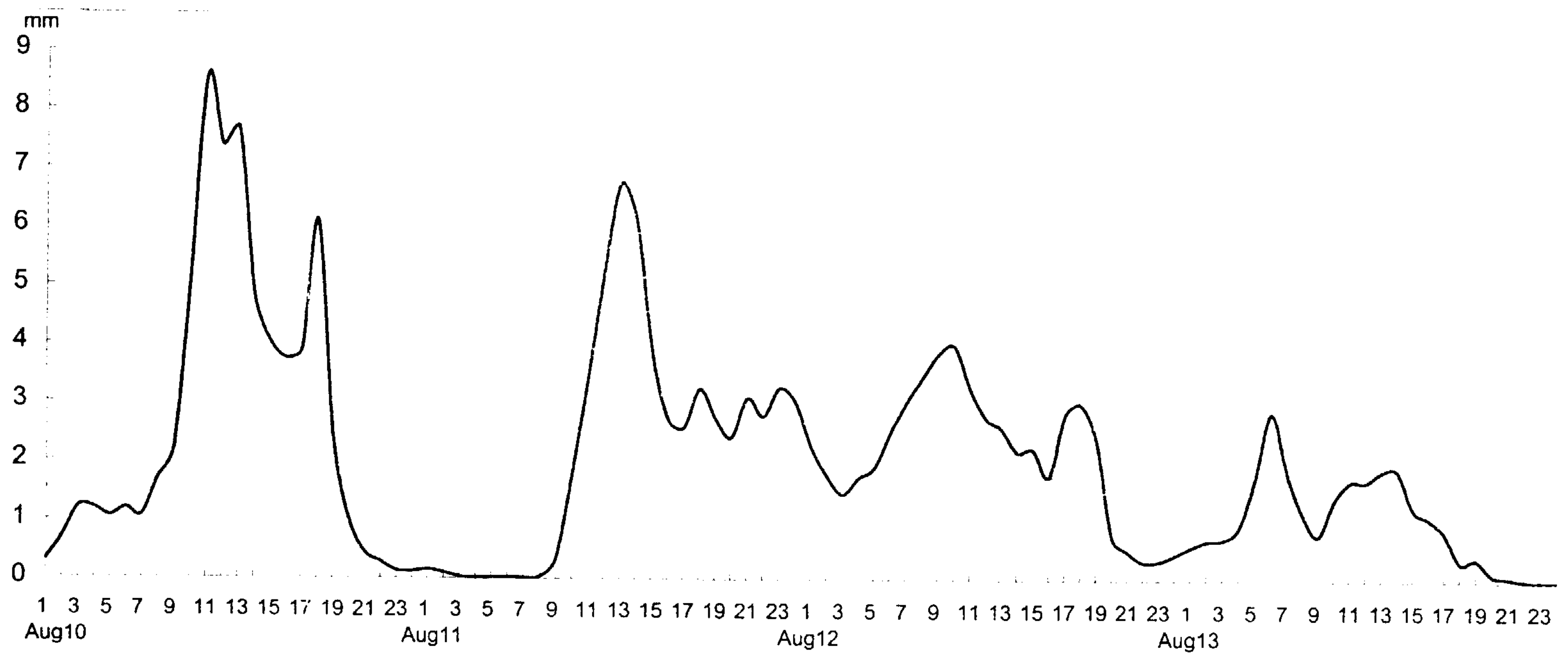mm
9
8
7
6
5
4
3
2
1
0
1 3 5 7 9 11 13 15 17 19 21 23 1 3 5 7 9 11 13 15 17 19 21 23 1 3 5 7 9 11 13 15 17 19 21 23 1 3 5 7 9 11 13 15 17 19 21 23
Aug10
Aug11
Aug12
Aug13

Fig. 15

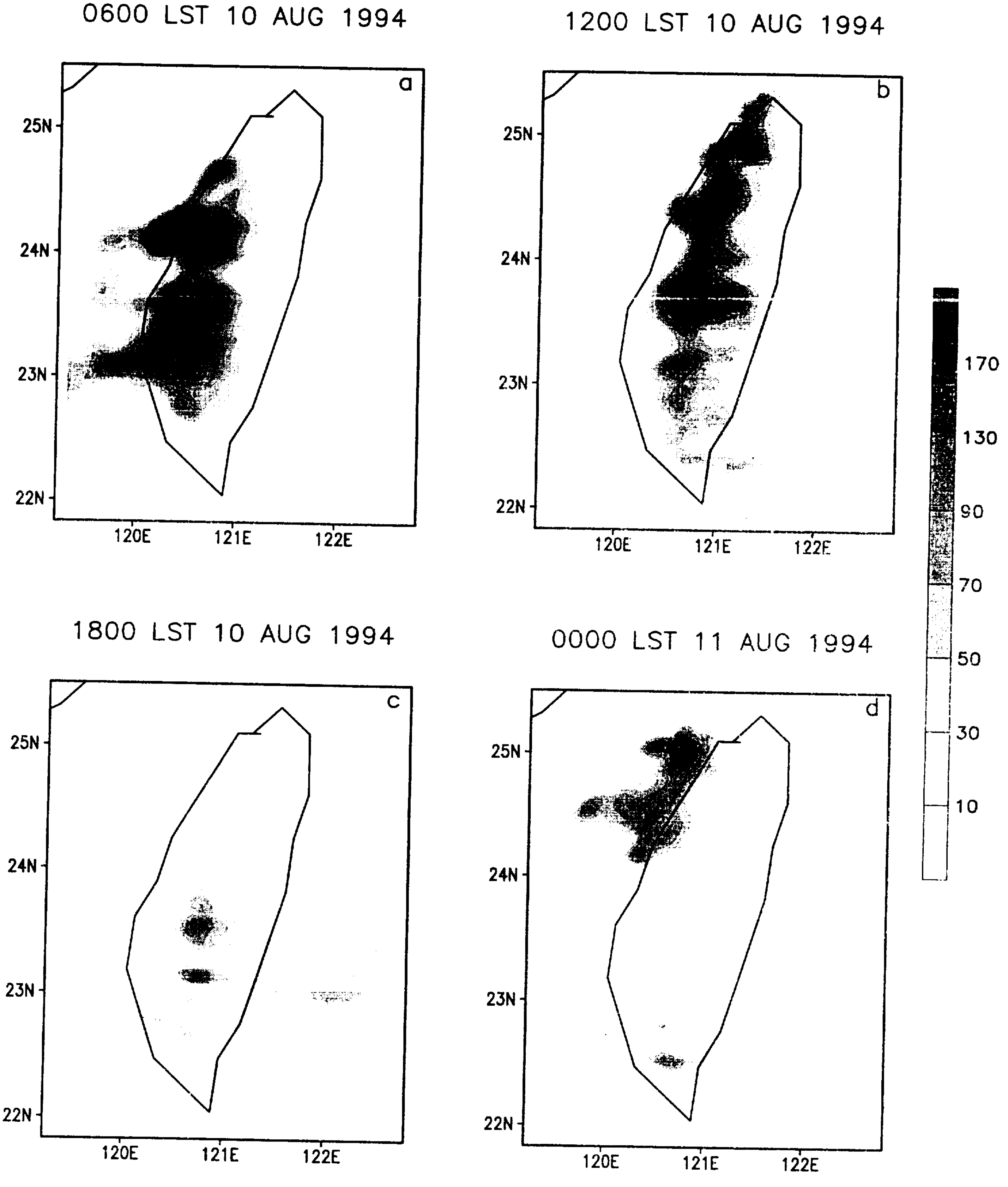
0600 LST 10 AUG 1994

1200 LST 10 AUG 1994

1800 LST 10 AUG 1994

0000 LST 11 AUG 1994

Fig. 16

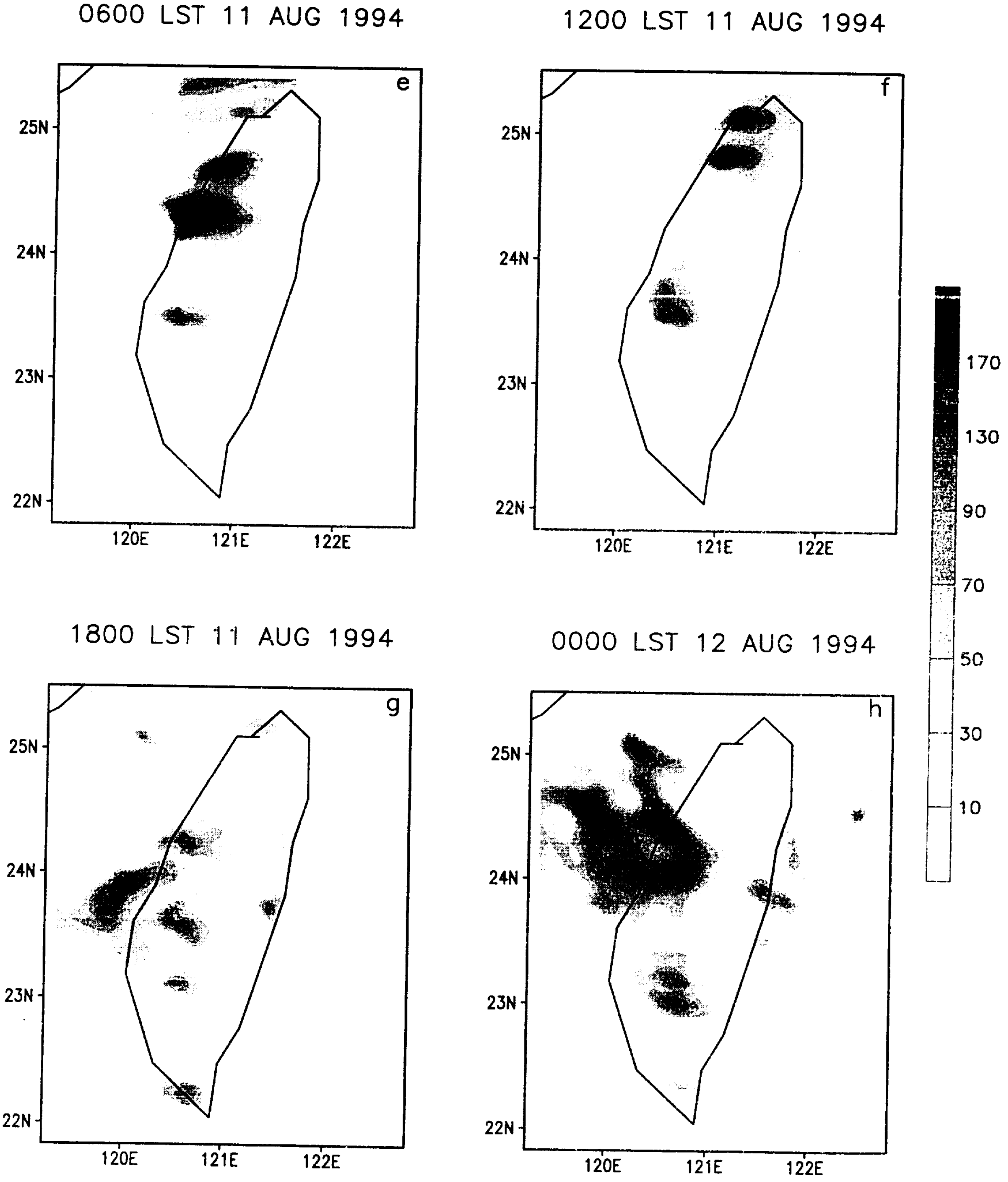
0600 LST 11 AUG 1994
e
1200 LST 11 AUG 1994
f
1800 LST 11 AUG 1994
g
0000 LST 12 AUG 1994
h
25N
24N
23N
22N
120E
121E
122E
170
130
90
70
50
30
10

Fig. 16 (Cont.)

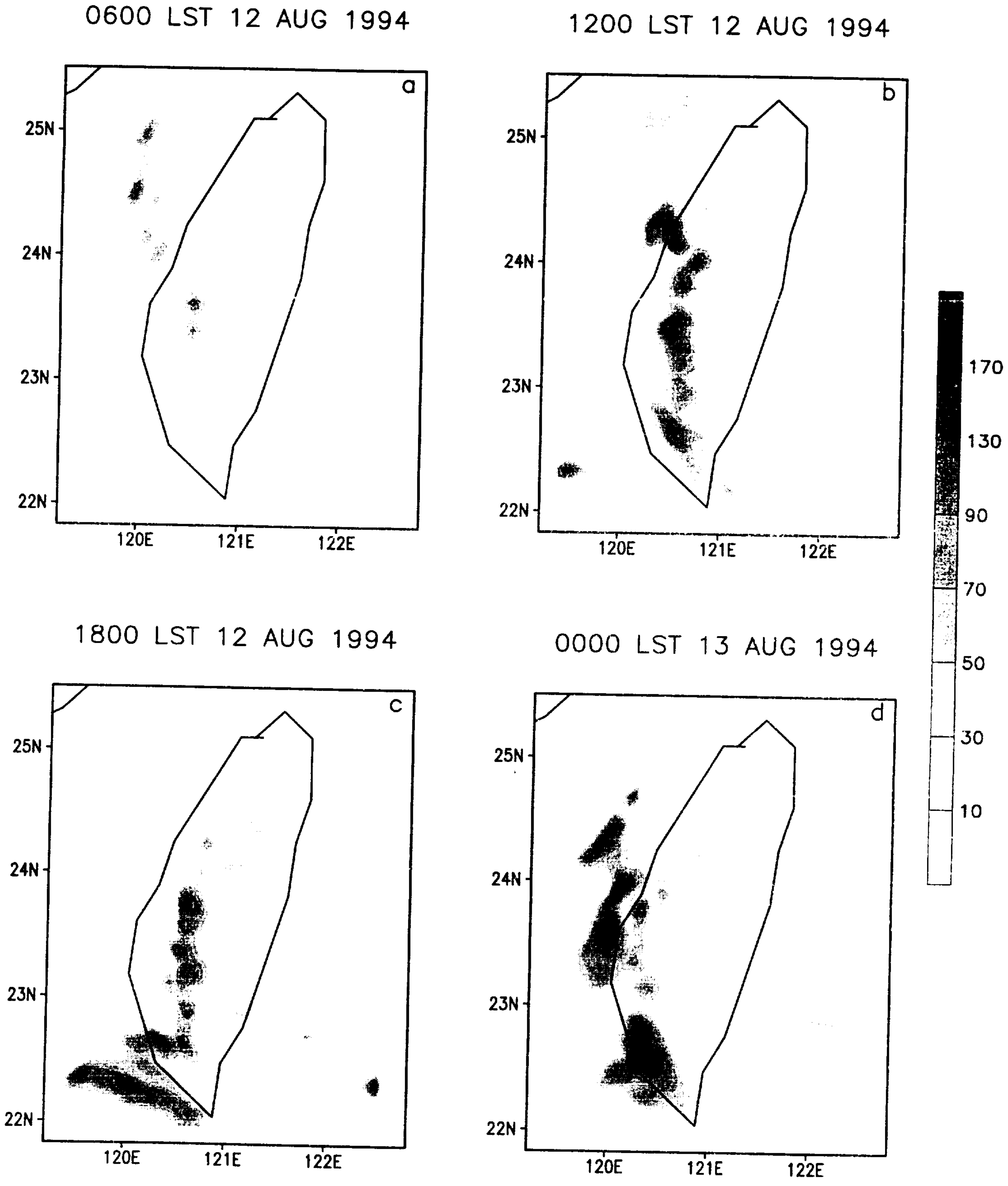
0600 LST 12 AUG 1994
a
1200 LST 12 AUG 1994
b
1800 LST 12 AUG 1994
c
0000 LST 13 AUG 1994
d
25N
24N
23N
22N
120E
121E
122E
170
130
90
70
50
30
10

Fig. 17

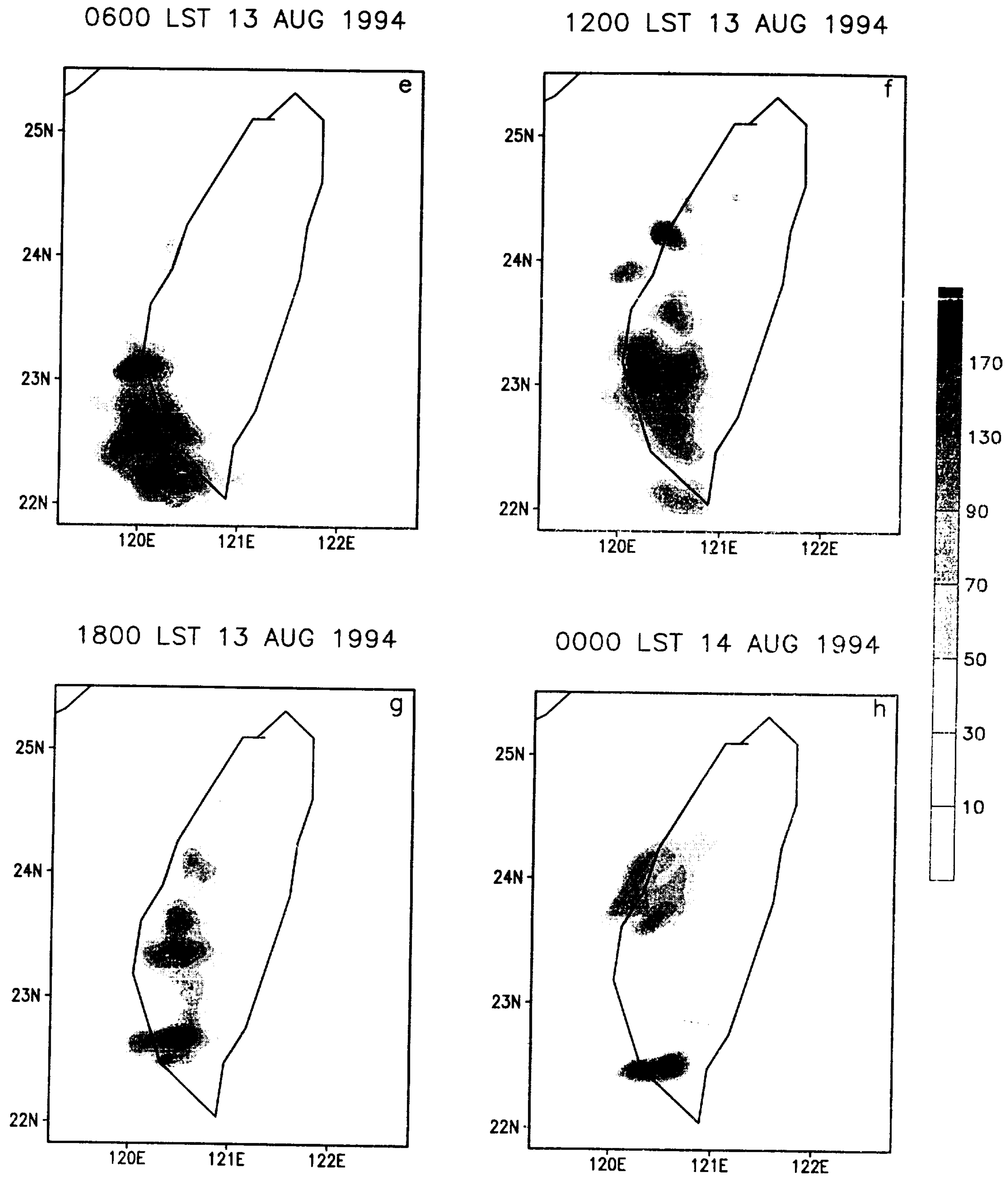
0600 LST 13 AUG 1994

1200 LST 13 AUG 1994

1800 LST 13 AUG 1994

0000 LST 14 AUG 1994

Fig. 17(Cont.)

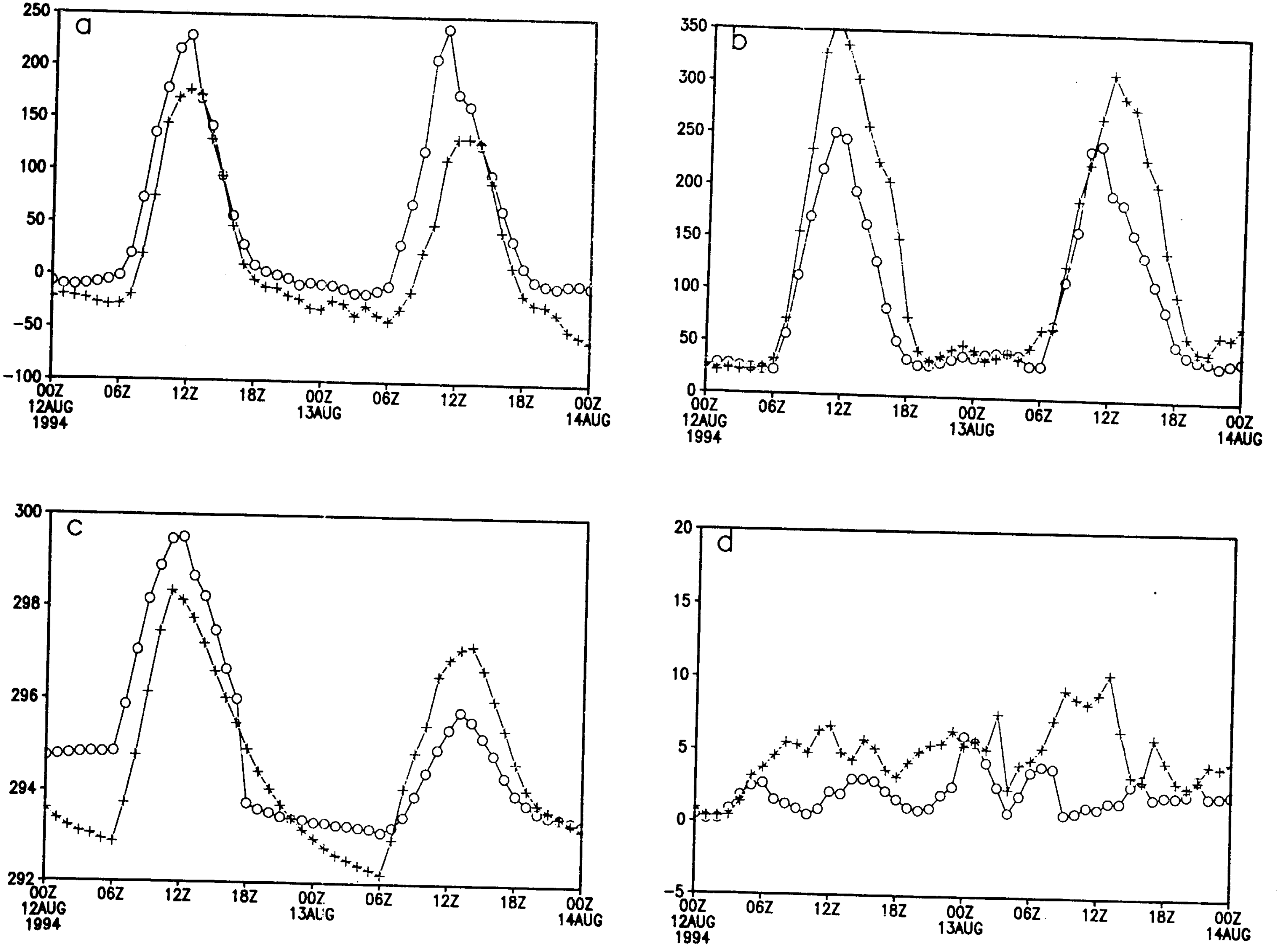
a
250
200
150
100
50
0
−50
−100
00Z 12AUG 1994
06Z
12Z
18Z
00Z 13AUG
06Z
12Z
18Z
00Z 14AUG
b
350
300
250
200
150
100
50
0
00Z 12AUG 1994
06Z
12Z
18Z
00Z 13AUG
06Z
12Z
18Z
00Z 14AUG
c
300
298
296
294
292
00Z 12AUG 1994
06Z
12Z
18Z
00Z 13AUG
06Z
12Z
18Z
00Z 14AUG
d
20
15
10
5
0
−5
00Z 12AUG 1994
06Z
12Z
18Z
00Z 13AUG
06Z
12Z
18Z
00Z 14AUG

Fig 18

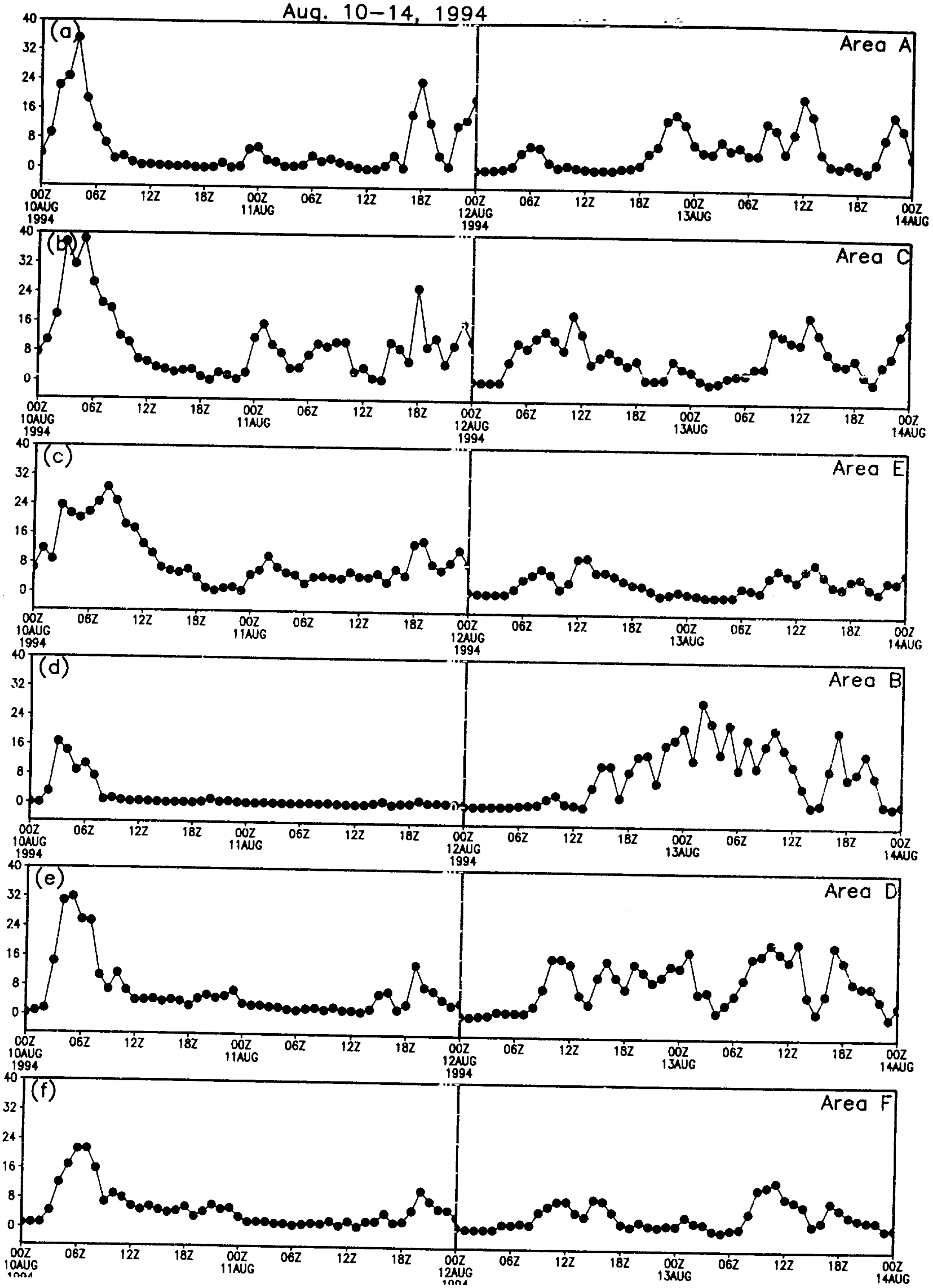
Aug. 10-14, 1994
(a)
Area A
(b)
Area C
(c)
Area E
(d)
Area B
(e)
Area D
(f)
Area F
40
32
24
16
8
0
00Z 10AUG 1994
06Z
12Z
18Z
00Z 11AUG
06Z
12Z
18Z
00Z 12AUG 1994
06Z
12Z
18Z
00Z 13AUG
06Z
12Z
18Z
00Z 14AUG

Fig. 19

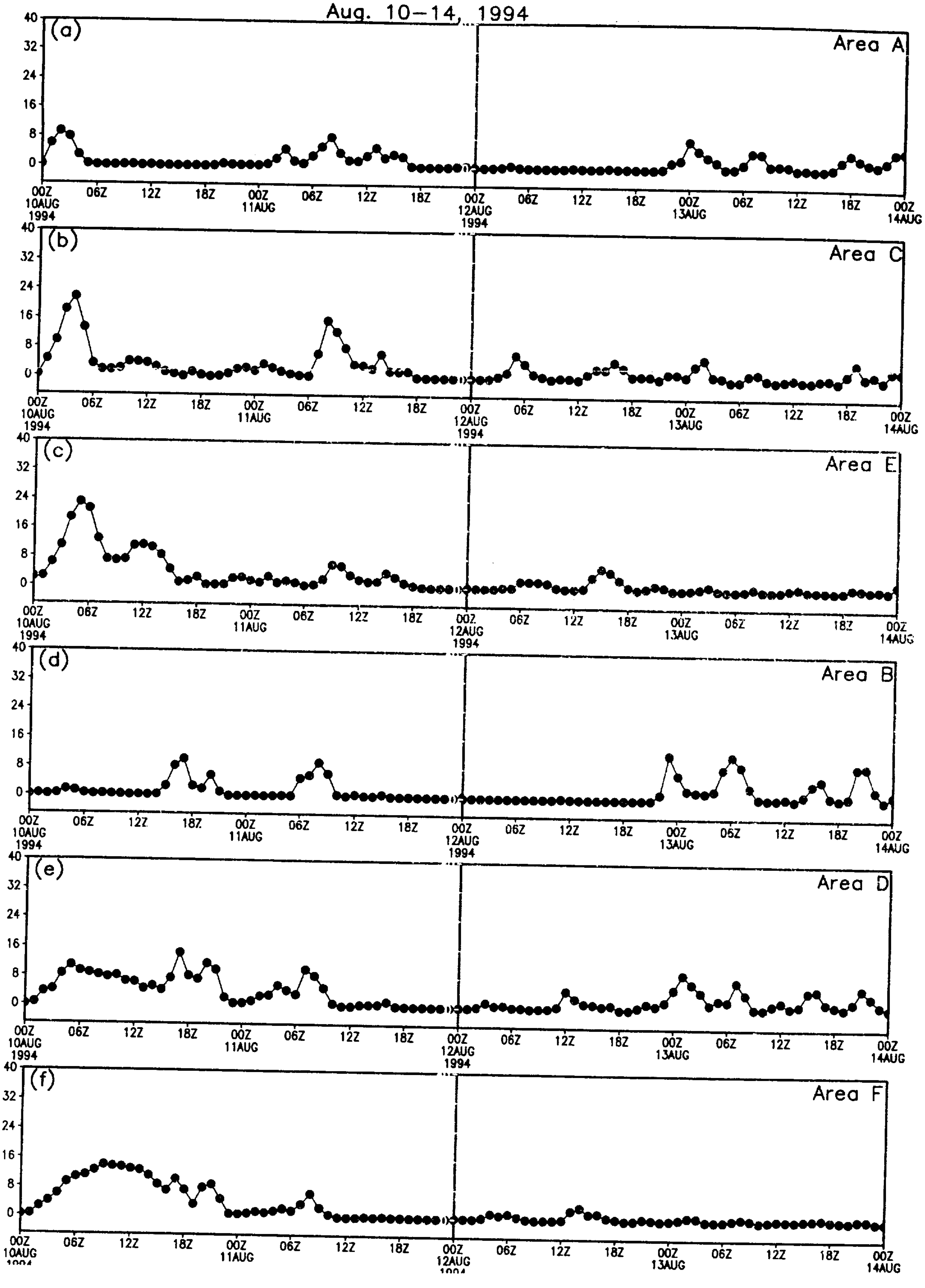
Aug. 10–14, 1994
(a)
Area A
(b)
Area C
(c)
Area E
(d)
Area B
(e)
Area D
(f)
Area F
40
32
24
16
8
0
00Z 10AUG 1994
06Z
12Z
18Z
00Z 11AUG
06Z
12Z
18Z
00Z 12AUG 1994
06Z
12Z
18Z
00Z 13AUG
06Z
12Z
18Z
00Z 14AUG

Fig. 20

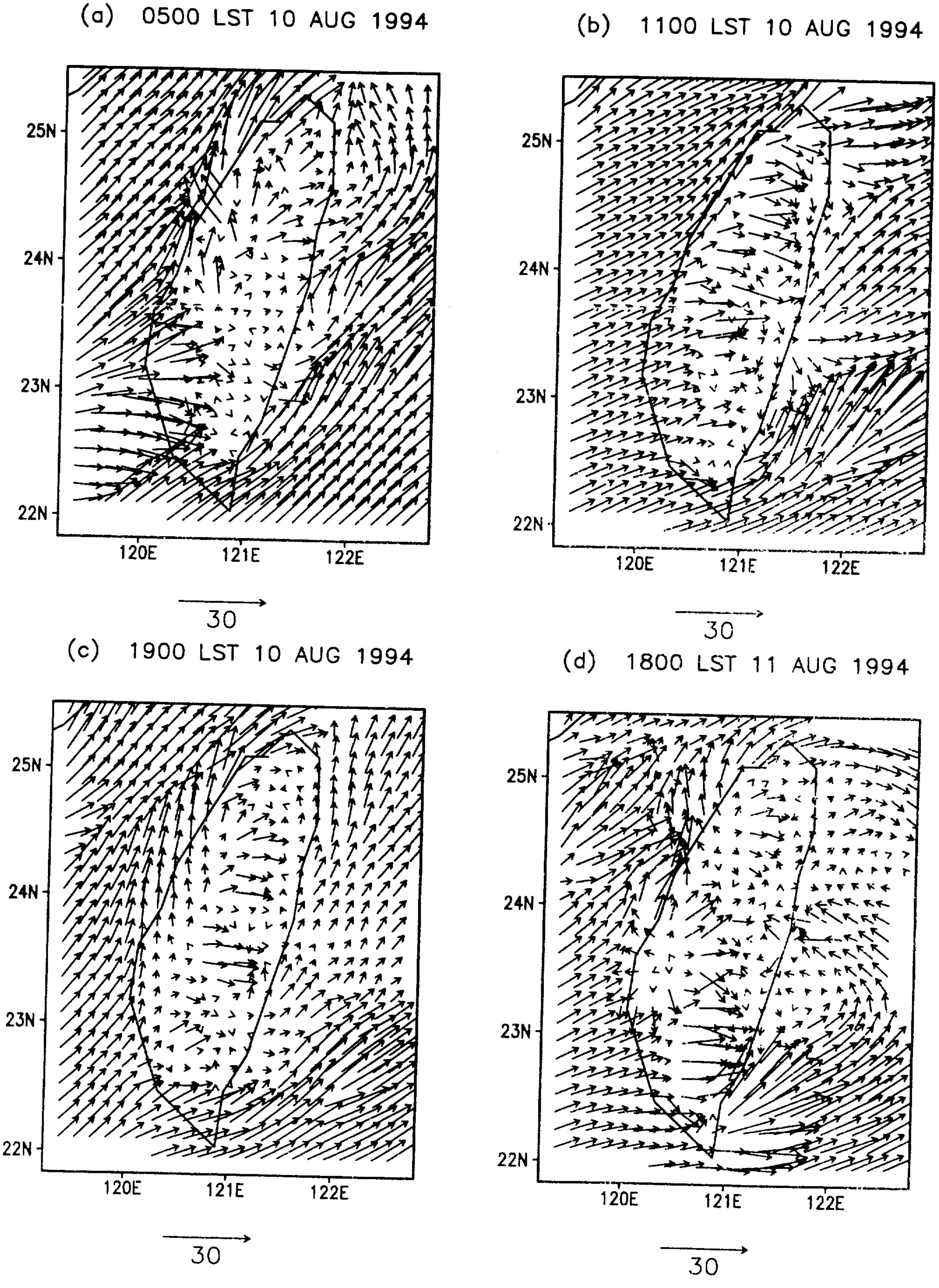
(a) 0500 LST 10 AUG 1994
(b) 1100 LST 10 AUG 1994
(c) 1900 LST 10 AUG 1994
(d) 1800 LST 11 AUG 1994
25N
24N
23N
22N
120E
121E
122E
30

Fig. 21

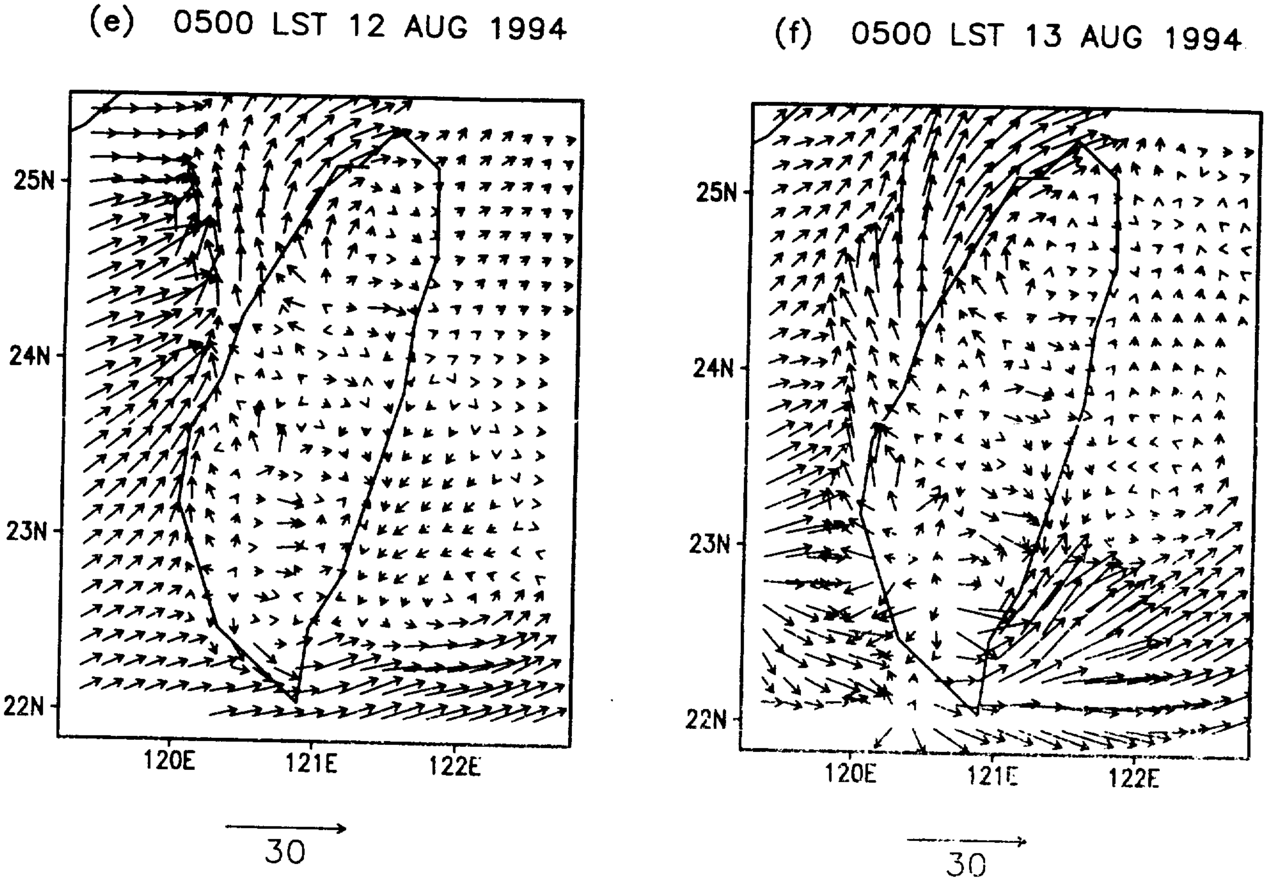
(e) 0500 LST 12 AUG 1994
25N
24N
23N
22N
120E
121E
122E
30
(f) 0500 LST 13 AUG 1994
25N
24N
23N
22N
120E
121E
122E
30

Fig. 21 (Cont.)

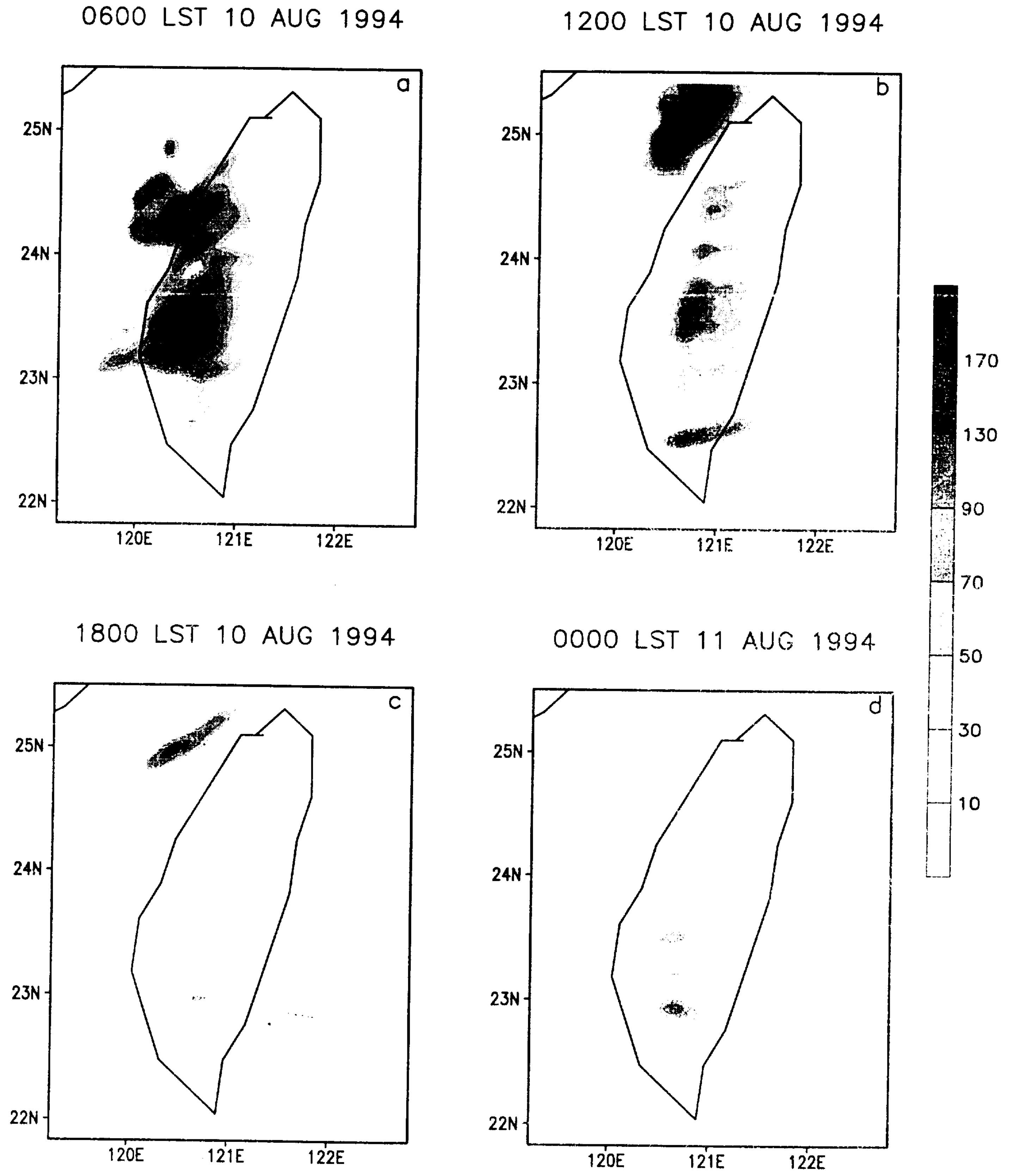
0600 LST 10 AUG 1994
a
1200 LST 10 AUG 1994
b
1800 LST 10 AUG 1994
c
0000 LST 11 AUG 1994
d
25N
24N
23N
22N
120E
121E
122E
170
130
90
70
50
30
10

Fig. 22